The Pennsylvania State University
The Graduate School

SURFACE MICROMACHINED PERISTALTIC PUMPS USING LEAD ZIRCONATE TITANATE FILM

A Thesis in
Materials Science and Engineering
by
Eunki Hong

Submitted in Partial Fulfillment
of the Requirements
for the Degree of

Doctor of Philosophy

May 2004

The thesis of Eunki Hong has been reviewed and approved* by the following:

Susan Trolier-McKinstry
Professor of Ceramic Science and Engineering
Thesis Advisor, Chair of Committee

Clive A. Randall
Professor of Materials Science and Engineering

Srinivas Tadigadapa
Associate Professor of Electrical Engineering

S.V. Krishnaswamy
Adjunct Professor of Materials Science and Engineering

James P. Runt
Professor of Polymer Science and Engineering
Associate Head for Graduate Studies,
Department of Materials Science and Engineering

*Signatures are on file in the Graduate School.

Abstract

In recent years, miniaturization of mass spectrometer systems has been studied for portable chemical and biological sensors. In this study, the design, fabrication and characterization of MEMS pumps which could be integrated into a MEMS mass spectrometer was investigated.

The MEMS pumps were designed as peristaltic pumps with three interconnected chambers. Sequential motion of the piezoelectric diaphragms on these chambers effect pumping. Diaphragm actuators driven with ring–shaped interdigitated transducer (IDT) electrodes were required to generate deflections of several micrometers. This design used SiO_2 and PZT as the passive and active layers, respectively. Zirconia films were used as barrier layers to prevent the rapid diffusion of Pb in PZT into the SiO_2 at crystallization temperatures. The residual stresses of SiO_2, PZT, and ZrO_2 were evaluated to be -147, 100-150 and 230-270 MPa after the final film deposition. Diaphragm actuators were fabricated by bulk micromachining. The PZT in the actuators showed good dielectric and ferroelectric properties. The dielectric constants were around 660 with dielectric losses of below 2 % at 10 kHz. The remanent polarizations and coercive fields were 20 $\mu C/cm^2$ and 50 kV/cm. The diaphragm actuators behaved more like membranes than plates and had a residual stress of 86 MPa. Non-180° domain motion of the PZT layer in diaphragm actuators was limited due to the residual stress and clamping by the elastic passive silicon oxide. For 980 μm diameter diaphragm actuators with an IDT spacing of 10 μm, center deflections of around 4.3 μm, larger than the thickness of the structure, were obtained at a voltage of 120 V. The deflection profiles had a funnel shape due to the relative contributions of d_{31} and d_{33} piezoelectric

coefficients. In addition, the deflection profiles from IDT-mode diaphragm actuators were modified using annular IDT electrodes with inactive center areas. For a given voltage applied to the electrodes, the deflection decreases with increasing percentage of inactive area. However, the deflection profile is much flatter for diaphragms with a higher percentage of inactive area, resulting in a larger stroke volume for the MEMS pumps.

The MEMS pumps were fabricated by surface micromachining. The fabrication steps included formation of chamber and channel structures by reactive ion etching (RIE) and subsequent release of diaphragm structures using a XeF_2 process. Ion-milling was used to form portholes for the pump structure. The diaphragm actuators in the structures generated enough deflection to touch the bottom of chambers 3–4 μm deep. Sequential motion of the diaphragm actuators in a three stage peristaltic pump was demonstrated.

Table of Contents

List of Figures

List of Tables

Acknowledgments

I wish to express my sincere gratitude to Dr. Susan Trolier-McKinstry for her guidance, advice and support while I was pursuing my doctorate degree at the Penn State University. I would also like to thank the other members of my committee, Dr. Clive Randall, Dr. Srinivas Tadigadapa and Dr. S.V. Krishnaswamy. I am grateful to Dr. Carl Freidhoff and Dr. Tim Braggins of Northrop Grumman corporation for their help and advice in this work. I would specially like to thank Robert Smith for his help in fabrication and characterization of the MEMS structures. I am also grateful to Dr. Mark Horn, Dr. Lawrence Pilione (for their help in stress measurements), Andrzej Mieckowski, Guy Lavallee (Nanofab, MRI), William Drawl (MRL) and the other technical staff. Financial support for this research from Northrop Grumman Corporation and DARPA is greatly appreciated. I also want to acknowlege the financial support for my PhD studies provided by Rotary International Foundation. This work was performed in part at the Penn State Nanofabrication Facility, a member of the NSF's National Nanofabrication Users Network.

I want to thank my colleagues (Azo, Mike, Tanawadee, Nazanin, Mustafa, Qifa, Steve and others) and friends in MRL and elsewhere. I would specially like to thank Raviprakash for his patient proofreading and help in LaTeX.

Lastly but most importantly, I would like to express my gratitude to my parents, my brother and his family for their love and support.

Chapter 1

Introduction and Statement of Goals

1.1 Introduction

Microelectromechanical systems (MEMS) are miniature sensors and actuators fabricated using techniques developed for microelectronics. This processing makes it possible to scale down the size and cost significantly. The cost reduction has been a strong driving force for miniaturization of numerous macroscopic devices using micromachining techniques. Since the late 1960's, various MEMS devices have been fabricated and demonstrated in academic and industrial laboratories. One good example of a commercially successful MEMS device is the MEMS accelerometer manufactured by Analog Devices, Inc. [1, 2]. The processing of the accelerometer combines surface micromachined differential capacitive sensors and electronic signal processing circuits on a single chip. This provides several benefits when compared to bulk piezoelectric and capacitive sensors: lower cost, stable sensitivity, high reliability and ease of use. These accelerometers have been adapted as

impact sensors to deploy air-bags in many automobiles. In light of the commercial success of the MEMS accelerometer, several research groups have investigated miniaturization of conventional laboratory instruments that are large, heavy, and expensive [3–5]. The miniature instruments will be cheap and small. Consequently, instead of the sample being brought to a laboratory, these portable instruments can be used for local real-time detection. One of many examples of this is a MEMS mass spectrometer system [6–8].

Mass spectrometers are instruments used to measure the mass and relative concentration of atoms and molecules in a gas mixture. These devices can be used to identify chemical and biological (C–B) molecules [9]. Such sensors are necessary in applications ranging from quality control of food and drug products to medical diagnosis, environmental monitoring, space missions, and defense industries [10]. In some interplanetary missions they are used to identify and estimate the abundance of atoms and molecules on extraterrestrial surfaces and atmospheres [11]. On battle fields, it is essential to detect life–threatening C–B agents. The recent anthrax scare in the United States (2001) highlighted the necessity of these kinds of devices. In addition to mass spectrometers, there are many other types of C–B sensors [10]: conductivity sensors, piezoelectric sensors, MOSFET sensors, and optical sensors. These sensors utilize changes in electrical or optical properties in response to C–B agents. Thus, a separate sensor is required to identify different C–B molecules. In contrast, mass spectrometers recognize species according to their mass–to–charge ratio; thus a mass spectrometer can identify diverse atoms and molecules simultaneously. Despite these advantages, conventional mass spectrometers have many limitations for use as portable detection systems. They are large, heavy, and expensive. In addition, conventional mass spectrometers require sophisticated pumping systems to create ultra high vacuum [9].

To overcome these problems with conventional mass spectrometers, several groups have successfully miniaturized different components of a mass spectrometer system including the sampling orifice [5], ionizer [12,13], ion optics [5], mass filter [8,14,15], etc. However, fabricating a micromachined vacuum pump to evacuate the mass

filter and ionizer regions of MEMS mass spectrometers is still a daunting challenge [16]. To date, many micropumps fabricated were designed to transport liquid for medical applications rather than pumping gas [17]. In addition, most of them were fabricated by bulk micromachining and required additional assemblies [18,19]. Micromachined pumps for MEMS mass spectrometer systems should fulfill several requirements, including:

- the ability to pump compressible gas
- ease of incorporation into MEMS mass spectrometers
- ease of fabrication

In this study, surface micromachined peristaltic pumps using lead zirconate titanate (PZT) films are designed and fabricated to satisfy the aforementioned requirements. Peristaltic pumps consist of at least three interconnected chambers [20]. A sequential motion of actuators on the chambers effects pumping. The pumps are operated by squeeze or suction of the fluid in the chambers, which enables flow of compressible gas. Surface micromachining makes it possible to fabricate compact pump structures without having to assemble different components [16]. The compact structures enables them to be easily incorporated into MEMS mass spectrometers. To date, there are few reports on surface micromachined pumps using PZT films despite a large number of reports on micropumps that use bulk PZT disks and were fabricated by bulk micromachining and manually assembled [18, 20]. Difficulties in fabricating surface micromachined pumps using PZT films lie in the lack of both proper processing techniques and appropriate design of piezoelectric diaphragm actuators. PZT films are deposited at high temperatures of around 650 °C and easily react with silicon or silicon oxide [21]. This requires modification of conventional surface micromachining techniques using common materials in microelectronics such as silicon, silicon oxide, and silicon nitride. Diaphragm actuators using PZT films must generate deflections larger than the structure thicknesses. For this reason, it requires different approaches to designing actuators from those using bulk PZT disks (which have deflections that

are much smaller than the actuator thicknesses). This thesis investigates surface micromachining techniques to fabricate MEMS peristaltic pumps using silicon as a sacrificial material and a XeF_2 release process. In addition, PZT diaphragm actuators, which are less than 1 mm in diameter and generate large deflections up to several micrometers using ring–shaped interdigitated transducer (IDT) electrodes, are designed, fabricated and characterized.

1.2 Statement of Goals

The objectives of this work are as follows.

Design–Aspects of MEMS pump and diaphragm actuators (Chapter 3) The proposed MEMS pump structures for use in MEMS mass spectrometers are discussed. To design diaphragm actuators for the MEMS pumps, problems in conventional piezoelectric actuators using a piezoelectric layer between top and bottom electrodes are analyzed in terms of fundamental mechanics and characteristics of PZT films. This knowledge is used to develop a new design for diaphragm actuators using IDT electrodes to generate large deflections. This design is verified using finite element analysis.

Processing and characterization of zirconia and PZT films (Chapter 4) As a step towards fabricating the MEMS pumps and diaphragm actuators discussed in Chapter 3, a sol-gel deposition technique to form PZT films on silicon wafers with silicon oxide surfaces was developed. Because of difficulties in depositing crack–free PZT films on SiO_2 by a sol-gel method, zirconia was investigated as a buffer layer. In addition, the development of residual stresses in the films deposited on silicon wafers was evaluated to extract the mechanical information required for designing diaphragm actuators and MEMS pumps.

Micromachined diaphragm actuators (Chapter 5) Using the deposition techniques developed in Chapter 4, piezoelectric diaphragms actuated by IDT electrodes were fabricated by bulk micromachining. The diaphragm actuators were characterized to understand their electrical and mechanical properties, which are critical for the design of MEMS pumps. The deflections were evaluated as a function of applied voltage. Considering the bending mechanics and using modified IDT configurations, deflection shapes were improved to increase stroke–volumes.

Understanding the piezoelectric responses of PZT films on released diaphragms is both scientifically and technically interesting. When a piezoelectric diaphragm is excited, the resonance frequencies are dependent on the initial stress and the stress induced by the piezoelectric response. Therefore, changes in the resonance frequencies can be utilized to study the piezoelectric properties of the PZT films in diaphragm actuators. Especially, the clamping of PZT layer by a substrate is known to degrade the piezoelectric responses, partially due to reduction in the non–180 ° domain wall mobility. Since non–180° domain wall motions induce additional stresses in diaphragm structures, a stress–sensitive resonance method can be used to evaluate non–180° domain wall motions. In addition, ambient pressure and temperature effects on diaphragm actuators can be evaluated indirectly by the resonance method. Thus, by understanding the theoretical resonance of edge–clamped circular diaphragms, resonance measurements for piezoelectric diaphragm actuators are developed.

MEMS piezoelectric peristaltic pumps (Chapter 6) From ideas learned from Chapter 3, 4, and 5, MEMS pumps were fabricated by surface micromachining. The surface micromachining technique utilized silicon as a sacrificial material and a XeF_2 release process. Process steps were developed and optimized for fabricating MEMS pumps. Finally, the fabricated MEMS pumps were evaluated.

References

[1] H. Samuels, "Single – and Dual – Axis Micromachined Accelerometers," *Analog Dialogue*, vol. 30, no. 4, 1995.

[2] J. Doscher, "ADXL105: A Lower Noise, Wider Bandwidth Acceleromter Rivals Performance of More Expensive Sensors," *Analog Dialogue*, vol. 33, no. 6, 1999.

[3] R.C. Anderson, G.J. Bogdan, Z. Barniv, T.D. Dawes, J. Winkler, and K. Roy, "Microfluidic Biochemical Analysis System," *in Proceedings of 1997 International Conference on Solid–State Sensors and Actuators, Chicago, IL*, pp. 477–480, 1999.

[4] D.A. Crewe, M.M. Ruffin, and A.D. Feinerman, "Initial Images with a Partially Micromachined Scanning Electron Microscope," *J. Vac. Sci. Technol. B*, vol. 14, no. 6, pp. 3808–3812, 1996.

[5] C.B. Freidhoff, R.M. Young, and S. Sriram, *U.S. Patent No. 5,386,115 (Jan. 31, 1995).*

[6] C.B. Freidhoff, R.M. Young, S. Sriram, T.T. Braggins, T.W. O'Keefe, J.D. Adam, H.C. Nathanson, R.R.A. Syms, T.J. Tate, M.M. Ahmad, S. Taylor, and J. Tunstall, "Chemical Sensing using Nonoptical Microelectromechanical Systems," *J. Vac. Sci. Technol. A*, vol. 17, no. 4, pp. 2300–2307, 1999.

[7] D.H. Holkeboer, T.L. Karandy, F.C. Currier, L.C. Frees, and R.E. Ellefson, "Miniature Quadruple Residual Gas Analyzer for Process Monitoring at milliTorr Pressures," *J. Vac. Sci. Technol. A*, vol. 16, no. 3, pp. 1157–1162, 1998.

[8] R.R.A. Syms, T.J. Tate, M.M. Ahmad, and S. Taylor, "Design of a Microengineered Electrostatic Quadrupole Lens," *IEEE Trans. on Electron. Devices*, vol. 45, no. 11, pp. 2304–2311, 1998.

[9] E.D. Hoffmann, J. Charette, and V. Stroobant, *Mass Spectrometry: Principles and Applications.* John Wiley and Sons, 1996.

[10] H.T. Nagle, R. Gutierrez-Osuna, and S.S. Shiffman, "The How and Why of Electronic Noses," *IEEE Spectr.*, vol. 35, pp. 22 – 31, 1998.

[11] W.B. Brinckerhoff, G.G. Managadze, R.W. McEntire, A.F.Cheng, and W.J.Green, "Laser Time–Of–Flight Mass Spectrometry for Space," *Rev. Sci. Instrum.*, vol. 71, no. 2, pp. 536–545, 2000.

[12] R.M. Young, C.B. Freidhoff, T.T. Braggins, and T.V. Congedo, *U.S. Patent No. 5,747,815 (May 5, 1998).*

[13] D.C. Perng, D.A. Crewe, and A.D. Feinerman, "Micromachined Thermionic Emitters," *J. Micromech. Microeng.*, vol. 2, pp. 25–30, 1992.

[14] C.B. Freidhoff and R.M. Young, *U.S. Patent No. 5,536,939 (Jul. 16, 1996).*

[15] N. Sillon and R. Baptist, "Micromachined Mass Spectrometer," *Sens. Actuators B*, vol. 83, pp. 129–137, 2002.

[16] G. Kovacs, *Micromachined Transducers – Sourcebook*. WCB McGraw Hill, New York, 1998.

[17] N. Nguyen, X. Huang, and T.K. Chuan, "MEMS–Micropumps: A Review," *Journal of Fluids Engineering*, vol. 124, pp. 384 – 392, 2002.

[18] J.G. Smits, "Piezoelectric Micropump with Three Valves Working Peristaltically," *Sens. Actuators*, vol. 15, pp. 153–167, 1988.

[19] A. Olsson, "Valve-less Diffuser Micropumps," PhD thesis, Royal Institute of Technology, 1998.

[20] N. Nguyen and X. Huang, "Miniature Valveless Pumps Based on Printed Circuit Board Technique," *Sens. Actuators A*, vol. 88, pp. 104–111, 2001.

[21] Q.F. Zhou, E. Hong, R. Wolf, and S. Trolier-McKinstry, "Dielectric and Piezoelectric Properties of PZT 52/48 Thick Films with (100) and Random Crystallographic Orientation," *in Proceedings of Materials Research Society Symposium, Boston, USA*, no. 655, 2001.

Chapter 2

Literature Review

In this chapter, MEMS mass spectrometers are reviewed. Since the main goal of the MEMS pumps in this study is to provide an appropriate micromachined pumping system for MEMS mass spectrometers, knowledge of MEMS mass spectrometers is essential for designing them. In addition, earlier work on micropumps and piezoelectric materials for microelectromechanical systems is also discussed.

2.1 MEMS Mass Spectrometers

A mass spectrometer is an instrument for analyzing atoms or molecules in a sample gas by measuring the mass–to–charge ratio [1]. The sample gas is ionized, typically by an electron beam, accelerated and injected into the mass filter, which separates the ions according to their mass–to–charge ratio in a static or an oscillating electromagnetic field and subsequently detects them. The mass spectrum that results can be used to identify atoms or molecules in the sample gas by referring to a mass spectral library. In addition, liquids or solids can be analyzed using a suit-

able vaporization method. Hence, a mass spectrometer can be used as a chemical sensor. This kind of sensor is utilized in many fields such as medical diagnosis, environmental surveys, safety and security and defense applications [2]. Especially, in current battlefields, there is danger of chemical and/ or biological weapons, which makes portable chemical and biological sensors essential. However, a conventional bench–top mass spectrometer system costs roughly 17,000 U.S. dollars, the weight is 70 kg, the volume is 30000 cm^3, and the power consumption is 1200 W [3]. Thus, there are difficulties in employing conventional mass spectrometers as in–field, real-time detectors.

To overcome the limitations with conventional mass spectrometers for portable detectors, miniaturization has been investigated in two ways. Several research groups have used new designs and accurate machining, including some micromachined components, and fabricated mass spectrometers that can fit in a shoe case [4,5]. There was a big reduction in size, cost, weight, and power consumption compared to conventional bench–top mass spectrometers. However, these devices are still too bulky and heavy to be used as portable devices. For this reason, fully micromachined mass spectrometer systems have been studied by many research groups [6–8].

Figure 2.1 illustrates the general concept of a MEMS spectrometer system consisting of a mass spectrometer, vacuum pump, and control electronics. As presented in Figure 2.1, the expected cost is 20 U.S. dollars, the weight is 200 g, the volume is 3 cm^3, and the power consumption is 0.5 W [3]. Such a MEMS mass spectrometer system can provide a reduction by a factor of 1000 in cost, weight, volume, and power consumption, which is useful in a hand-held detection device. In addition, the small size of MEMS mass spectrometer systems enables incorporation into many venues for environmental monitoring.

A proposed MEMS mass spectrometer system consists of seven parts (see Figure 2.2) [9]: 1) sampling orifice, 2) ionizer, 3) ion optics, 4) mass filter, 5) detector, 6) microprocessor, and 7) vacuum system. The operation of this MEMS mass

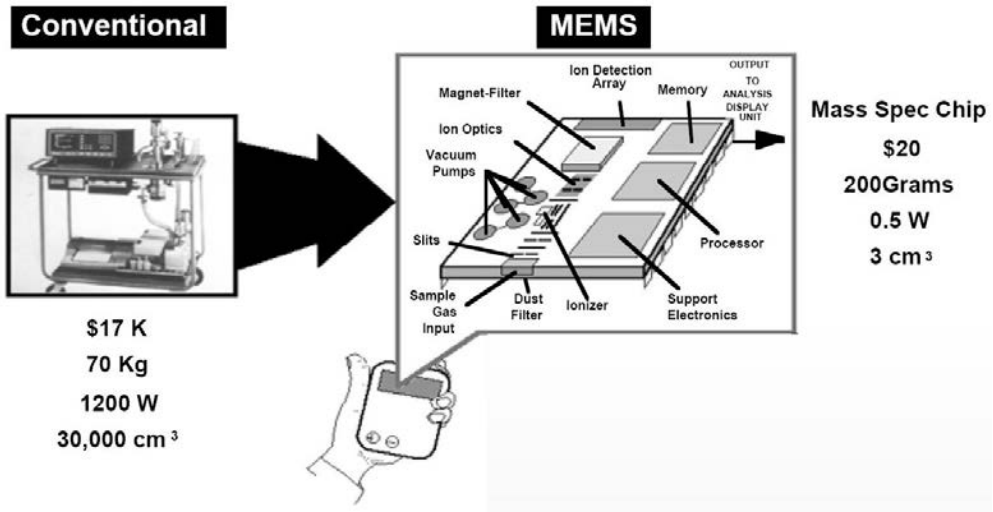

Figure 2.1. Mass spectrometer system on a chip, which has incorporated vacuum pumps, ionizer, ion detector, and control electronics onto a monolithic chip, from [3].

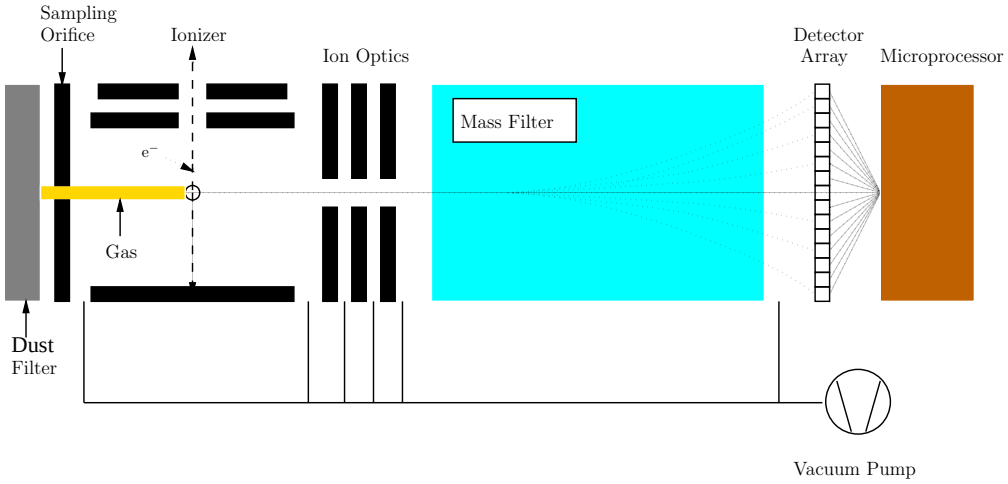

Figure 2.2. Seven components of a mass spectrometer system, from [10].

spectrometer system is as follows: a sample gas is introduced into the mass spectrometer system through the sampling orifice (possibly, a dust filter can be used to prevent dust particles from blocking the system.). The gas is then ionized by the ionizer. The ions are accelerated and focused by ion optics and passed through a mass filter. The mass filter separates the ions depending on the mass–to–charge ratio. The signal is detected by the detector array, which is connected to a mi-

croprocessor. Finally, the microprocessor analyzes the data by referring to a mass spectral library.

Conceptually, a MEMS mass spectrometer can be manufactured via bi-lithic integration [6]. Namely, the components of a mass spectrometer are fabricated on two separate silicon wafers and a complete device is formed by bonding the two wafers. However, hybrid methods, where the components are separately fabricated and later assembled, are commonly used. To date, mass filters [8, 10–12], ionizers [11, 13–15], and detectors [8] have been successfully fabricated by micromachining.

2.1.1 Mass Filters

The mass filter is an essential component for a mass spectrometer and is used to separate ionized atoms or molecules of different mass. Conventional mass spectrometers utilize various mass filters such as magnetic, time–of–flight, Fourier–transform cyclotron resonance, quadrupole, and double–focusing analyzers [16]. For MEMS mass spectrometers, Wien [8] and quadrupole mass filters [12] have been investigated. However, there is very little data available on the performance of micromachined mass filters. A review of those studies citing the advantages and limitations of micromachined mass filters is presented here.

Wien filter An ion moving with a velocity in a direction perpendicular to a magnetic field follows a circular trajectory due to the Lorentz force (Equation 2.1) and the ion's path can also be deflected by an applied electric field (Equation 2.2).

$$\vec{F}_{magnetic} = q\vec{v} \times \vec{B} \tag{2.1}$$

$$\vec{F}_{electric} = q\vec{E} \tag{2.2}$$

where $F_{electric}$ is the force exerted by the applied electric field (E), q is the charge of the ion, $F_{magnetic}$ is the force due to the magnetic field (B), and v is the velocity of the ion.

In a Wien filter, an electric field normal to the magnetic field is used to control the ion trajectory (see Figure 2.3). To get a straight trajectory, the electric force

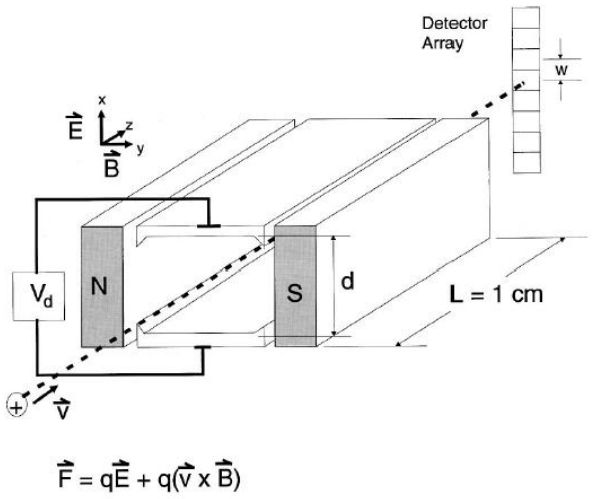

Figure 2.3. Principle of Wien filter, from [10].

should be balanced by the magnetic force. The mass of the ion, which can travel in a straight path, is given by Equation 2.3.

$$\frac{m}{q} = 2V_a \left(\frac{B}{E}\right)^2 \tag{2.3}$$

where m is the mass of the ion, V_a is the acceleration voltage (which determines the velocity of the ion). Thus, it is possible to determine $\frac{m}{q}$ from the deflection experienced for a given combination of E and B.

For Wien filters to work properly, it is important to form uniform electric and magnetic fields inside them. A permanent magnet is commonly used to obtain

a uniform magnetic field in micromachined Wien filters [8, 17]. Since the micromachined filters are usually only a few mm thick, it is easy to achieve a uniform magnetic field of a few thousand Gauss with a ceramic magnet [18].

Two different approaches have been reported for forming a uniform electric field in a Wien filter. Sillon et al. fabricated Wien filters using silicon on insulator (SOI) wafers with 200 μm thick silicon [8]. As seen in Figure 2.4, Si rods were formed by deep reactive ion etching (DRIE) and a metallic layer was deposited on them. The reduction of the aspect ratio of the width to the height of the channel made it possible to form a uniform electric field.

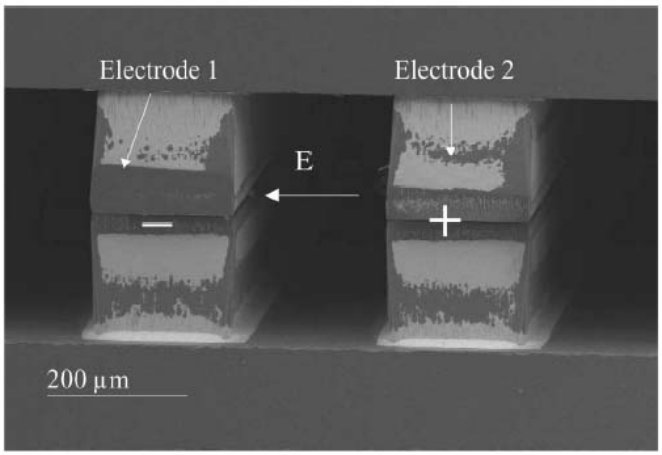

Figure 2.4. Micromachined Wien filter fabricated using a SOI wafer, from [8].

In contrast, Freidhoff et al. used two methods to get a uniform electric field, namely, additional segmented metal electrodes or resistive films [10]. In the first method, they formed additional pairs of opposed trimming electrodes on the Wien filter to modify the electric field in addition to the two main electrodes. These electrodes yielded a uniform electric field inside the filters. However, this approach was accompanied by difficulties in the fabrication because it demanded deposition of 10–15 μm wide lines with similar spacings over a length of 1 cm. Therefore, as an alternative, they used resistive films (undoped polysilicon) deposited on the top and bottom of a Wien filter to form a uniform electric field (see Figure 2.5). This approach simplified the fabrication.

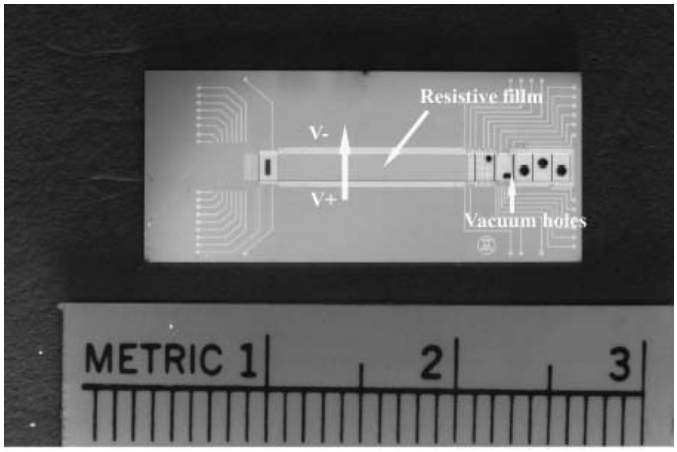

Figure 2.5. Micromachined Wien filter using a resistive film to form a uniform electric field, scale in cm, from [10].

The Wien filter fabricated by Sillon performed poorly. For higher masses such as 20 and 73 amu, the resolution was too low to separate different masses [8]. This is attributed to the fact that the channel was too wide (200 μm) and there was only one detector for each channel. Therefore, several neighouring ions, especially for higher masses (heavy ions deflect to a lesser extent in response to magnetic and electric fields than lighter ones) arrive at the detector without any separation.

In contrast, in the Wien filter in Figure 2.5, using a detector array, a resolution of 1 amu at 150 amu (see Figure 2.6) was obtained, which is comparable to a higher–priced bench–top mass spectrometer [18].

The performance of a mass spectrometer is expressed by the resolving power (R) [16]:

$$R = m/\Delta m \tag{2.4}$$

This ratio describes the ability of a mass spectrometer to distinguish ions having masses of m from those of $m + \Delta m$.

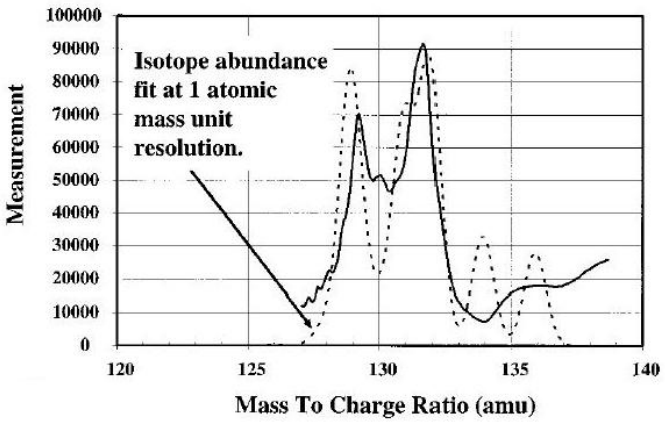

Figure 2.6. Mass spectrum (solid line) of xenon together with a simulated spectrum (dashed line) of the natural isotope pattern with a resolution of 1 amu at 150 amu, from [10].

For a Wien filter, the resolving power is given by Equation 2.5 [10].

$$\frac{m}{\Delta m} = \frac{V_d L^2}{2 d V_a \Delta w} \tag{2.5}$$

where V_d is the deflection potential, L is the length of the filter, d is the distance between the electric field plates, V_a is the acceleration voltage, and Δw is the spacing on the detector array (see Figure 2.3).

In terms of miniaturization, reduction of the length of the filter decreases the resolving power, but the distance between the electric field plates and the spacing on the detector array can be easily reduced, resulting in a significant enhancement in the resolving power. Therefore, Wien filters can be miniaturized by micromachining without a big loss in the resolving power.

Quadrupole filter The quadrupole mass filter, invented by Wolfgang Paul and Steinwedel in the early 1950's, is the most popular mass filter employed in macroscopic mass spectrometers. The filter (see Figure 2.7) consists of four cylindrical electrodes, which are equidistant from each other [19]. The application of voltages

to diagonally opposite electrode pairs results in a hyperbolic potential field near the axis. The driving voltage contains both dc and rf components, whose amplitudes are scanned while being held in a fixed ratio. For a given applied voltage, the

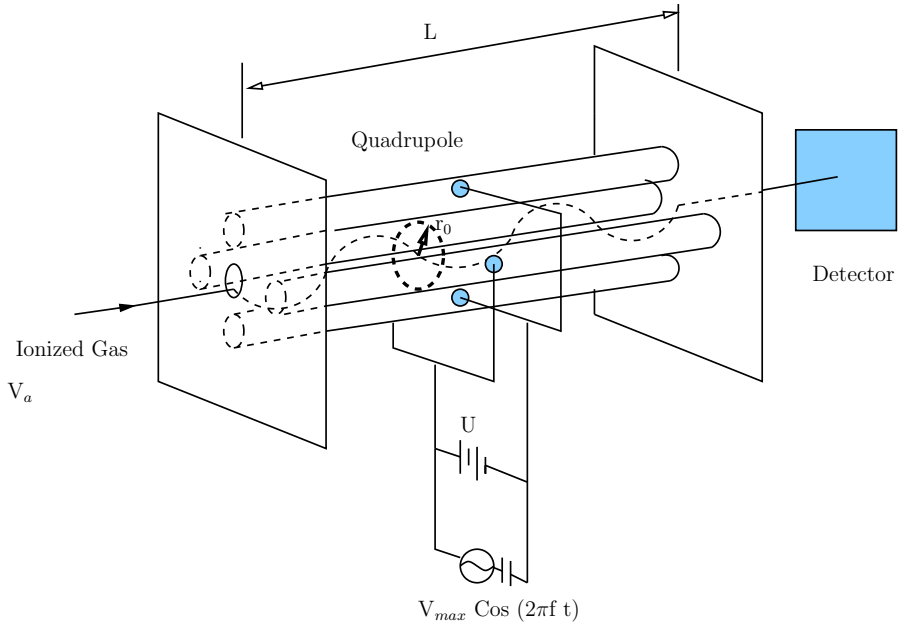

Figure 2.7. Principle of quadrupole filter, from [19].

filter transmits ions of a specific mass–to–charge ratio and deflects away other ions by inducing a potential field distribution that is periodic in time and symmetric with respect to the axis of the ion beam [12].

Syms et al. fabricated a micromachined quadrupole filter, consisting of 500 μm diameter metallized silica rods (see Figure 2.8) [7]. First, silica rods were coated with gold and then mounted on two silicon dies separated by insulating spacers. The width and length of this filter was 6 mm and 3 cm, respectively and the thickness was around 3 mm.

The resolving power of quadrupole filters is given by Equation 2.6 [19].

$$\frac{m}{\Delta m} = \frac{f^2 L^2 m}{40 q V_a} \tag{2.6}$$

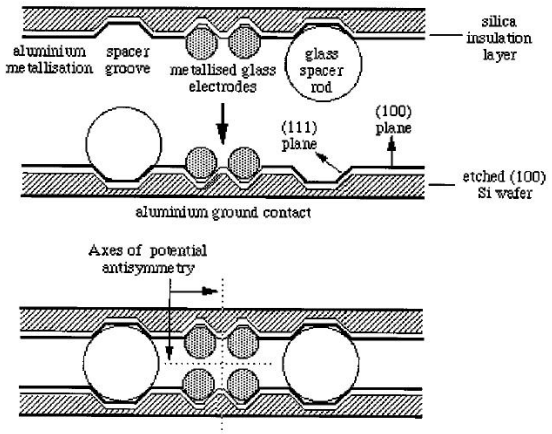

(a)

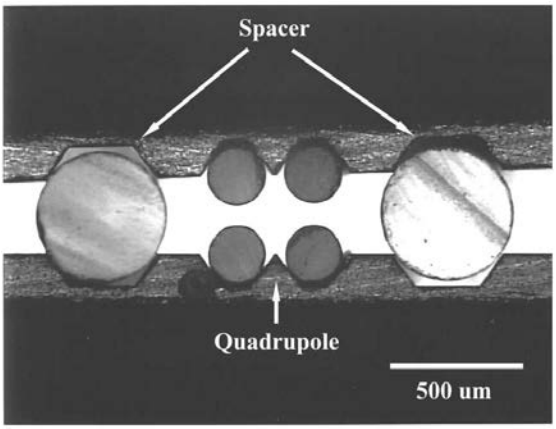

(b)

Figure 2.8. (a) Schematic of a micromachined quadrupole mass filter showing some of the assembly steps and (b) optical picture of a micromachined quadrupole mass filter, from [7].

where f is the applied frequency, L is the length of the quadrupole filter, V_a is the acceleration voltage, and q is the charge of an electron. From this equation, it is clear that scaling down of the size (L) requires an increase in the operation frequency to maintain the same resolution.

The maximum mass (m_{max}), which can be resolved by a quadrupole filter, depends

on the rf voltage (V_{max}) applied between adjacent rods as given by Equation 2.7 [19].

$$V_{max} = 14.46 \times 10^{-8} m_{max} f^2 (r_0)^2 \tag{2.7}$$

where r_0 is the radius between quadrupoles (see Figure 2.7). By reducing the diameters of the quadrupoles by micromachining (namely, reducing r_0), it is possible to reduce the maximum voltage required to resolve m_{max} at the same frequency. To obtain good resolving power, high frequency and low voltage is required, but this condition will decrease the mass range (m_{max}) at the same time. In addition, in terms of miniaturization, reducing r_0 increases the mass range, but reducing L decreases the resolving power. Therefore, there is a trade-off between the mass range and the resolution in terms of the operation and the miniaturization.

Figure 2.9 shows the mass spectrum of a mixture obtained from a micromachined quadrupole with a 3 cm lens driven at an rf frequency of 6 MHz [10]. The resolution was 2.7 amu at 40 amu. This value was worse than that presented by a micromachined Wien filter in Figure 2.6. To improve the resolution, the operational and geometrical parameters should be optimized using Equations 2.6 and 2.7.

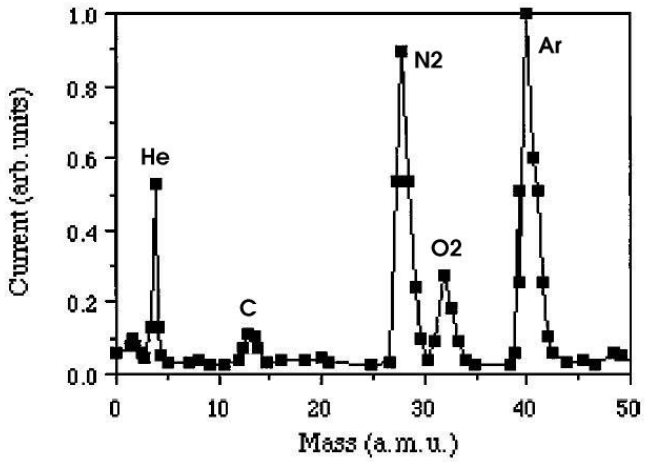

Figure 2.9. Mass spectrum of a mixture of helium, argon, and air obtained from a 3 cm quadrupole mass filter with 500 μm diameter electrodes at 6 MHz, from [10].

Mean Free Path For a mass filter to work properly, the filter area should provide a collision-free environment. Collisions between the sample ions and other atoms either prevent the detector from collecting ions or change the ion path, clouding the mass resolution. The average distance traveled by ions between successive collisions is called the mean free path, which depends on the pressure [20].

$$\lambda_{mfp} = \frac{5 \times 10^{-3}}{P} \tag{2.8}$$

where λ_{mfp} is the mean free path in cm and P is the pressure in Torr.

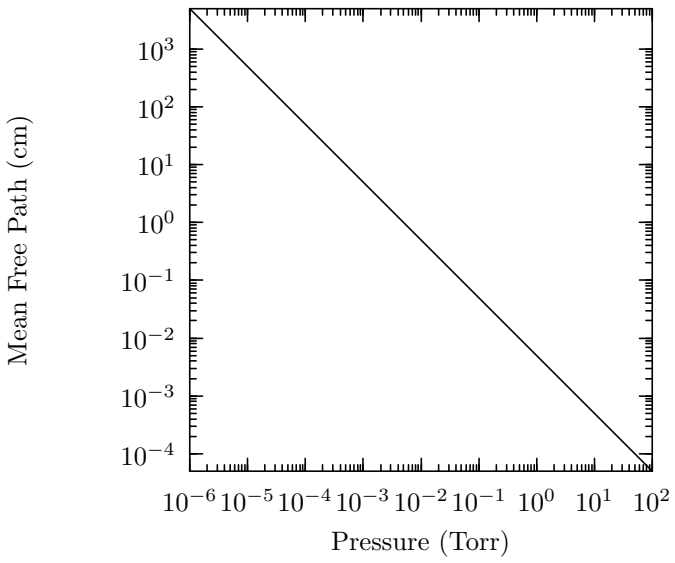

Figure 2.10. Mean free path as a function of pressure.

From Figure 2.10, the advantage of miniaturization of the mass filter is obvious. Scaling down a mass filter from 1 m to 1 cm in length reduces the requirements for the vacuum from 10^{-5} to 10^{-3} Torr. For MEMS mass spectrometer systems, where the mass filters are around 1–3 cm long, the required pressures are in ranges of 1 to 10 mTorr to create a collisionless environment.

2.1.2 Other Components in MEMS Mass Spectrometers

Apart from mass filters, other mass spectrometer components have been fabricated by micromachining. In many cases, these components were integrated with a mass filter. Freidhoff et al. fabricated a sampling orifice, ion optics and a detector array together with a Wien filter by bonding two patterned and metallized silicon wafers [10, 17]. They used a double zoom lens or Einzel lens for the ion optics and Faraday cylinders for the detector array. In particular, a 22 μm spacing between Faraday detector elements was realized by micromachining. As noticed in Equation 2.5, a narrower spacing between the detector elements increases the resolving power of the Wien filter. Faraday cylinders are commonly used as detectors in mass spectrometers [1]. In operation, when ions touch the inside of the cylinder, the ions are neutralized and discharge electrons. By measuring the discharge current, ions can be detected.

Micromachined Ionizers In mass spectrometers, ionizers ionize the sample gas. For MEMS mass spectrometers, thermionic electron emitters [13], plasma electron sources [15], and reverse-bias p-n junctions [21] have been studied for this application.

Thermionic emitters were fabricated using sputtered tungsten films employed as microbridges [11, 13]. When the microbridges are heated by a current, an electron current of around around 7–10 nA was observed. However, this level was not enough to ionize the sample gas and presented a short life-time of less than 1 hour.

To achieve longer lifetimes and generate ions under low vacuum conditions, Siebert et al. developed a plasma electron source [15]. The plasma source was made by bonding three Pyrex glass plates with patterned metal strips on them. These sources generated currents of around 100 μA, which is enough to ionize the sample gas in MEMS mass spectrometers. However, the fabrication was complex and the sources required external input of a rare gas and a piezoelectrically generated

electric spark to ignite the plasma.

In reverse-bias p-n junctions, shallow junctions near the surface can emit high energy electrons into a vacuum and these junctions can be employed as ionizers for MEMS mass spectrometers [14]. The reverse-bias p-n junctions can be integrated on a silicon wafer using standard silicon processing, which enables it to be fabricated with a mass filter directly on a silicon wafer. The fabricated junction demonstrated an emission current of around 1 μA, which was enough to ionize gas molecules [21]. However, the electron emission exhibited instability in operation due to changes in the surface work function. The design and fabrication need to be optimized for long term operation.

2.2 Micromachined Diaphragm Pumps

Conventional vacuum pumps can be broken into two broad classes [20]: gas transfer pumps and entrapment pumps. Gas transfer pumps transfer gas molecules from the pumping chamber to the ambient using either positive displacements or kinetic forces. Diaphragm, rotary, diffusion, and turbomolecular pumps belong to this category. In entrapment pumps, gas molecules are condensed or chemically bonded on walls located inside the chamber.

Young has discussed the possibilities of miniaturizing these conventional vacuum pumps by micromachining [22]. For turbomolecular pumps, high rotor speeds of around 10 million rotations per minute are required. This is impractical for micromachined devices. Diffusion pumps require oil to transfer momentum to the gas molecules. However, the size of a condensed oil droplet can be large enough to clog micromachined components of a few micrometers in size. In addition, diffusion pumps are orientation–sensitive in operation. In entrapment pumps, special adsorption walls and compressors are necessary, which are difficult to micromachine. Hence, it is difficult to directly scale down typical macroscopic vacuum pump by

micromachining.

To date, micropumps have been fabricated to transfer liquids rather than to pump gas. These pumps can be divided into two categories [23]: mechanical and non–mechanical pumps. The mechanical pumps utilize the motion of diaphragms, gears or surface acoustic waves (SAW) to transfer fluid. Nonmechanical pumps are based on physical principles such as elecrohydrodynamics, electrokinetics, thermal transpiration (Knudesn compressor), and magnetohydrodynamics. Among them, diaphragm pumps and Knudsen compressors are ideal candidates for micromachined vacuum pumps [24, 25]. Knudsen compressors utilize thermal transpiration at different temperatures. Theoretically, this device can be miniaturized by micromachining. However, the pump requires creation of numerous tubes of different depths making the fabrication process complicated [22]. Also, the power consumption is high due to incorporation of resistive heaters inside the pump.

In this section, micropumps using diaphragm actuators are reviewed in terms of the pumping principles and actuation to investigate feasibility of fabricating diaphragm vacuum pumps by micromachining. Good reviews of other pumping principles can be found elsewhere [23, 26].

All diaphragm pumps have oscillating diaphragms that create a pressure differential between two regions. This pressure difference causes the fluid to move to the lower pressure region. To control the direction of the flow, diaphragm pumps can be divided into three groups: check–valve pumps, valveless–diffuser pumps, and peristaltic pumps [27]. These micropumps have been designed to manipulate liquids rather than gases [28–30]. There is little reported work on micromachined vacuum pumps. Table 2.1 summarizes characteristics of some diaphragm pumps.

Table 2.1. Typical parameters of diaphragm pumps.

Author[1]	Type	Size[2] (mm)	Actuation Principle	Flow Rate (μl/min)	Pressure[3] (Torr)	Frequency[4] (Hz)	Assembly
van Lintel [31]	check–valve	ϕ50×2	piezoelectric	8	200	3	anodic bonding, gluing
Smits [30]	peristaltic	*	piezoelectric	100	125	15	anodic bonding, gluing
van de Pol [28]	check–valve	13×45×2	thermo–pneumatic	34	100	1	anodic bonding
Zengerle [32]	check–valve	7×7×2	electrostatic	350	230	0.1–6000	anodic and eutectic bonding
Olsson [29]	valveless–diffuser	15×17×1	piezoelectric	2300	550	3000–4000	anodic bonding, gluing
Linnemann [33]	check–valve	7×7×1	piezoelectric	1300	670	200	direct bonding
Shoji [34]	check–valve	20×20×1	piezoelectric	40	110	40	direct bonding
Grosjean [35]	Peristaltic	10×3×2	thermo-pneumatic	4	25	2	direct bonding
Judy [36]	Peristaltic	*	electrostatic	*	*	*	No assembly
Nguyen [37]	Valveless Diffuser	9×9×*	piezoelectric	80	4	110	direct bonding

[1] the first author in the reference
[2] size of the pump
[3] maximum back pressure
[4] typical operation frequency
* information unavailable

2.2.1 Check–Valve Pumps

The first check–valve micropump (shown in Figure 2.11) was demonstrated by Van Lintel et al. The pump consisted of one diaphragm and two passive check–valves. As the diaphragm deflects, compressing the chamber volume, it creates a pressure differential between the inlet and the outlet. When the chamber volume expands, the inlet check–valve opens and the outlet check–valve closes. This causes fluid to flow from the inlet to the chamber. When the chamber contracts, the inlet valve remains closed, but the outlet valve opens, expelling the fluid. This pump

was made using two glass plates and a silicon wafer. Check–valve structures in the form of a ring diaphragm were fabricated on the silicon wafer by anisotropic etching. The wafer was then anodically bonded to the top and bottom glass plates. To actuate the diaphragms, 100∼200 μm thick PZT disks, 1 cm in diameter, were glued on the top glass plate. The pump structure was formed on a 2" wafer. The typical membrane and valve diameters were 12.5 and 7 mm, respectively. A maximum flow rate of 8 μl/min was obtained at 1 Hz with an actuation voltage of 100 V.

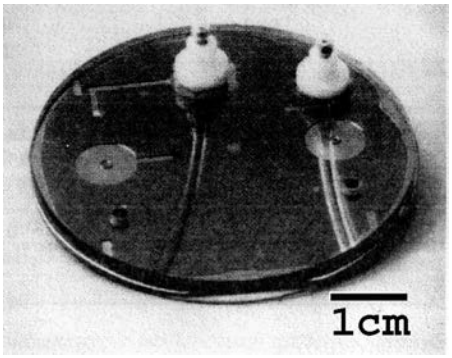

(a)

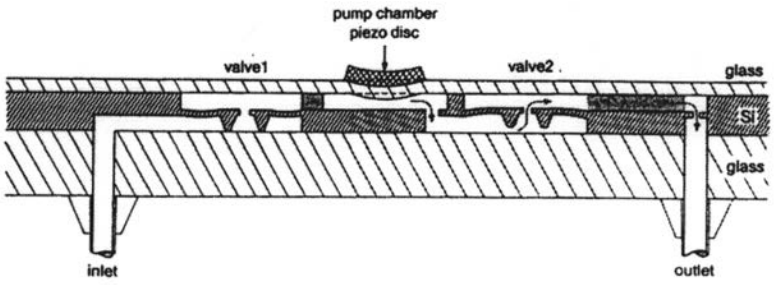

(b)

Figure 2.11. (a) Photo of an assembled check-valve pump and (b) schematic of the pump, from [31].

2.2.2 Valveless–Diffuser Pumps

Valveless–diffuser pumps are basically similar to check–valve pumps. These pumps utilize diffuser/nozzle elements instead of fragile check–valves. The diffuser/nozzle elements are designed to have different resistances to forward and reverse flow [38]. Olsson fabricated valveless-diffuser micropumps using isotropic etching, deep reactive ion etching (DRIE) and anisotropic etching, and thermoplastic replication [29]. Figure 2.12 shows an image of a valveless–diffuser pump as well as the process flow used to fabricate it. The fabrication process consisted of two steps: 1) DRIE for the pump chambers and diffuser elements and 2) anisotropic silicon etching for the inlet and outlet openings. The silicon wafer was then anodically bonded to a glass wafer. Finally, $\sim$ 200 μm thick piezoelectric disks, 3.8 mm in diameter, were manually glued to the glass diaphragms (5 mm in diameter). The size of the pump was 15$\times$17 mm with a thickness of 1 mm. The maximum flow rate was $\sim$2000 μl/min and the maximum back pressure[1] was around 500 Torr. In addition, this pump acted as a gas pump when it was driven at high resonance frequencies.

2.2.3 Peristaltic Pumps

The peristaltic pump is based on the peristaltic motion of serially connected chambers. The principle is similar to the motion of the esophagus while swallowing food. Peristaltic micropumps using piezoelectric disks were first demonstrated by Smits [30]. The pump was fabricated using anisotropic silicon etching for the chamber structures on the front and the connecting channels on the back side (see Figure 2.13). Three piezoelectric disks were glued to the glass diaphragms. Sequential actuation of these piezoelectric diaphragms effected pumping. In Figure 2.13, when the first actuator flexes upward, the first chamber is filled with fluid from the inlet. The fluid in the first chamber will move in to the second chamber when the second actuator is deflected. When the first chamber is closed and the

[1] the maximum back pressure is a pressure against which a pump can flow fluid.

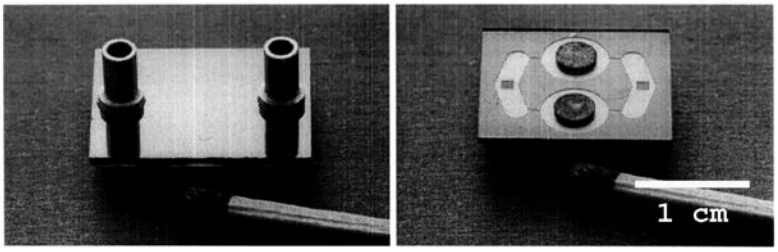

(a)

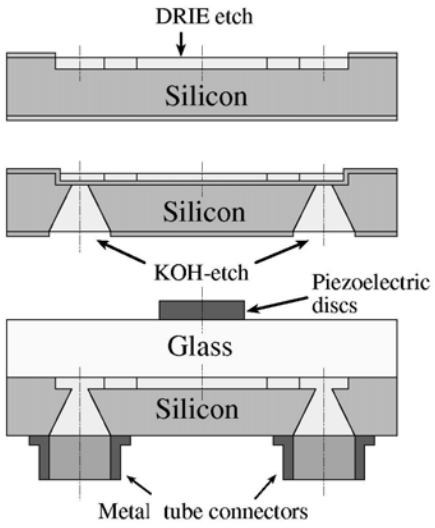

(b)

Figure 2.12. (a) Photo of a valveless diffuser pump and (b) fabrication process of the pump, from [29].

third actuator flexes upward, the fluid will reach the third chamber. Finally, the fluid will move out through the outlet when the third chamber is closed. The maximum pump rate was 100 μl/min at 15 Hz with an actuation voltage of 80 V. The maximum back pressure was about 40 Torr.

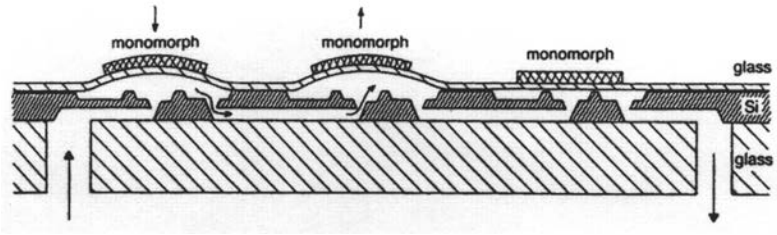

Figure 2.13. Peristaltic pump using three piezoelectric disks, from [30].

2.2.4 Surface Micromachined Peristaltic Pumps

Surface micromachined peristaltic pumps have been reported previously. A group at the University of Minnesota demonstrated fabrication of peristaltic pumps using either piezoelectric or electrostatic actuation [36, 39]. Phosphosilicate glass (PSG) was used as the sacrificial material and the pump structures were released by hydrofluoric acid. It is expected that the pump structures had stiction problems. For pump structures using piezoelectric actuation, it is not clear that the diaphragm actuators could generate enough deflection. The diaphragm actuators consisted of a 1.5 μm thick silicon nitride support and a 0.35 μm thick PZT using d_{31} actuation (where a PZT layer is sandwiched between top and bottom electrodes). As will be described in detail in Chapter 3, to get deflections larger than the thickness of the structures, the piezoelectric layer should expand. However, d_{31} actuation yields radial and tangential contraction. Therefore, the maximum deflection is expected to be limited to less than the diaphragm thickness. Detailed information on the deflections of the diaphragms and performances of the pumps is not available in the literature.

Recently, Xie et al. developed surface micromachined peristaltic pumps using electrostatic actuation [40] (Figure 2.14). Parylene and photoresist were used as the diaphragm and the sacrificial material, respectively. Stiction that occured when the photoresist was removed by acetone was minimized by depositing a thin silicon layer under the photoresist. In this case, after the photoresist was removed, the diaphragms stuck to the bottom structures. However, when the silicon was removed by BrF_3 dry etching, the diaphragms became free-standing. The achieved

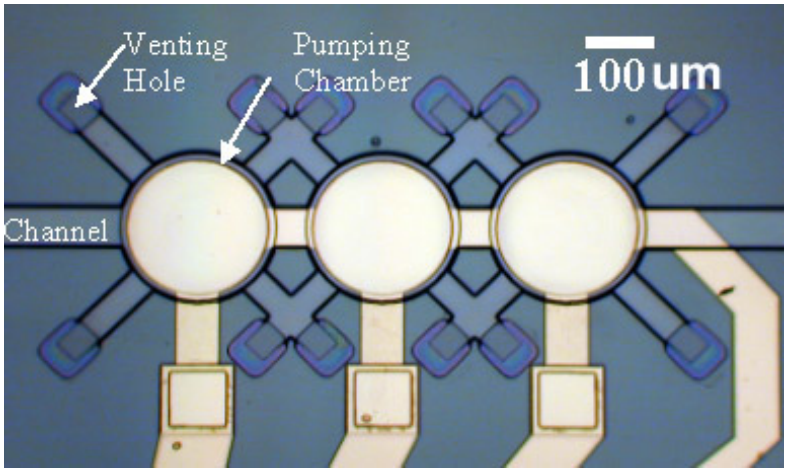

Figure 2.14. Peristaltic pump using electrostatic actuation, the structure was fabricated with a multilayer parylene surface micromachining, from [40].

flow rate was 0.3 nL/min at 60 Hz with an actuation voltage of 120 V.

2.2.5 Actuation Mechanisms for Micropumps

Although most of the diaphragm pumps in the previous sections utilized piezoelectric actuation, there are other actuation mechanisms such as electrostatic, thermopneumatic, and electromagnetic actuation [26].

Electrostatic actuation When a voltage is applied to two parallel metal plates, an attractive force (Coloumbic attraction in origin) is generated between the plates. This electrostatic force is expressed by Equation 2.9 [41].

$$F_e = \frac{1}{2}\frac{\epsilon_r \epsilon_0 A V^2}{d^2} \tag{2.9}$$

where F_e is the electrostatic force, ϵ_r is the relative dielectric constant of the fluid

between the two plates, ϵ_0 is permittivity in vacuum, A is the area of the plates, V is the applied voltage, and d is the distance between the plates.

Zengerle et al. fabricated a micropump using electrostatic actuation (see Figure 2.15) [32]. The actuator unit consists of a diaphragm, an isolation layer, and a counter electrode. When a voltage is applied, the moving diaphragm is attracted to the counter electrode. The isolation layer prevents the two electrodes from forming an electric short circuit. The operation voltage was 200 V at frequencies of kHz. The power consumption was less than 1 mW. The main advantages in electrostatic actuation are the high frequency operation and low power consumption. The drawback lies in the high voltage operation. In addition, the electrostatic force between two electrodes is inversely proportional to the square of the distance between the plates as shown in Equation 2.9. Therefore, the displacements are limited to a few micrometers to obtain a reasonable force.

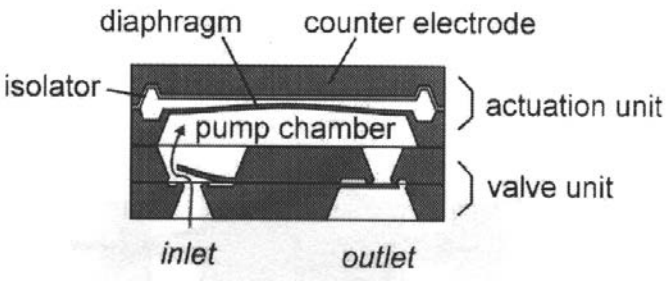

(a)

Figure 2.15. Electrostatic diaphragm pump, from [32].

Thermopneumatic actuation When gas in a closed chamber is heated, a pressure is generated. Assuming the gas behaves like an ideal gas, when the temperature in the chamber changes from T_1 to T_2, the final pressure is expressed by Equation 2.10 [42].

$$P_{T_2} = P_{T_1} \frac{T_2}{T_1} \tag{2.10}$$

When one side of the chamber is flexible, an increased pressure will deform it. When the temperature goes back to T_1, the deformed side will recover its original shape. This is the operating principle of thermopneumatic actuation. Pol et al. fabricated a thermopneumatic pump by bonding three patterned silicon wafers and two pyrex glass plates (see Figure 2.16) [28].

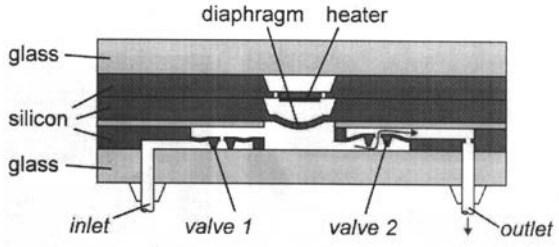

(a)

Figure 2.16. Thermopneumatic diaphragm pump, from [28].

Using an embedded resistive heater, the chamber temperature could be varied. This kind of pump could be operated at a low voltage (below 10 V) [43]. However, the operation frequencies was limited to a few Hz. In thermopneumatic actuation, the heated chamber need some time to cool down because of the long thermal time constant. Typical power consumptions are in range from hundreds of mW to a few W due to energy dissipation by the resistive heaters [27, 35].

Electromagnetic Actuation Electromagnetic force can be used to actuate a diaphragm for micropumps. Dario et al. fabricated a micropump using electromagnetic actuation (see Figure 2.17) [44]. The pump body was fabricated by thermoplastic molding. A permanent magnet was attached to the diaphragm and driven by an embedded microcoil. The pump consisted of a pumping chamber (with a diaphragm) and two passive valves. The electromagnetic force is given by Equation 2.11 [45].

$$F_m = M_z \int \frac{d}{dz} H_z dV \tag{2.11}$$

where F_m is the electromagnetic force, M_z is the vertical component of the magnetization of the permanent magnet, H_z is the vertical component of the magnetic

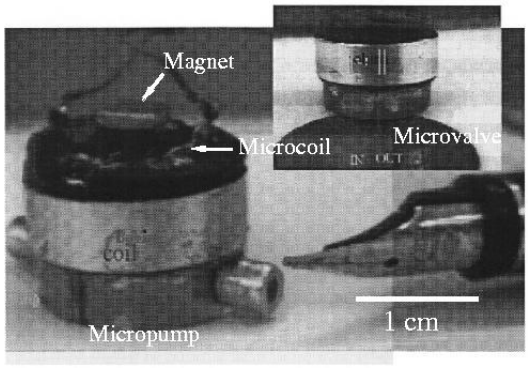

(a)

Figure 2.17. Electromagnetic diaphragm pump, from [44].

field, and V is the volume of the magnet.

Since the electromagnetic force is proportional to the volume of the magnet, there is a limitation on miniaturization of electromagnetic actuators. In addition, the external permanent magnet and the coil made the pump bulky. The pump operated at a frequency of 264 Hz with a low voltage of 14 V. A maximum flow rate achieved was 13 μl/s.

Piezoelectric Actuation Piezoelectric actuation is the most common actuation mechanism for micropumps [29–31]. These micropumps commonly used piezoelectric disks glued on flexible diaphragms. As seen in the previous sections 2.2.1–2.2.3, the actuators were driven at moderate voltages of around 100 V. In addition, these actuators can be operated at high frequencies of kHz [29]. Piezoelectric actuation can be operated with low power consumption due to the high electrical resistance of piezoelectric materials [46].

Table 2.2 summarizes many of the available actuation mechanisms for micropumps [47, 48]. Piezoelectric actuation is suitable for actuators that require fast response and low power consumption.

Table 2.2. Comparison of actuation mechanisms for micropumps.

Actuation	Power consumption	Response time	Energy density	Displacement	Fabrication[1] issues
Electrostatic	Low	Fast	Low	Low	Easy
Thermopneumatic	High	Slow	High	High	Fair
Electromagnetic	High	Fast	Low	High	Difficult
Piezoelectric	Low	Fast	High[2]	Medium[3]	Fair

[1] in terms of miniaturization
[2] Ferroelectric materials with high dielectric constants
[3] Piezoelectric unimorph

2.2.6 Summary

To date many micromachined pumps have been fabricated using various pumping principles. The majority of micropumps are check–valve pumps using piezoelectric disks. In terms of the processes, these pumps were assembled by wafer bonding or gluing. In addition, in many cases, the sizes were too large to be incorporated into around 3×1 cm^2 mass spectrometer chips.

2.3 Piezoelectric Materials for MEMS

Piezoelectricity is the ability of a material to convert mechanical energy to electric energy or electric energy to mechanical energy [49]. Due to its unique energy conversion mechanism, piezoelectric materials have been used for many sensor and actuator applications such as quartz resonators, accelerometers, sonars, motors and ultrasonic transducers for medical diagnosis [50]. With the rapid growth of MEMS fields, piezoelectric films have been investigated for integration into MEMS devices. This section emphasizes lead zirconate titanate films. Comprehensive reviews on thin film piezoelectrics for MEMS are also available elsewhere [51, 52].

2.3.1 Piezoelectric Coefficients for Actuators

The piezoelectric properties of materials are expressed by the following equations using the Einstein summation convention[2] [53]:

$$D_i = d_{ijk}\sigma_{jk} \tag{2.12}$$

$$D_i = e_{ijk}x_{jk} \tag{2.13}$$

$$x_{jk} = d_{ijk}E_i \tag{2.14}$$

$$\sigma_{jk} = e_{ijk}E_i \tag{2.15}$$

where D_i is the electric displacement field, d_{ijk} and e_{ijk} are piezoelectric constants, σ_{jk} is the stress, and x_{jk} is the strain. Here, D_i is a vector, σ_{jk} and x_{jk} are second rank tensors, and d_{ijk} and e_{ijk} are third rank tensors.

Equations 2.12 and 2.13 describe the direct piezoelectric effect, which expresses the piezoelectric conversion from the mechanical domain to the electrical domain. The converse effect is expressed by Equations 2.14 and 2.15. The piezoelectric d_{ijk} coefficient can be converted to e_{ijk} through the stiffness tensor c^E_{jkl} (namely, $e_{ilm} = d_{ijk}\ c_{jklm}$). For actuator applications, the d_{ijk} are useful to calculate the displacements in response to electric fields. The e_{ijk} coefficients are used to estimate the stresses induced by the electric fields.

These piezoelectric coefficients are mathematically expressed as a third rank tensor (Equation 2.16) or in matrix form (Equation 2.17) [53].

[2] when a letter suffix occurs more than once in the same expression, the expression is implicitly summed over all possible values for that suffix.

$$d_{ijk} = \underbrace{\begin{pmatrix} d_{111} & d_{112} & d_{113} \\ d_{121} & d_{122} & d_{123} \\ d_{131} & d_{123} & d_{133} \end{pmatrix}}_{\substack{1^{st}\text{ Layer} \\ i=1}} \underbrace{\begin{pmatrix} d_{211} & d_{212} & d_{213} \\ d_{221} & d_{222} & d_{223} \\ d_{231} & d_{223} & d_{233} \end{pmatrix}}_{\substack{2^{nd}\text{ Layer} \\ i=2}} \underbrace{\begin{pmatrix} d_{311} & d_{312} & d_{313} \\ d_{321} & d_{322} & d_{323} \\ d_{331} & d_{323} & d_{333} \end{pmatrix}}_{\substack{3^{rd}\text{ Layer} \\ i=3}} \tag{2.16}$$

$$d_{ij} = \begin{pmatrix} d_{11} & d_{12} & d_{13} & d_{14} & d_{15} & d_{16} \\ d_{21} & d_{22} & d_{23} & d_{24} & d_{25} & d_{26} \\ d_{31} & d_{32} & d_{33} & d_{34} & d_{35} & d_{36} \end{pmatrix} \tag{2.17}$$

2.3.2 Piezoelectric Materials for MEMS

Piezoelectric materials can be divided into pure piezoelectric (not ferroelectric) or ferroelectric, depending whether or not there are spontaneous electric dipoles that can be reoriented by an applied electric field. In pure piezoelectric materials such as ZnO and AlN, the polarization direction is fixed by the crystal structure and reorientation would require bond breaking. As a result, these materials are usually used in piezoelectric MEMS as textured films in order to exhibit strong piezoelectricity [54]. In the case of ferroelectric materials such as PZT, the dipoles are easily aligned by relatively low electric fields. Therefore, ferroelectric materials become piezoelectric by a poling process.

ZnO and AlN were initially used for piezoelectric MEMS since these materials are simple binary compounds and easily deposited by sputtering on various substrates at a relatively low temperature (below 450 °C) [55, 56]. The low deposition temperature provides a big advantage in compatibility with IC integration [57]. In addition, their low dielectric constants makes them suitable for voltage detection in many sensor applications [58, 59]. However, the low inherent piezoelectric response of ZnO and AlN limits their use for many high performance micromachined actuators, which are required to generate displacements of several micrometers [60].

Lead Zirconate Titanate Films As an alternative, lead zirconate titanate (PZT), which has higher piezoelectric constants than those of ZnO and AlN, has been intensively investigated for MEMS actuators [61, 62].

PZT is a ferroelectric material which has been adapted for many bulk piezoelectric applications. The prototype structure of PZT is a cubic perovskite, as shown in Figure 2.18. The perovskite structure consists of corner-linked oxygen (O) octahe-

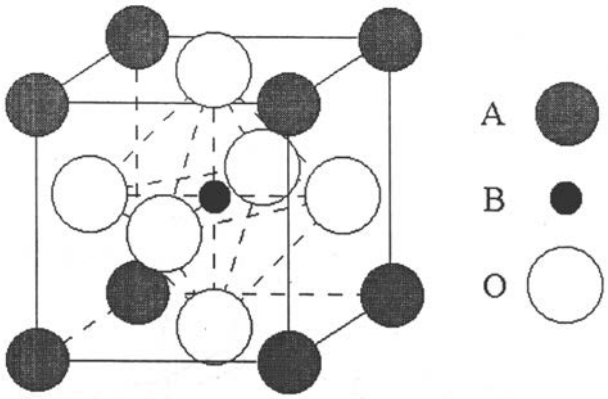

Figure 2.18. Perovskite structure [49].

dra with the smaller Ti or Zr cations (B) occupying sites within the octahedra and larger Pb cations (A) occupying dodecahedral sites between octahedra. The phase diagram of PZT (see Figure 2.19) shows that the structure undergoes a displacive phase transformation into a distorted perovskite structure on cooling. A rhombohedral phase is favorable for zirconium–rich compositions (mol % $PbTiO_3 < 48$) and a tetragonal phase is formed at titanium–rich composition (Mol % $PbTiO_3 > 48$) below the Curie temperature. In the rhombohedral phase, the spontaneous polarization is along one of the <111> directions (eight possible directions) of the cubic unit cell (see Figure 2.20 (a)). In the tetragonal phase, the polarization ap-

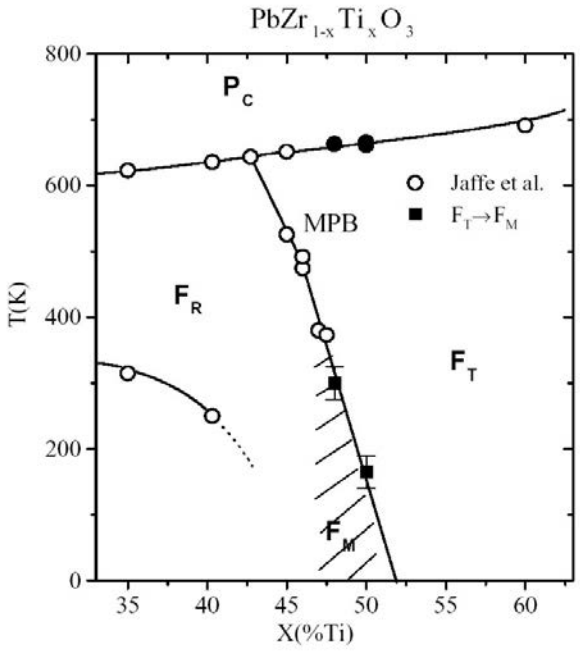

Figure 2.19. Modified phase diaphragm of PZT by Noheda et al. [63]. P_C = paraelectric cubic phase, F_R = ferroelectric rhombohedral phase, F_T = ferroelectric tetragonal phase, and F_M = ferroelectric monoclinic phase.

pears along <001> (six possible directions) (see Figure 2.20 (b)). It is known that the compositions near the morphotropic boundary (MPB) between the rhombohedral and tetragonal phases favor strong piezoelectric effects [49]. More recently, Noheda et al. found a monoclinic phase near the MPB using high–resolution synchrotron x–ray diffraction [65]. This monoclinic phase is interesting since it provides another explanation of the origin of high piezoelectric activity in PZT near the MPB [66].

Initially, PZT films have been investigated for their application to ferroelectric random access memories [67]. The films can be deposited by various methods such

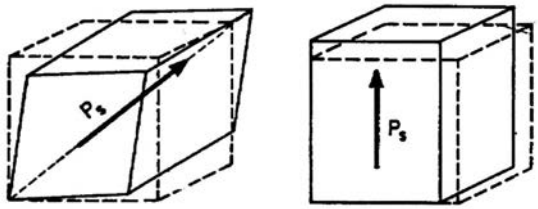

(a) (b)

Figure 2.20. (a) The ferroelectric distortion of a rhombohedral perovskite. The polarization direction is along one of the <111> directions of the prototype unit cell and (b) the ferroelectric distortion of a tetragonal perovskite. The polarization directions is along one of the <100> directions of the prototype unit cell [64].

as sputtering [68], sol–gel [69], metalorganic chemical vapor deposition (MOCVD) [70], and pulsed laser deposition (PLD). However, the deposition temperatures are high, around 600-700 °C. To exhibit good ferroelectric properties, PZT films commonly require noble metals as bottom electrodes. In addition, they need to have a proper buffer layer to enable deposition on silicon, silicon oxide or silicon nitride surfaces due to reactions between Pb and these materials [71]. Despite these problems, the higher piezoelectric response of PZT films (relative to AlN or ZnO) are still advantageous for many microactuators. Table 2.3 summarizes piezoelectric materials and their properties. PZT films have around 10 times larger piezoelectric constants compared to ZnO or AlN films.

Piezoelectric Actuation using PZT Films When a randomly oriented PZT film is poled, the symmetry is a conical symmetry (Curie group: ∞m) [53]. The

Table 2.3. Common piezoelectric materials in MEMS [52].

	ZnO	AlN	PZT
$e_{31,b}$[1],[2] (C/m^2)	-0.57	-0.58	-3.0
$e_{31,f}$[3] (C/m^2)	-0.43∼-0.8	-0.9∼-1.0	-8∼-10
$d_{33,b}$[2] (pC/N)	12.4	5.0	223
$d_{33,f}$ (pC/N)	10∼12	3.4∼3.9	90∼100

[1] e_{31} is another piezoelectric constant, which is proportional to d_{31}.
[2] the subscript b means the piezoelectric constant was measured from a bulk sample.
[3] the subscript f means the piezoelectric constant was measured from the thin film sample.

piezoelectric matrix for the material is simplified by Neumman's law:

$$d_{ijk} = \begin{pmatrix} 0 & 0 & 0 & 0 & d_{15} & 0 \\ 0 & 0 & 0 & d_{15} & 0 & 0 \\ d_{31} & d_{31} & d_{33} & 0 & 0 & 0 \end{pmatrix} \tag{2.18}$$

All piezoelectric constants are zero except d_{31}, d_{33} and d_{15}. These three non–zero piezoelectric constants are important for piezoelectric actuation (see Figure 2.21). In the d_{33} (longitudinal) mode, the motion parallel to the electric field is utilized. The d_{31} (transverse) mode uses the motion perpendicular to the electrical field. In the d_{15} (shear) mode, the electric field is perpendicular to the polarization. In this configuration, the electric field induce a shear strain. For PZT (52/48) ceramics at compositions near the morphotropic boundary, d_{33} = 223 pC/N, d_{31} = - 94 pC/N, and d_{15} = 494 pC/N [49]. Therefore, the largest motions can be generated from d_{15}.

As actuators, unimorph structures, which consist of one piezoelectric and one passive layer, are commonly adapted to amplify displacements. To date, micromachined cantilevers using the d_{31} or d_{33} piezoelectric constant have been fabricated. Kueppers et al. fabricated PZT microactuators, consisting of a PZT layer sandwiched between top and bottom electrodes and polysilicon [72]. For 390 μm long cantilevers, maximum tip deflections of 20 μm were obtained at an applied voltage of 10 V. In contrast, Zhang et al. used the d_{33} piezoelectric constant of PZT to drive their cantilevers. They deposited PZT on silicon nitride without a bottom electrode. The structure was driven using interdigitated transducer (IDT) elec-

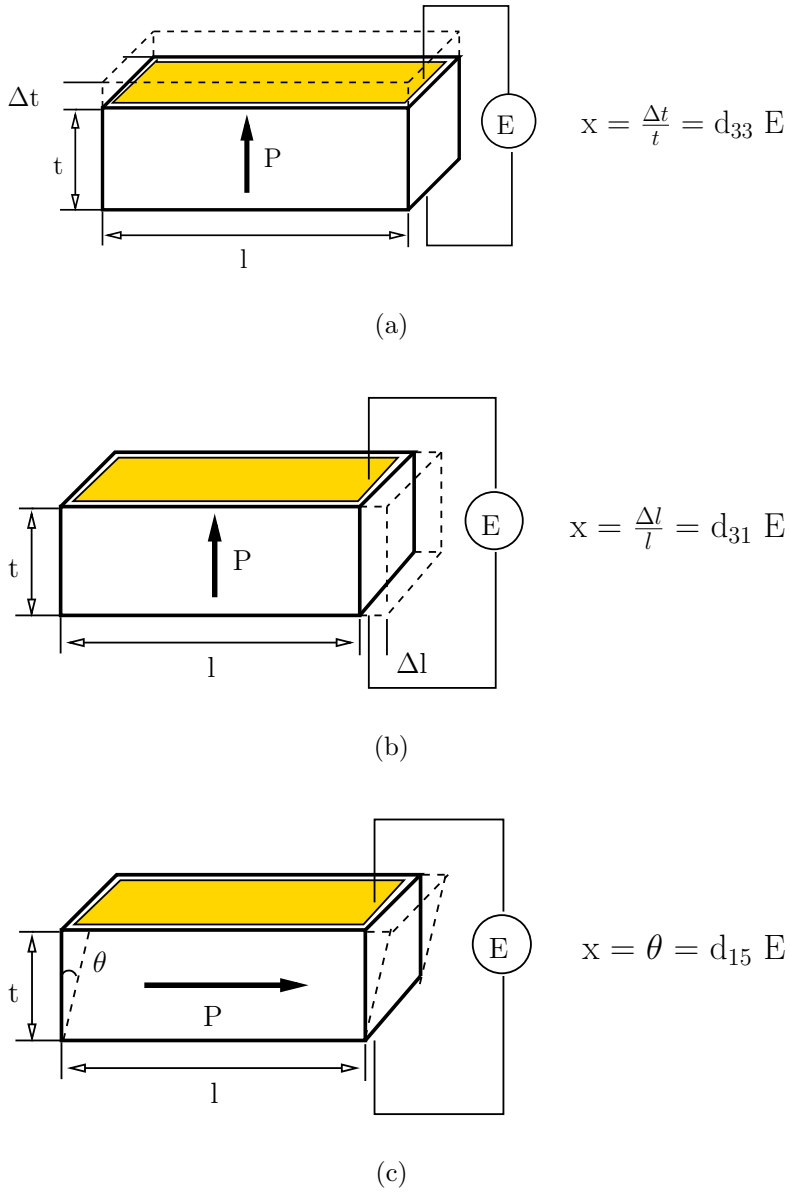

Figure 2.21. Piezoelectric actuations using (a) d_{33}, (b) d_{31}, and (c) d_{15} piezoelectric constant [50].

trodes. A ZrO_2 buffer layer was used to prevent reaction between the PZT and the silicon nitride. 280 μm long cantilevers gave a tip deflection of 30 μm at 100 V [73]. It is clear that PZT is a better piezoelectric material for microactuators than ZnO or AlN.

Piezoelectric Responses in PZT Films Piezoelectric responses in PZT commonly are explained as being due to a combination of intrinsic and extrinsic contributions (see Figure 2.22) [74]. The intrinsic effect results from the homogeneous unit cell deformation by the electric field and the extrinsic effect are the elastic deformations generated by the motions of non-180 ° domain walls and interphase interfaces.

Xu et al. intensively studied the dielectric and piezoelectric response from PZT films with different thicknesses, grain sizes, and preferred orientations [75]. They found that the extrinsic contribution to the dielectric constant of PZT films was mainly attributed to 180 ° domain wall motion. But, ferroelastic non-180 ° domain wall motion was limited. Especially, extrinsic contributions to the piezoelectric response in fine grain PZT films (under 1.5 μm in thickness) were small. To observe substantial nonlinear behavior in the piezoelectric response, the films need to be thicker (> 5 μm).

Piezoelectric Coefficients of PZT Films The piezoelectric properties of thin films are different from those of bulk materials. The main reason lies in the fact that a film is usually clamped to a substrate. Therefore, stresses and strains generated by the piezoelectric film are influenced by the substrate, resulting in effective piezoelectric coefficients different from those for the unclamped material.

Lefki et al. derived an effective piezoelectric coefficient of d_{33} of the film clamped to a substrate from the constitutive equations (see Equation 2.19[3]) for piezoelectric

[3]The equations are in matrix form

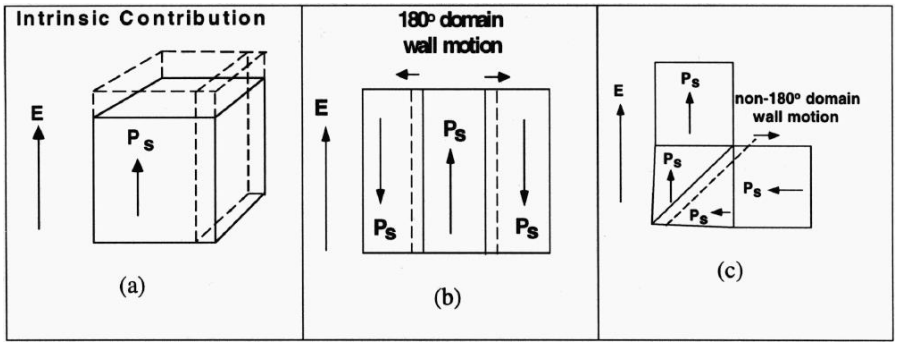

Figure 2.22. (a) Intrinsic contribution due to the response from the lattice, (b) extrinsic contribution due to 180 ° domain wall motion, and (c) extrinsic contribution due to non–180 ° domain wall motion [76].

materials [77]. Muralt expanded this idea for e_{31} [52]. They assumed that the piezoelectric film is clamped on a stiffer substrate and shares a common interface with the substrate in the x–y plane. In this condition, when an electric field is applied to the piezoelectric film, the strains in the x–y plane and the stress along the z–direction will be zero. Therefore, the constitutive equation 2.19 can be simplified to Equations 2.20 and 2.21.

$$x_i = s_{ij}^E \sigma_j + d_{ki} E_k \tag{2.19}$$

$$x_1 = x_2 = (s_{11}^E + s_{12}^E)\sigma_1 + d_{31} E_3 = 0 \tag{2.20}$$

$$x_3 = 2 s_{13}^E \sigma_1 + d_{33} E_3 \tag{2.21}$$

where s_{ij}^E is the compliance measured at constant electric field, E is the electric field, σ is the stress, x is the strain, and the subscripts, 1, 2, 3 mean the x–, y–, and z–directions, respectively.

Using Equations 2.14 and 2.15, the effective piezoelectric coefficients of a piezo-

electric film clamped to a stiff substrate are derived from Equations 2.20 and 2.21.

$$d_{33,f} = d_{33} - \frac{2s_{13}^E}{s_{11}^E + s_{12}^E} d_{31} \tag{2.22}$$

$$e_{31,f} = \frac{d_{31}}{s_{11}^E + s_{12}^E} \tag{2.23}$$

The effective $d_{33,f}$ of a piezoelectric film is smaller than d_{33} since s_{13}^E and d_{31} have negative values and s_{11}^E and s_{12}^E are positive. However, the $e_{31,f}$ is always larger than the e_{31} from the unclamped material. Typical piezoelectric coefficients for PZT films are given in Table 2.3.

References

[1] E.D. Hoffmann, J. Charette, and V. Stroobant, *Mass Spectrometry: Principles and Applications.* John Wiley and Sons, 1996.

[2] H.T. Nagle, R. Gutierrez-Osuna, and S.S. Shiffman, "The How and Why of Electronic Noses," *IEEE Spectr.*, vol. 35, pp. 22 – 31, 1998.

[3] K. Gabriel, "Microelectromechanical Systems Program: Summary of Research Activities," *Advanced Research Projects Agency*, July, 1994.

[4] O.J. Orient, A. Chutjian, and V. Garkanian, "Miniature, High-resolution, Quadrupole Mass–spectrometer Array," *Rev. Sci. Instrum.*, vol. 68, no. 3, pp. 1393–1397, 1997.

[5] T.J. Cornish and W.A. Bryden, "Miniature Time–of–Flight Mass Spectrometer for a Field–Portable Biodetection System," *Johns Hopkins APL Tehnical Digest*, vol. 20, no. 3, pp. 335–342, 1999.

[6] J.C. Kotvas, T.T. Braggins, R.M. Young, and C.B. Freidhoff, *U.S. Patent No. 5,492,867 (Feb. 20, 1996).*

[7] R.R.A. Syms, T.J. Tate, M.M. Ahmad, and S. Taylor, "Design of a Microengineered Electrostatic Quadrupole Lens," *IEEE Trans. on Electron. Devices*, vol. 45, no. 11, pp. 2304–2311, 1998.

[8] N. Sillon and R. Baptist, "Micromachined Mass Spectrometer," *Sens. Actuators B*, vol. 83, pp. 129–137, 2002.

[9] C.B. Freidhoff, R.M. Young, and S. Sriram, *U.S. Patent No. 5,386,115 (Jan. 31, 1995).*

[10] C.B. Freidhoff, R.M. Young, S. Sriram, T.T. Braggins, T.W. O'Keefe, J.D. Adam, H.C. Nathanson, R.R.A. Syms, T.J. Tate, M.M. Ahmad, S. Taylor, and J. Tunstall, "Chemical Sensing using Nonoptical Microelectromechanical Systems," *J. Vac. Sci. Technol. A*, vol. 17, no. 4, pp. 2300–2307, 1999.

[11] H.J. Yoon, J.H. Kim, E.S.Choi, S.S. Yang, and K.W. Jung, "Fabrication of a Novel Micro Time–Of–Flight Mass Spectrometer," *Sens. Actuators A*, vol. 97–98, pp. 441–447, 2002.

[12] R.R.A. Syms, T.J. Tate, M.M. Ahmad, and S. Taylor, "Design of a Micro-engineered Electrostatic Quadrupole Lens," *IEEE Transactions on Electron Devices*, vol. 45, no. 11, pp. 2304–2311, 1998.

[13] D.C. Perng, D.A. Crewe, and A.D. Feinerman, "Micromachined Thermionic Emitters," *J. Micromech. Microeng.*, vol. 2, pp. 25–30, 1992.

[14] R.M. Young, C.B. Freidhoff, T.T. Braggins, and T.V. Congedo, *U.S. Patent No. 5,747,815 (May 5, 1998).*

[15] P. Siebert, G. Petzold, A. Hellenbart, and J. Muller, "Surface Microstructure/ Miniature Mass Spectrometer: Processing and Applications," *Appl. Phys.*, vol. A 67, pp. 155–160, 1998.

[16] E. Constantin and A. Schnell, *Mass Spectrometry.* Chichester, England: Ellis Horwood Limited, 1990.

[17] C.B. Freidhoff and R.M. Young, *U.S. Patent No. 5,536,939 (Jul. 16, 1996).*

[18] H.C. Nathanson, I. Liberman, and C.B. Freidhoff, "Novel Functionality Using Micro–Gaseous Devices," *Proceedings of MEMS '95, Amsterdam, The Netherlands, January 29 – Febrary 2*, pp. 72–76, 1995.

[19] P.H. Dawson, *Quadrupole Mass Spectrometery and its Application.* Elsevier Scientific Publishing Company, 1976.

[20] M. Ohring, *The Materials Science of Thin Films.* London: Academic Press, Inc., 1991.

[21] C. Freidhoff, "Status of the Mass Spectrograph on a Chip (MSOC), Technical R&D Status Report, Advanced Research Projects Agency, 1995."

[22] R.M. Young, "Analysis of a Micromachine Based Vacuum Pump on a Chip Actuated by the Thermal Transpiration Effect," *J. Vac. Sci. Technol. B*, vol. 17, no. 2, 1999.

[23] S. Shoji and M. Esashi, "Microflow Devices and Systems," *J. Micromech. Microeng.*, vol. 4, pp. 157–171, 1994.

[24] R.M. Young and C.B. Freidhoff, *U.S. Patent No. 5,659,171 (Aug. 19, 1997).*

[25] S.E. Vargo, E.P. Muntz, G.R. Shiflett, and W.C. Tang, "Knudsen Compressor as a Micro– and Macroscale Vacuum Pump without Moving Parts or Fluids," *J. Vac. Sci. Technol. A*, vol. 17, no. 4, pp. 2308–2313, 1999.

[26] N. Nguyen, X. Huang, and T.K. Chuan, "MEMS-Micropumps: A Review," *Journal of Fluids Engineering*, vol. 124, pp. 384–392, 2002.

[27] P. Woias, "Micropumps – Summarizing the First Two Decades," *Proceedings of SPIE, Microfluidics and BioMEMS, San Francisco, October 22 – 24*, vol. 4560, pp. 39–52, 2001.

[28] F.C.M. van de Pol, H.T.G. van Lintel, M. Elvenspoek, and J.H.J. Fluitman, "A Thermopneumatic Micropump Based on Micro–engineering Techniques," *Sens. Actuators A*, vol. 21–23, pp. 198–202, 1990.

[29] A. Olsson, "Valve-less Diffuser Micropumps," PhD thesis, Royal Institute of Technology, 1998.

[30] J.G. Smits, "Piezoelectric Micropump with Three Valves Working Peristaltically," *Sens. Actuators*, vol. 15, pp. 153–167, 1988.

[31] H.T.G. Van Lintel, F.C.M. Van de Pol, and S. Bouwstra, "A Piezoelectric Micropump Based on Micromachinig of Silicon," *Sens. Actuators*, vol. 15, pp. 153–167, 1988.

[32] R. Zengerle, S. Kluge, M. Richter, and A. Richter, "A Bidirectional Silicon Micropump," *Proceedings of MEMS '95, Amsterdam, The Netherlands, January 29 – Febrary 2*, pp. 19–24, 1995.

[33] R. Linneman, P. Woias, C.D. Senfft, and J.A. Ditterich, "A Self–Priming and Bubble Tolerant Piezoelectric Silicon Micropump," *IEEE 11th Int. Workshop on MEMS–MEMS '98*, pp. 532–537, 1998.

[34] S. Shoji, S. Nakafawa, and M. Esashi, "Micropump and Sample–Injector for Integrated Chemical Analyzing Systems," *Sens. Actuators A*, vol. 21–23, pp. 189–192, 1990.

[35] C. Grosjean and Y. Tai, "A Thermopneumatic Peristaltic Micropump," *1999 International Conferenece on Solid-State Sensors and Actuators (Transducers '99), Sendai, Japan, June*, 1999.

[36] J.W. Judy, T. Tamagawa, and D.L. Polla, "Surface-Machined Micromechanical Membrane Pump," *in Proceedings of IEEE 4^{th} International Workshop on MEMS*, pp. 182–186, 1991.

[37] N.T. Nguyen, S. Schubert, S. Richter, and W. Dotzel, "Hybrid–assembled Micro Dosing System using Silicon–Based Micropump/Valve and Mass Flow Sensor," *Sens. Actuators A*, vol. 69, pp. 85–91, 1998.

[38] A. Olsson, G. Stemme, and E. Stemme, "Numerical and Experimental Studies of Flat–Walled Diffuser Elements for Valve–less Micropumps," *Sens. and Actuators A*, vol. 84, pp. 165–175, 2000.

[39] D.L. Polla, A.G. Erdman, W.P. Robbins, D.T. Markus, J. Diaz-Diaz, R. Rizq, Y. Nam, H.T. Brickner, A. Wang, and P. Krulevitch, "Microdevices in Medicine," *Annu. Rev. Biomed. Eng.*, vol. 2, pp. 551–576, 2000.

[40] J. Xie, J. Shih, and Y.-C. Tai, "Integrated Parylene Electrostatic Peristaltic Pump," *presented at the Seventh International Symposium on Micro Total Analysis System, Squaw Valley, USA*, 2003.

[41] G. Kovacs, *Micromachined Transducers – Sourcebook*. WCB McGraw Hill, New York, 1998.

[42] D.R. Gaskell, *Introduction to Metallurgical Thermodynamics*. McGraw–Hill, NY, 1981.

[43] O.C. Jeong and S.S. Yang, "Fabrication and Test of a Thermopneumatic Micropump with a Corrugated p+ Diaphragm," *Sens. Actuators A*, vol. 83, pp. 249–255, 2000.

[44] P. Dario, N. Croce, M.C. Carrozza, and G. Varallo, "A Fluid Handling System for a Chemical Microanalyzer," *J. Micromech. Microeng.*, vol. 6, pp. 95–98, 1996.

[45] B. Wagner and W. Benecke, "Microfabricated Actuator with Moving Permanent Magnet," *in Proceedings of MEMS '91, Nara, Japan, January 30 – Febrary 2*, pp. 27–32, 1991.

[46] M. Sitti, D. Campolo, J. Yan, R.S. Fearing, T. Su, D. Taylor, and T. Sands, "Development of PZT and PZN-PT Based Unimorph Actuators for Micromechanical Flapping Mechanisms," *in Proceedings of IEEE Int. Conf. Robotics and Automation, Seoul, Korea, May 21–26*, pp. 3839–3846, 2001.

[47] P.B. Koeneman, I.J. Busch–Vishniac, and K.L. Wood, "Feasibility of Micro Power Supplies for MEMS," *J. Microelectromech. Syst.*, vol. 6, no. 4, pp. 355–362, 1997.

[48] D. Wood, J.S. Burdess, and A.J. Harris, "Actuators and Their Mechanisms in Microengineering," *J. Engineering Science and Education*, vol. 2, pp. 19–27, 1998.

[49] B. Jaffe, W.R. Cook Jr., and H. Jaffe, *Piezoelectric Ceramics*. Academic Press, Inc., 1971.

[50] K. Uchino, *Ferroelectric Devices*. Marcel–Dekker, 1999.

[51] S. Trolier-McKinstry and P. Muralt, "Thin Film Piezoelectrics for MEMS," *accepted (J. Electroceramics (2003))*.

[52] P. Muralt, "PZT Thin Films for Microsensors and Actuators: Where Do We Stand," *IEEE Transactions on Utrasonics, Ferroelectrics, and Frequency Control*, vol. 47, no. 4, pp. 903–915, 2000.

[53] J.F. Nye, *Physical Properties of Crystals*. Oxford University Press, Oxford, 1985.

[54] F.S. Hickernell, "Zinc Oxide Films for Acoustoelectric Device Applications," *IEEE Transactions on Sonics and Ultrasonics*, vol. SU–32, no. 5, pp. 621–629, 1985.

[55] J.G.E. Gardeniers, Z.M. Rittersma, and G.J. Burger, "Preferred Orientation and Piezoelectricity in Sputtered ZnO Films," *J. Appl. Phys.*, vol. 83, no. 12, pp. 7844–7854, 1998.

[56] A. Rodriguez–Navarro, W. Otano–Rivera, J.M. Garcia–Ruiz, R. Messier, and L.J. Pilione, "Development of Preferred Orientation in Polycrystalline AlN Thin Films Deposited by RF Sputtering System at Low Temperature," *J. Mater. Res.*, vol. 12, no. 7, pp. 1850–1855, 1997.

[57] M.J. Vellekoop, C.C.G. Visser, P.M. Sarro, and A. Venema, "Compatibility of Zinc Oxide with Silicon IC Processing," *Sens. and Actuators A*, vol. 23, pp. 1027–1030, 1990.

[58] D.L. Devoe and A.P. Pisano, "Surface Micromachined Piezoelectric Accelerometers (PiXLs)," *J. Microelectromech. Syst.*, vol. 10, no. 2, pp. 180–186, 2001.

[59] S.S. Lee, R.P. Ried, and R.M. White, "Piezoelectric Cantilever Microphone and Microspeaker," *J. Microelectromech. Syst.*, vol. 5, no. 4, pp. 238–242, 1996.

[60] D.L. Devoe and A.P. Pisano, "Modeling and Optimal Design of Piezoelectric Cantilever Microactuators," *J. Microelectromech. Syst.*, vol. 6, no. 3, pp. 266–270, 1997.

[61] C. Lee, T. Itoh, R. Maeda, and T. Suga, "Characterization of Micromachined Piezoelectric PZT Force Sensors for Dynamic Scanning Force Microscopy," *Rev. Sci. Instrum.*, vol. 68, no. 5, pp. 2091–2100, 1997.

[62] P. Muralt, M. Kohli, T. Maeder, A. Kholkin, K.G. Brooks, N. Setter, and R. Luthier, "Fabrication and Characterization of PZT Thin–Film Vibrators for Micromotors," *Sens. Actuators A*, vol. 48, pp. 157–65, 1995.

[63] B. Noheda, J.A. Gonzalo, L.E. Cross, R. Guo, S.-E. Park, D.E. Cox, and G. Shirane, "Tetragonal-to-Monoclinic Phase Transition in a Ferroelectric Perovskite: The Structure of $PbZr_{0.52}Ti_{0.48}O_3$," *Phys. Rev. B*, vol. 61, no. 13, pp. 8687–8695, 2000.

[64] J. Shepard, "The Investigation of Biaxial Stress Effects and the Transverse Piezoelectric d_{31} Characterization of Lead Zirconate Titanate Thin Films," PhD thesis, The Pennsylvania State University, 1998.

[65] B. Noheda, D.E. Cox, G. Shirane, J.A. Gonzalo, L.E. Cross, and S.-E. Park, "A Monoclinic Ferroelectric Phase in the $Pb(Zr_{1-x}Ti_x)O_3$ Solid Solution," *Appl. Phys. Lett.*, vol. 74, no. 14, pp. 2059–2061, 1999.

[66] R. Guo, L.E. Cross, S.-E. Park, B. Noheda, D.E. Cox, and G. Shirane, "Origin of the High Piezoelectric Response in $Pb(Zr_{1-x}Ti_x)O_3$," *Phys. Rev. Lett.*, vol. 84, no. 23, pp. 5423–5426, 2000.

[67] J.F. Scott and C.A. Paz de Araujo, "Ferroelectric Memories," *Science*, vol. 246, pp. 1400–1405, 1989.

[68] I. Kanno, H. Kotera, K. Wasa, T. Matsunaga, T. Kamada, and R. Takayama, "Crystallographic Characterization of Epitaxial $Pb(Zr,Ti)O_3$ Films with Different Zr/Ti Ratio Grown by Radio–Frequency–Magnetron Sputtering," *J. Appl. Phys.*, vol. 93, no. 7, pp. 4091–4096, 2003.

[69] Q.F. Zhou, E. Hong, R. Wolf, and S. Trolier-McKinstry, "Dielectric and Piezoelectric Properties of PZT 52/48 Thick Films with (100) and Random Crystallographic Orientation," *in Proceedings of Materials Research Society Symposium, Boston, USA*, no. 655, 2001.

[70] E. Hong, J.C. Shin, J. Choi, C.S. Hwang, and H.J. Kim, "Preparation and Characterization of $Pb(Zr,Ti)O_3$ Thin Films by Metalorganic Chemical Vapor Deposition Using a Solid Delivery System," *J. Mater. Res.*, vol. 15, no. 6, pp. 1284–1290, 2000.

[71] B. Xu, Y. Ye, L.E. Cross, J.J. Bernstein, and R. Miller, "Dielectric Hysteresis from Transverse Electric Fields in Lead Zirconate Titanate Thin Films," *Appl. Phys. Lett.*, vol. 74, pp. 3549–3551, 1999.

[72] H. Kueppers, T. Leuerer, U. Schnakenberg, W. Mokwa, M. Hoffmann, T. Schneller, U. Boettger, and R. Waser, "PZT Thin Films for Piezoelectric Microactuator Applications," *Sens. Actuators A*, vol. 97–98, pp. 680–684, 2002.

[73] Q.Q. Zhang, S.J. Gross, S. Tadigadapa, T.N. Jackson, F.T. Djuth, and S. Trolier-McKinstry, "Lead Zirconate Titanate Films for d_{33} mode Cantilever Actuators," *Sens. Actuators A*, vol. 105, pp. 91–97, 2003.

[74] S. Li, W. Cao, and L.E. Cross, "The Extrinsic Nature of Nonlinear Behavior Observed in Lead Zirconate Titanate Ferroelectric Ceramic," *J. Appl. Phys.*, vol. 69, no. 10, pp. 7219–7224, 1991.

[75] F. Xu, S. Trolier-McKinstry, W. Ren, B. Xu, Z.-L. Xie, and K.J. Hemker, "Domain Wall Motion and its Contribution to the Dielectric and Piezoelectric Properties of Lead Zirconate Titanate Films," *J. Appl. Phys.*, vol. 89, no. 2, pp. 1336–1348, 2001.

[76] F. Xu, "Longitudinal Piezoelectric Characterization and Domain Wall Contributions in Lead Zirconate Titanate Thin Films," PhD thesis, The Pennsylvania State University, University Park, PA, 1999.

[77] K. Lefki and G.J.M. Dormans, "Measurement of Piezoelectric Coefficients of Ferroelectric Thin Films," *J. Appl. Phys.*, vol. 76, no. 3, pp. 1764–1767, 1994.

Chapter 3

Design–Aspects of MEMS Pump and Diaphragm Actuators

This chapter discusses the design of MEMS peristaltic pumps and piezoelectric diaphragm actuators. The MEMS pump structures are designed to be fabricated by surface micromachining. Piezoelectric diaphragm actuators, which operate the MEMS pumps, utilize ring–shaped interdigitated transducer (IDT) electrodes to generate vertical deflections up to several micrometers. Aspects of fabrication, fundamental mechanics, the properties of piezoelectric materials, as well as the design of MEMS pumps and diaphragm actuators are described in detail.

3.1 Design of MEMS Pump

MEMS devices such as mass spectrometers [1], electron beam optics [2], and gas chromatographs require pumping systems to sample gas or create vacuum in the detector–chambers to provide a collision–free environment. To date, the commer-

cially available pumping systems are over-sized for these kinds of MEMS devices, which need extremely small flow and have tiny detector–chambers. A miniaturized pumping system is needed to enable the whole system to be mounted on a single chip.

Requirements for a pumping system depend on the specific design of the MEMS device. In this study, the pumping system is primarily targeted at a MEMS mass spectrograph on a chip fabricated by Northrop Grumman Corporation [3, 4]. Figure 3.1 shows all the components for a micromachined mass spectrograph on a chip. The system shown does not include electronic and pumping systems. The dimensions of these parts are less than 3×1 cm with a thickness of around 0.5 mm. The length of the mass filter (Wien filter) region is around 1 cm. Reductions in the size, weight, and power consumption over a conventional mass spectrograph of up to a factor of 1000 can be achieved [3]. Hence miniaturization of the pump system is highly desirable to achieve the required pressure in the mass filter. The pump can either be fabricated on the back surface of one of the components or directly attached to one of the MEMS mass spectrograph pieces. Such a combined mass spectrometer chip can be inserted into a hand–held device such as a personal digital assistant (PDA) or mounted on a stationary system to monitor gas molecules present in the environment [5].

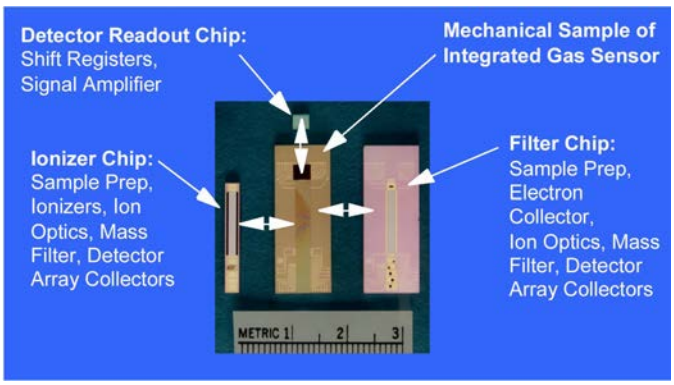

Figure 3.1. Fabricated components for a mass spectrometer on a chip, courtesy C.B. Freidhoff, Northrop Grumman Corp.

3.1.1 Differential Pumping

A mass spectrograph, which has a 1 cm long mass filter region, requires a pressure on the order of 1–10 mTorr to enable collisionless transport of ionized gas molecules, as discussed in Section 2.1.1. To achieve this pressure, the MEMS mass spectrograph can be evacuated by a differential pumping scheme. Figure 3.2 shows a mass filter which has differential pumping chambers in front of the filter region.

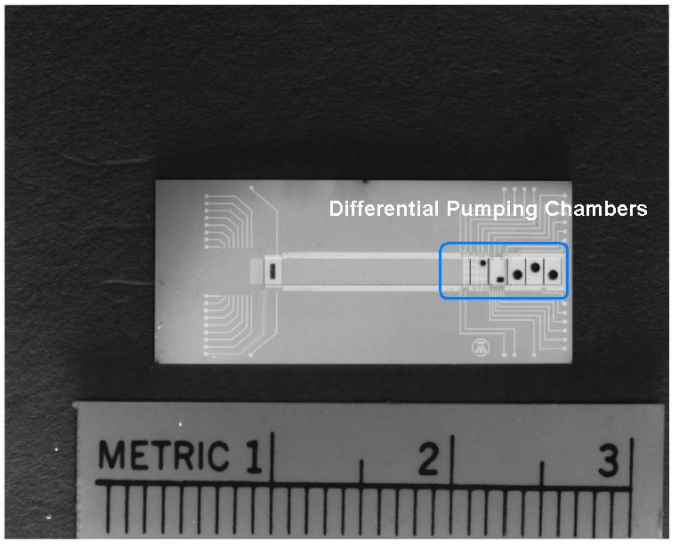

Figure 3.2. Wien filter which has differential pumping chambers (scale in cm) [3].

These chambers are connected by an aperture, which enables the chambers to be evacuated to different levels of pressure using six pumps. The advantage of differential pumping is that most of the gas inside the mass spectrograph is removed at a high pressure. This enables low volume displacement pumps to be used instead of one high volume displacement pump [6]. Figure 3.3 illustrates the advantage of the differential pumping.

To maintain a certain pressure in the chamber, which has a certain amount of gas inflow, the required pumping speed (volume displacement per time) is given by Equation 3.1 [7].

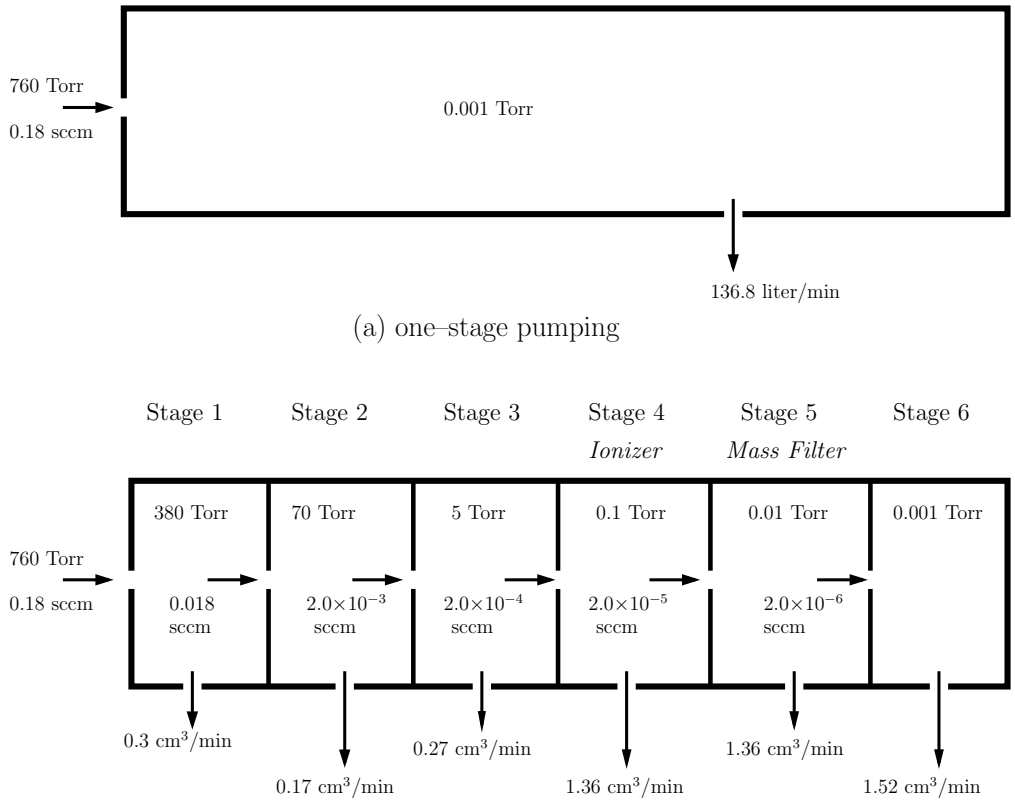

(a) one–stage pumping

(b) six–stage differential pumping

Figure 3.3. (a) Single stage pumping and (b) six–stage differential pumping schemes [6]. Numbers give the chamber pressures and the flow rates.

$$p_0 \frac{dV}{dt} = p \times S \tag{3.1}$$

where p_0 is the pressure at (but outside) the aperture through which the gas is introduced, $\frac{dV}{dt}$ is the gas flow at the aperture, p is the pressure at the inlet of the pumping system and S is the pumping speed.

When a single stage pumping system (see Figure 3.3 (a)) is used to maintain the chamber at 1 mTorr with a gas inflow of 0.18 sccm, a pumping speed of 136.8 liter/min is required. However, in the case of a six–stage differential pumping system (in Figure 3.3 (b)), the required pumping speed is reduced to 1.52 cm^3/min,

a reduction in pumping speed by a factor of 90000. A pumping speed of at least 1 cm^3/min is required for the MEMS mass spectrograph [6].

In a pumping system, the minimum power required to overcome an opposing pressure can be calcuated by the following equation [8].

$$Power = \Delta P \times \frac{\Delta V}{\Delta t} \tag{3.2}$$

where ΔP is the pressure difference (the opposing pressure), and $\frac{\Delta V}{\Delta t}$ is the volume displacement per time. Table 3.1 summarizes the minimum power required for each stage pump for the six–stage differential pumping.

Table 3.1. Minimum power required for each stage pump in Figure 3.3.

Stage[1]	Differential Pressure (Torr)	Volume Displacement (cm^3/min)	Power (mW)
1	380	0.3	0.25
2	310	0.17	0.12
3	65	0.27	0.04
4	4.9	1.36	0.015
5	0.09	1.36	0.0003
6	0.009	1.52	0.00003

The maximum power required in the six–stage differential pump scheme is around 0.25 mW.

3.1.2 MEMS Peristaltic Pump

From the discussion in the previous section, it is clear that the pumping system for a MEMS mass spectrograph should be of comparable size to the other components. In addition, differential pumping, employing multiple pump structures, is needed for the system.

A peristaltic pump, shown in Figure 3.4, was thus designed to satisfy these requirements. The pump structures can be fabricated by surface micromachining. Surface micromachining begins by building up the structure in layers of thin films on the surface of the silicon wafer [9]. This technique usually employs at least two different materials: a structural material and a sacrificial material. By removing the sacrificial material, released structures can be formed. This technique is suitable for making compact MEMS structures without large dead volumes. The pump structure consists of at least five interconnected chambers. Diaphragm actuators are located on top of the chambers.

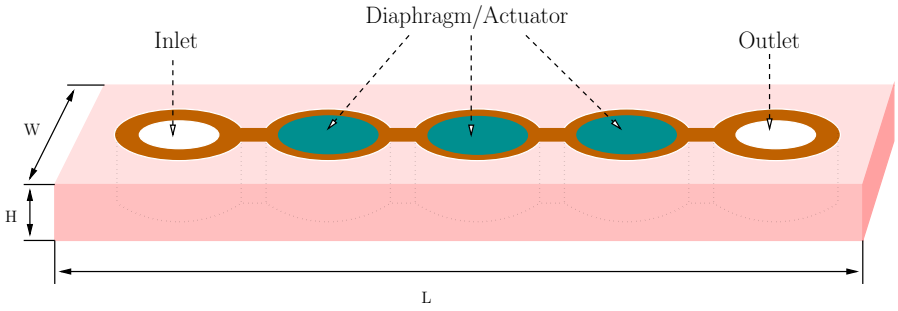

Figure 3.4. Schematic of prototype peristaltic micropump.

The basic operation principle of the peristaltic pump is illustrated in Figure 3.5.

When a diaphragm actuator is open (flat diaphragm), gas is introduced into the chambers. Gas in the chamber moves to the next chamber when the diaphragm is closed (flexed downward). A sequential motion of diaphragm actuators on the chambers creates a volume displacement from the inlet to the outlet. To understand what parameters influence the performance of peristaltic pumps, the volume displacement per cycle is derived. To simplify the problem, the following assumptions are made: 1) there is no in–flow of fluid from the outlet and 2) the fluid is incompressible.

Intially, all chambers are filled with fluid. When chamber 1 is closed, the volume of fluid displaced by the diaphragm actuator will move to both the inlet and chamber 2 (assuming the fluid resistances to the two directions are the same). However, at

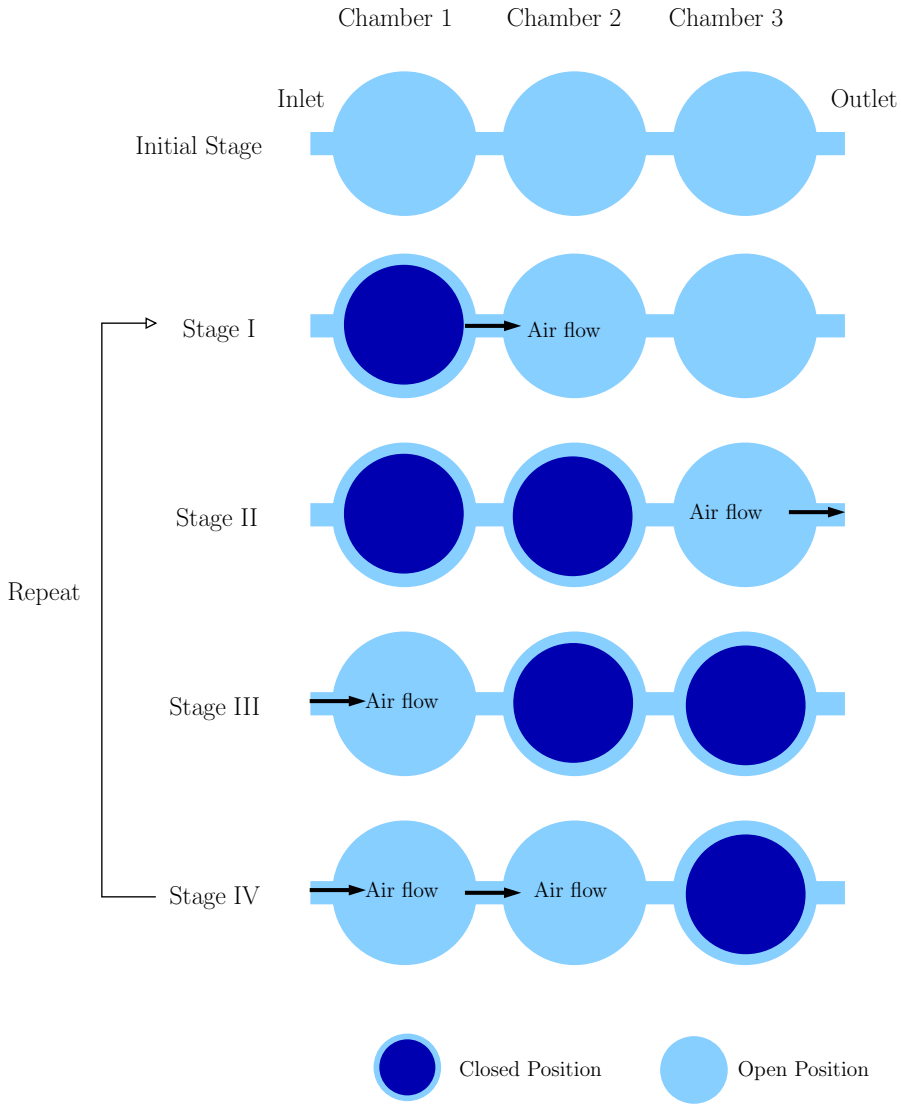

Figure 3.5. Operation of a peristaltic pump.

stage II and III, the fluid will move preferentially from chamber 2 to chamber 3 and from chamber 3 to the outlet since the prior chamber is kept closed to increase resistance to flow to that chamber. From stage I to stage III, the fluid in chambers 1, 2, and 3 will pump out to the outlet. At stage III and stage IV, only chambers 1 and 2 will be refilled from the inlet since chamber 3 is kept closed to prevent inflow from the outlet. Repeating the cycle from stage I to IV, fluid will be transferred from the inlet to the outlet.

Based on the aforementioned operation sequence, the volume displacement caused from the initial stage to stage III was calculated as Equation 3.3.

$$\Delta V = V_C\beta((1-r) + (1-r)^2\beta + \frac{1}{2}(1-r)^2\beta^2) \tag{3.3}$$

where ΔV is the volume displacement per cycle, V_C is the chamber volume, β is the compression ratio (which is the ratio of the stroke volume to the chamber volume) and r is the ratio of the reverse flowing volume to the stroke volume.

After the initial cycle, in the following cycle (from stage I to stage IV), the volume displacement per cycle is given by the following equation.

$$\Delta V = V_C\beta((1-r)(1-\beta) + (1-r)^2 + \frac{1}{2}(1-r)^2\beta^2) \tag{3.4}$$

Assuming an ideal case where β is 1 and r is 0, the volume displacements for Equation 3.3 and for Equation 3.4 are 2.5 and 1.5 V_C, respectively. Half of V_C is a loss to the inlet chamber at Stage I. From Equations 3.3 and 3.4, it is evident that the compression ratio should be increased and the reverse flow should be minimized to enhance the performance of peristaltic pumps. A large chamber and stroke volume is critical to obtain a large volume displacement per cycle.

Pump Speed of Peristaltic Pump The pumping speed of a peristaltic pump (volume displacement per time) is proportional to the stroke volume and operational frequency (i.e., the rate at which the diaphragm actuators are flexed downward). Figure 3.6 shows the chamber volumes required to obtain a certain pumping speed as a function of the operation frequency, assuming the volume displacement per cycle is the same as the chamber volume.

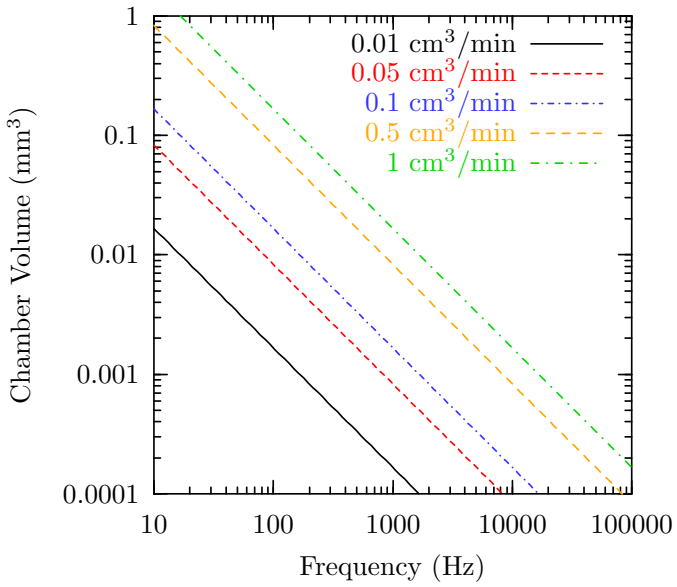

Figure 3.6. Chamber volumes required to obtain various pumping speeds as a function of operation frequency.

The chamber volume is directly related to the size of the pump structure. Therefore, there is a limit on the chamber volume. In this study, target dimensions of the chambers are less than 1 mm in diameter and 3–5 μm in the depth. The chamber volume is around 4×10^{-3} mm^3. To obtain the pumping speed required for the MEMS mass spectrograph (about 1 cm^3/min), the operation frequency is around 4 kHz. Table 3.2 summarizes the required operation frequencies for each stage of the differential pumping shown in Figure 3.3.

Table 3.2. Operation frequencies to satisfy the differential pumping in Figure 3.3 (b) for a peristaltic pump structure with a chamber volume of 4×10^{-3} mm^3.

Pumping Speed (cm^3/min)	0.17	0.27	0.32	1.36	1.52
Operation[1] Frequency (kHz)	0.708	1.12	1.3	5.7	6.3

[1] Assuming the chamber volume is identical to the volume displacement per cycle.

Requirements for the Diaphragm Actuators Diaphragm actuators for the peristaltic pump can be operated at high frequencies (in the kHz range) to keep

the size of the pump structure small. For this reason, electrostatic or piezoelectric actuation is the preferred actuation method. Electrostatic actuators can be fabricated by standard silicon processes [10]. However, electrostatic actuation presents problems with stability due to collapse of the structure to the bottom electrodes over a certain threshold of deflection [9]. In addition, to use electrostatic actuation for the peristaltic pump structure (see Figure 3.4), one electrode should be formed on the bottom of the chamber well. Since the depth of these wells is on order of micrometers, it is difficult to fabricate electrical connections to the bottom electrodes. To avoid these problems, piezoelectric actuation was investigated.

3.1.3 Fabrication Scheme for the Peristaltic Pump

To fabricate the pump structure (Figure 3.4), selection of appropriate piezoelectric and sacrificial materials is important. The fabrication procedure of these structures is as follows: First, cavities for chambers and channels are formed on the silicon wafer. The cavities are then filled with a sacrificial material. Structures for the diaphragm actuators are built up on top of the wafer. Finally, the pump structures are released by removing the sacrificial material.

Piezoelectric material Lead zirconate titanate (PZT) offers a combination of large piezoelectric response and widely available deposition methodologies. 1–7 μm thick PZT films can be deposited by sol-gel methods on 4 inch wafers with thickness deviations of less than 5% [11]. The energy density of PZT films can be calculated by the following equation [8].

$$Energy\ density = \frac{\epsilon_0 \epsilon_r E^2}{2} \tag{3.5}$$

where ϵ_0 is the permittivity in vacuum, ϵ_r is the relative dielectric constant and E is the applied electric field.

As a first approximation, maximum power available from a PZT actuator with a volume of 7.85x10^{-7} cm^3 (for example, the diameter and thickness are 1 mm and 1 μm, respectively) can be calculated assuming that the relative dielectric constant of the PZT is 1000 and the PZT is operated at 1 kHz at 1 MV/cm. The calcuated power is around 35 mW, which is far greater than the power required for the differential pumping (see Table 3.1). Note that this estimation is quite rough, as it does not account for field dependence of the dielectric constant. It is, however, sufficient to show that the energy density available exceeds that required by over an order of magnitude.

Sacrificial Material Silicon dioxide, polymer, and silicon are typical candidate materials for the sacrificial layer. When PZT films are used as the actuator material, the sacrificial material should survive the deposition temperature of PZT films (around 700 °C [12]). This precludes the use of organic sacrificial layers. In addition, the etchant used to remove the sacrificial material should not attack PZT. In the case of SiO_2, etchants based on hydrofluoric acid (HF) are commonly used. Unfortunately, these are also good etchants for PZT. In contrast, silicon is a better sacrificial material for this application. Silicon survives at high temperatures and can be removed readily by xenon difluoride (XeF_2) [9]. XeF_2 is a gas–phase etchant and does not cause any stiction problems during the release process. In addition, PZT survives long exposures to it. Consequently, release of pump structures was achieved with a XeF_2 release.

3.2 Design of Diaphragm Actuator

Piezoelectric diaphragm actuators are essential components in the MEMS pump structure presented in Section 3.1.2. For the pump structure, it is required that thin piezoelectric diaphragms (2 to 4μm) should create large deflections of up to several micrometers.

3.2.1 Basic Principles of Piezoelectric Unimorph

A unimorph structure constructed by bonding together one piezoelectric plate and one elastic layer, is commonly used to achieve large displacement. The basic idea is to convert the piezoelectric transverse strain to large bending displacement in the perpendicular direction due to the constraint of each component in the unimorph structure. In most implementations, the strain utilized in the piezoelectric layer is generated by either d_{31} or d_{33}, as illustrated in Figure 3.7.

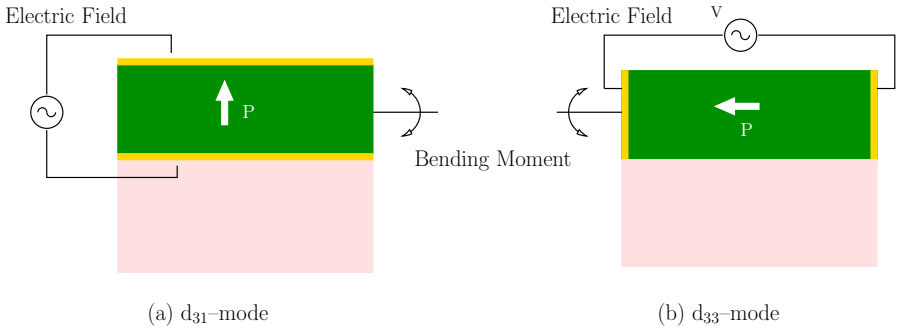

Figure 3.7. Basic bending principle of (a) d_{31}– and (b) d_{33}–mode unimorph.

In the d_{31}–mode, a transverse strain (perpendicular to the polarization axis) is caused by the d_{31} piezoelectric effect. In contrast, the d_{33} piezoelectric constant is used to create a strain parallel to the polarization in the d_{33}–mode unimorph. The available deflection at the tip of a cantilever or center of a diaphragm structure is governed by the structure size, the piezoelectric constant, and the applied electric field [13]. The main disadvantage of the d_{33}–mode unimorph is that it is difficult to increase the length of the structure while maintaining the same electric field. To circumvent this problem, Kugel et al. made d_{33}–mode unimorphs in a complicated way [14] (see Figure 3.8). They stacked piezoelectric plates poled along their thickness such that adjacent plates had polarization in opposing directions. Metal electrodes were formed on the surface of the stack in such a way that the voltage applied to these electrodes produces the same piezoelectric strain in each of the piezoelectric segments comprising the stack. Finally, the stack is bonded onto a

metal plate.

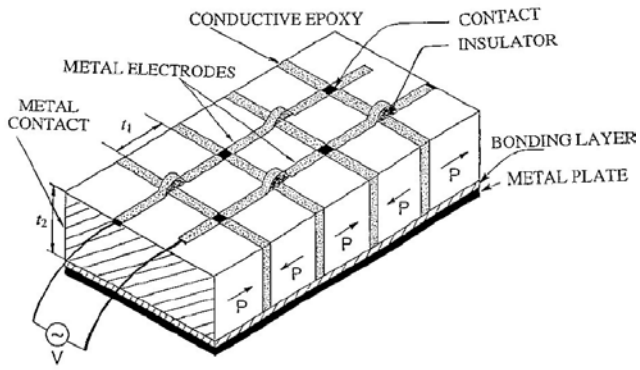

Figure 3.8. d_{33}–mode unimorph structure [14].

When the piezoelectric layer in a unimorph expands or contracts in response to an electric field, the structure flexes. Depending on the clamping condition of the unimorph, the direction of bending in response to a strain in the piezoelectric layer is different. In a cantilever, where only one side is clamped, expansion in the piezoelectric layer makes the free end of the structure bend downward. Contraction causes the opposite effect. In contrast, in a bridge, where both sides are clamped, the expansion makes the middle of the structure deflect up. In all cases, expansion in the piezoelectric layer creates a convex curvature viewed from the piezoelectric side (see Figure 3.9 (a)). Contraction results in a concave curvature (see Figure 3.9 (b)).

3.2.2 Diaphragm Actuators

Based on the discussion in the previous section, diaphragm actuators using PZT films with two designs were studied (see Figure 3.10). In the d_{31}–mode diaphragm actuator, the PZT layer is sandwiched between the top and bottom electrodes. The polarization is perpendicular to the passive layer. When an electric field is applied, the transverse strains generated along the radial and tangential direc-

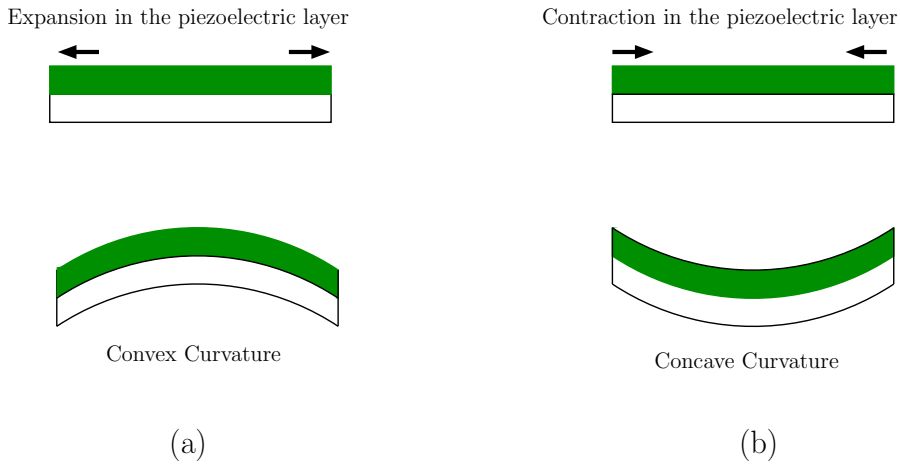

Figure 3.9. Bending curvature of a unimorph when (a) the piezoelectric layer expands or (b) contracts.

tions have the same sign and magnitude. The IDT–mode diaphragm actuator is a derivative of the d_{33}–mode unimorph in Figure 3.7 (b). The diaphragm actuator uses IDT electrodes formed on the top surface of the PZT layer and does not have a bottom electrode. The polarization is parallel to the passive layer. Adjacent segments have opposite polarization directions. In this polarization configuration, when an electric field is applied, the transverse strain along the radial direction is different from that along the tangential direction in sign and magnitude. The strain in the radial direction is caused by the d_{33} piezoelectric effect and the strain in the tangential direction is generated by the d_{31} piezoelectric effect. These two piezoelectric constants have different signs, resulting in strains with different signs in the radial and tangential directions. Hence, it is more reasonable to call this mode an IDT–mode, rather than a d_{33}–mode. As described in section 3.2.1, when the piezoelectric layer expands or contracts, the curvature of the unimorph changes (convex or concave). When the same concept is applied to d_{31}– and IDT–mode diaphragm structures which are clamped at the edges, four different deflection conditions, shown in Table 3.3, can be considered. In the d_{31} mode diaphragm actuator, when the electric field is parallel to the polarization (forward bias), the piezoelectric layer contracts laterally. With an electric field opposite to the polarization (reverse bias), it expands in–plane. In the case of the IDT–mode diaphragm actuator, with forward electric fields, the piezoelectric layer expands in the radial direction and contracts in the tangential direction. Reverse electric fields cause

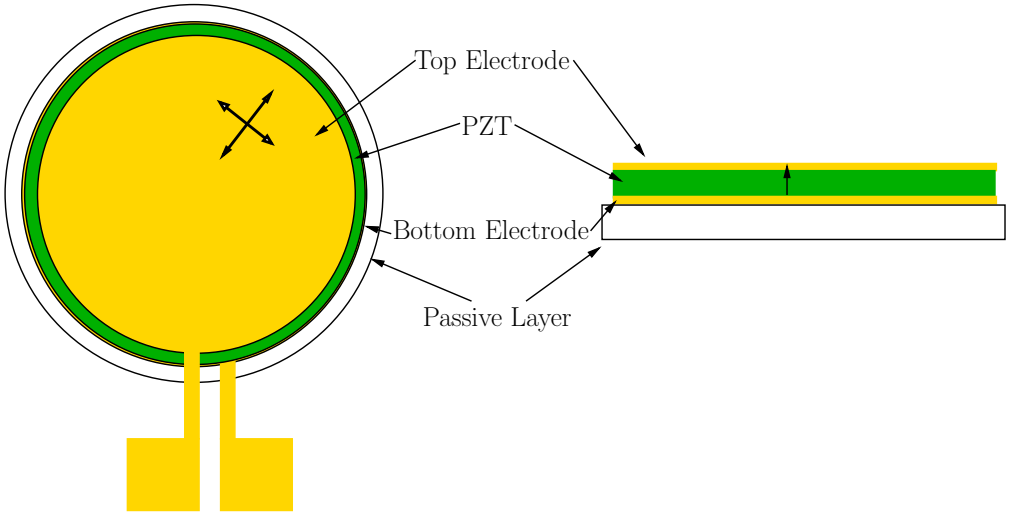

(a)

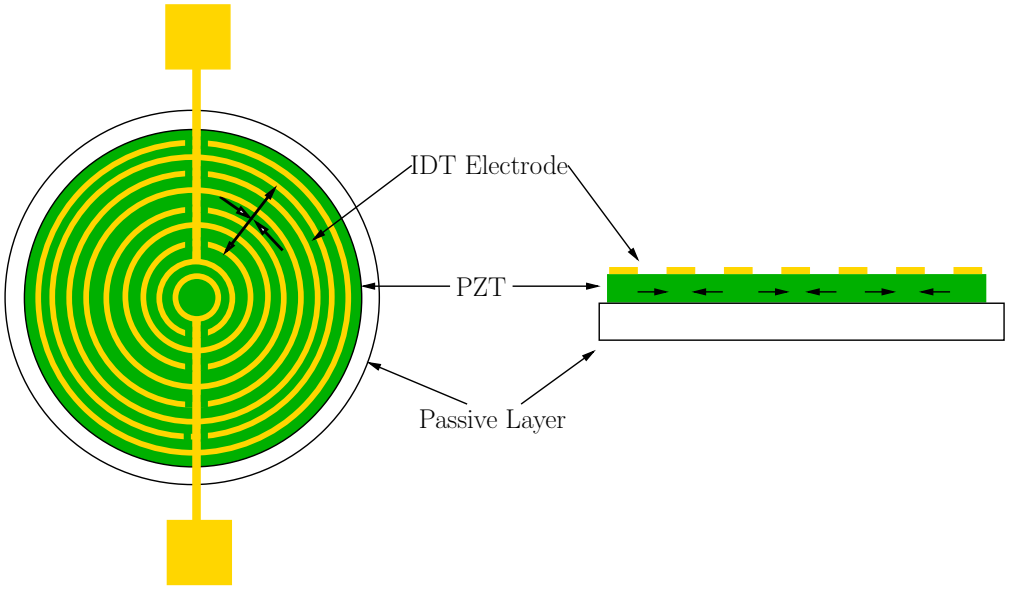

(b)

Figure 3.10. Schematics of (a) d_{31} and (b) IDT–mode diaphragm actuators (not to scale vertically).

opposite results for the IDT–mode diaphragm actuators. Figure 3.11 illustrates the expected deflection shapes of each case in Table 3.3[1].

Table 3.3. Deflections of diaphragm unimorphs.

	Mode	Bias	Radial Direction	Tangential Direction
Case I	d_{31}	Reverse	Expansion	Expansion
Case II	d_{31}	Forward	Contraction	Contraction
Case III	IDT	Forward	Expansion	Contraction
Case IV	IDT	Reverse	Contraction	Expansion

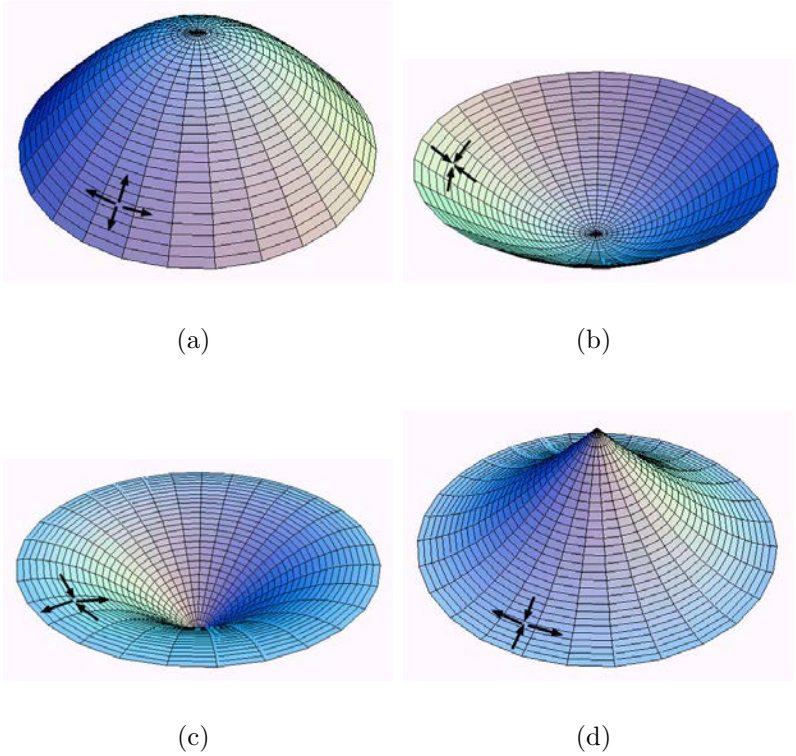

(a) (b)

(c) (d)

Figure 3.11. Deflection shapes of (a) Case I, (b) Case II, (c) Case III, and (d) Case IV (not to scale vertically).

Aspects of Piezoelectric Films PZT films are suitable piezoelectrics for diaphragm actuators due to their strong piezoelectric effect and well developed deposition processes. However, unlike PZT bulk ceramics, PZT films have significant

[1]These are illustrations for deflection shapes obtained by finite element analysis for the stress conditions mentioned in Table 3.3.

residual stress. For example, sol–gel PZT films exhibits around 100 MPa tensile stress on Si substrates [15, 16]. Partially due to this stress, the PZT layers in MEMS structures are often driven at electric fields in excess of the coercive field [17]. A stress (or strain)–electric field curve for a PZT material can be represented as shown in Figure 3.12. For forward biases, the induced stress will continue

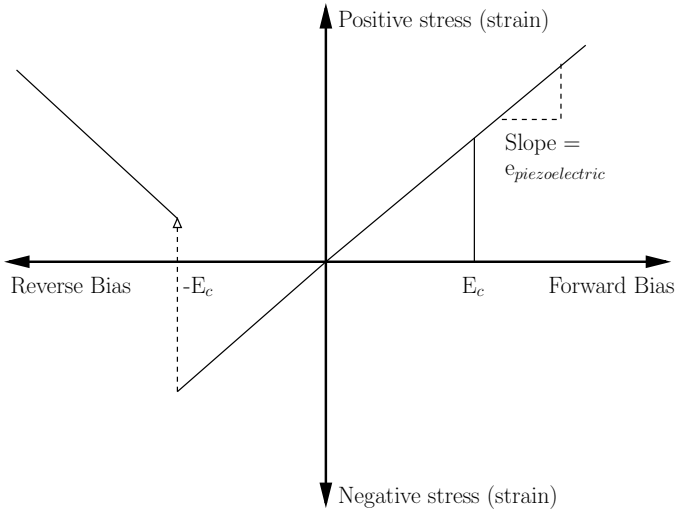

Figure 3.12. Expected stress–electric field curve of PZT material (drawn for voltage scanned from forward bias to reverse bias).

to increase until the PZT breaks down. In reverse biases, the increase in negative strain is limited since at negative biases above the coercive field, the PZT films are depoled, and subsequently the polarization reorients parallel to the reverse bias. For PZT 52/48 films, e_{31} is -4 to -7 C/m^2 and E_c is usually 40–50 kV/cm [11]. Therefore, the maximum negative stress is in the range of 16–35 MPa. From cases I and IV in Table 3.3, which use reverse bias for deflection, operation is limited to electric fields less than the coercive field. Therefore, the deflection will be limited. For cases II and III, which use forward bias, electric fields greater than the coercive field, can be used. The result is that larger deflections can be obtained.

As seen in Section 3.2.1, fabrication of d_{33} unimorphs using PZT bulk ceramics is extremely complicated. Especially, complex wiring of electrodes is required. However, by using thin PZT films as the piezoelectric material and IDT electrodes formed on top of the PZT (see Figure 3.10 (b)) d_{33}–mode unimorph structures

can be fabricated. This advantage comes from using a thin PZT film instead of a thick bulk plate. When an electric field is applied to the IDT electrodes, a uniform electric field is formed under the IDT electrodes up to several micrometers deep. For the bulk PZT plate, such field penetration is not deep enough to bend plates that are hundreds of micrometers thick. However, in thin MEMS structures, this electric field is sufficient to bend the structure. This is clearly seen in finite element modeling of the field distributions in a model system, where IDT electrodes were placed on a PZT sample (see Figure 3.13). This figure presents the x–directional component of the electric field distribution, which is important to use the d_{33} piezoelectric constant, along an x-y plane through a PZT layer with IDT electrodes with 10 μm IDT spacing and width. In this modeling, the relative dielectric constants of PZT and air were fixed to 850 and 1 (in reality, dielectric constants of materials are a function of the applied electric field. Therefore, for a more accurate modeling, changes in the dielectric constants in response to applied electric fields should be considered.), respectively and the applied voltage difference between the two IDT electrodes was 10 V. As shown in the figure, the electric field in the x–direction is strong at a depth of 3 μm into the PZT. At depths over 9 μm, the electric field decreases by around a factor of 4. This electric field distribution through the piezoelectric layer determines which fraction of the piezoelectric layer can be active. As the IDT spacing increases, the penetration depth of the electric field will be enhanced. However, at the same time, the voltage required to generate the same electric field is increased. Hence, a unimorph structure consisting of a piezoelectric thin film and a thin passive layer can deflect, unlike unimorph structures made from the bulk piezoelectric material.

3.2.3 Finite Element Analysis

For a small deflection (less than the thickness of the structure) in an edge clamped diaphragm structure, when the diaphragm deflects downwards, material above the neutral axis[2] experiences compressive strain [18]. Tensile strain is induced

[2]For a small deflection, the neutral axis remains without deformation.

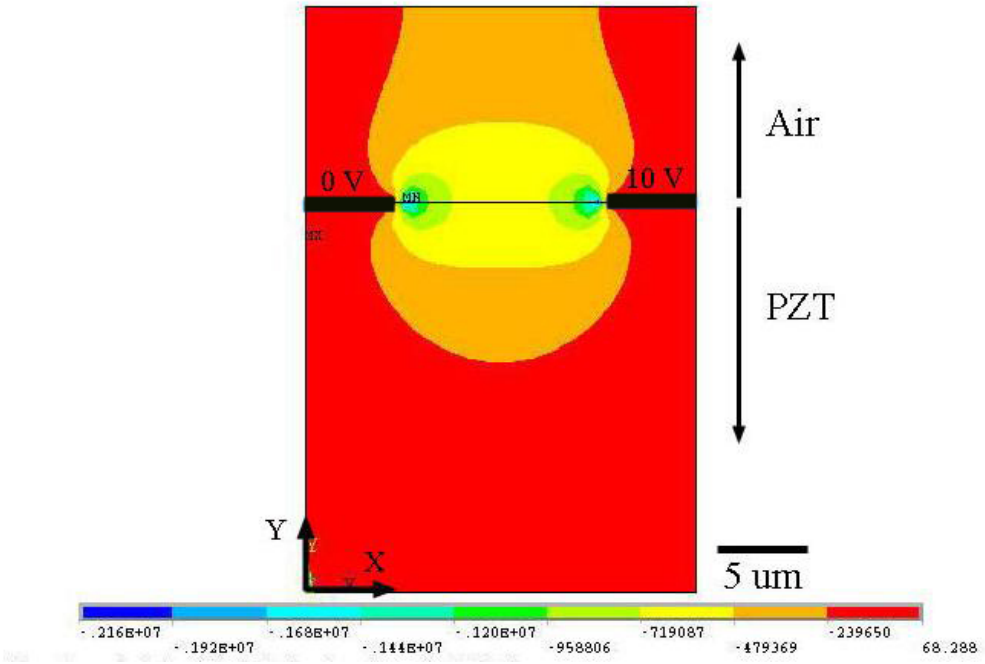

Figure 3.13. Electric field distribution in x–direction of PZT with IDT electrodes.

below the neutral axis. However, for large deflections (larger than the thickness of the structure) stretching of the diaphragm structure occurs [18]. As a result the structure experiences tensile strain.

The deflection modes, cases II and III, result in deflection under forward biases. However, there is a fundamental difference between the two modes. In case II, which uses only the d_{31} piezoelectric constant, the PZT layer contracts with forward biases. In case III, which uses both d_{33} and d_{31} piezoelectric constants, the PZT layer expands in the radial direction and contracts in the tangential direction with forward bias. It is clear that case II, which uses compressive strain, is not suitable for obtaining large deflection over the thickness of the structures.

For case III, which uses both expansion and contraction, it is not clear a priori whether it is possible to get large deflections. To clarify this, a finite element model (shown in Figure 3.14) was made. The radius of the diaphragm (r_d) was 500 μm

and the radius of the active (piezoelectric) layer (r_a) was 400 μm. The structures were modeled using Shell 99 elements, which allow the use of multilayers [19]. A thickness of 1 μm was used for both the passive and active layer. The Young's modulus and Poisson's ratio are also assumed to be the same for the passive and active layer. A Young's modulus of 100 GPa and Poisson's ratio of 0.3 were assumed. The structure was clamped at the boundary. Stress in the active region was varied from 1 to 50 MPa. For comparison, the d_{31}–mode diaphragm (case II) was simulated together with the IDT–mode diaphragm. For the d_{31}–mode diaphragm, a tensile stress was applied to create contractions of equal magnitude in both radial and tangential directions. For the IDT–mode diaphragm, the applied stress in the radial direction was compressive (to create expansion) and the stress in the tangential direction was tensile and the value was half of the stress in the radial direction to simulate the ratio of d_{31} to d_{33} (0.5) [20]. The solutions were obtained by Newton-Raphson technique with an option for large deflection [19]. These stress conditions are expected to simulate the situations of case II and case III.

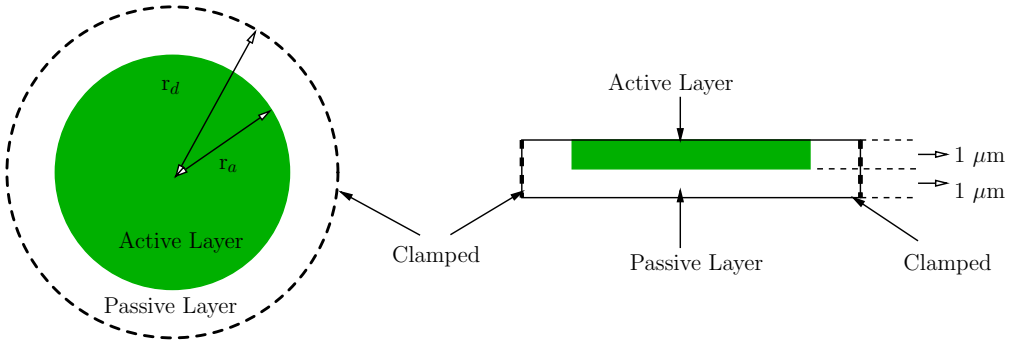

Figure 3.14. Finite element model to simulate d_{31}– and IDT–mode diaphragm actuators: (a) plane–view and (b) cross–sectional view.

Figure 3.15 shows the resulting deflection shapes for cases II and III when a stress of 10 MPa is applied in the radial direction. (Note: as described above, for case II, the stresses in the radial and tangential directions were both 10 MPa. In case III, the radial stress was -10 MPa and the tangential stress was 5 MPa.) The results

are in agreement with the deflection shapes presented in Figure 3.11.

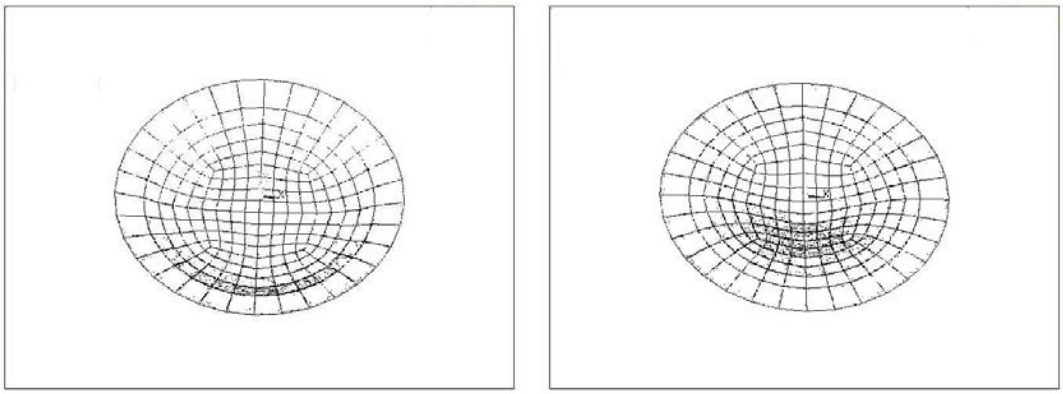

(a) (b)

Figure 3.15. Deflection shapes of (a) Case II and (b) Case III with 10 MPa radial stress.

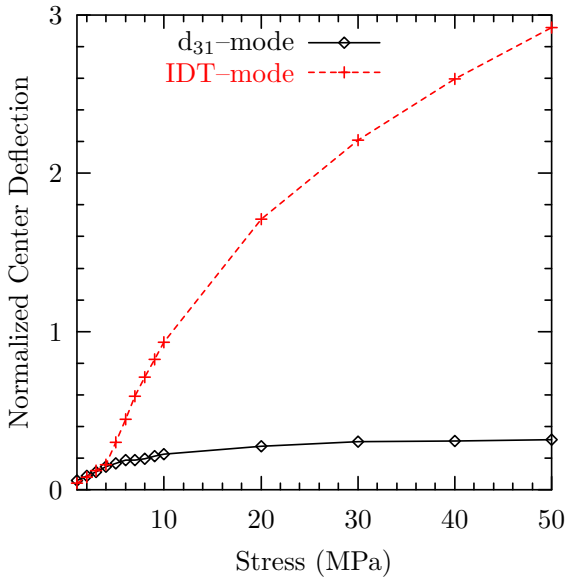

Figure 3.16. Normalized center-deflections of (a) d_{31}–mode (Case II) and (b) IDT–mode (Case III) as a function of the radial stress.

Figure 3.16 shows the center deflections normalized by the diaphragm thickness (2 μm) as a function of applied stress in the active region. For case II, the deflection saturated to a value of around one third of the thickness of the structure. It is interesting to note that this deflection corresponds to the small deflection condition. However, in case III, it is possible to obtain deflections larger than the thickness

of the structures. These results prove that d_{31}–mode, which uses contraction in the piezoelectric layer, is not useful for obtaining large deflections in fully clamped structures and that the IDT–mode is suitable to generate large deflections.

3.3 Conclusions

The MEMS mass spectrographs, which use differential pumping, require a pumping speed of 1 cm^3/min. To achieve this pumping speed with diaphragm actuators (1 mm in diameter), diaphragm actuators should be operated at kHz frequencies. For this purpose, piezoelectric actuation is appropriate. To generate large deflections, diaphragm actuators can be actuated by ring–shaped IDT electrodes.

References

[1] D.H. Holkeboer, T.L. Karandy, F.C. Currier, L.C. Frees, and R.E. Ellefson, "Miniature Quadruple Residual Gas Analyzer for Process Monitoring at milliTorr Pressures," *J. Vac. Sci. Technol. A*, vol. 16, no. 3, pp. 1157–1162, 1998.

[2] M.A. McCord, T.H.P. Chang, D.P. Kern, and J.L. Speidell, "A Novel Scanning Tunneling Microscope Controlled Field Emission Microlens Electron Source," *J. Vac. Sci. Technol. B*, vol. 7, no. 6, pp. 1851–1854, 1989.

[3] C.B. Freidhoff, R.M. Young, S. Sriram, T.T. Braggins, T.W. O'Keefe, J.D. Adam, H.C. Nathanson, R.R.A. Syms, T.J. Tate, M.M. Ahmad, S. Taylor, and J. Tunstall, "Chemical Sensing using Nonoptical Microelectromechanical Systems," *J. Vac. Sci. Technol. A*, vol. 17, no. 4, pp. 2300–2307, 1999.

[4] C.B. Freidhoff, R.M. Young, and S. Sriram, *U.S. Patent No. 5,386,115 (Jan. 31, 1995).*

[5] K. Gabriel, "Microelectromechanical Systems Program: Summary of Research Activities," *Advanced Research Projects Agency*, July, 1994.

[6] C.B. Freidhoff, *Private Communication*, 2003.

[7] M. Ohring, *The Materials Science of Thin Films.* London: Academic Press, Inc., 1991.

[8] P.B. Koeneman, I.J. Busch–Vishniac, and K.L. Wood, "Feasibility of Micro Power Supplies for MEMS," *J. Microelectromech. Syst.*, vol. 6, no. 4, pp. 355–362, 1997.

[9] G. Kovacs, *Micromachined Transducers – Sourcebook.* WCB McGraw Hill, New York, 1998.

[10] J.W. Judy, T. Tamagawa, and D.L. Polla, "Surface-Machined Micromechanical Membrane Pump," *in Proceedings of IEEE 4^{th} International Workshop on MEMS*, pp. 182–186, 1991.

[11] R. Wolf, "Temperature Dependence of the Piezoelectric Response of Lead Zirconate Titanate Films for MEMS Applications," Master's thesis, The Pennsylvania State University, 2001.

[12] Q.F. Zhou, E. Hong, R. Wolf, and S. Trolier-McKinstry, "Dielectric and Piezoelectric Properties of PZT 52/48 Thick Films with (100) and Random Crystallographic Orientation," *in Proceedings of Materials Research Society Symposium, Boston, USA*, no. 655, 2001.

[13] Q.M. Wang, Q. Zhang, B. Xu, R. Liu, and L.E. Cross, "Nonlinear Piezoelectric Behavior of Ceramic Bending Mode Actuators under Strong Electric Fields," *J. Appl. Phys.*, vol. 86, no. 6, pp. 3353–3360, 1999.

[14] V.D. Kugel, S. Chandran, and L.E. Cross, "Caterpillar-Type Piezoelectric d_{33} Bimorph Transducer," *Appl. Phys. Lett.*, vol. 69, pp. 2021–2023, 1996.

[15] G.A.C.M. Spierings, G.J.M. Dormans, W.G.J. Moors, M.J.E Ulenaers, and P.K. Larsen, "Stresses in Pt/Pb(Zr,Ti)O_3/Pt Thin–Film Stacks for Integrated Ferroelectric Capacitors," *J. Appl. Phys.*, vol. 17, no. 2, pp. 1926–1933, 1995.

[16] B.A. Tuttle, J.A. Voigt, T.J. Garino, D.C. Goodnow, R.W. Schwartz, D.L. Lamppa, T.J. Headly, and M.O. Eatough, "Chemically Prepared Pb(Zr,Ti)O_3 Thin Films: The Effects of Orientation and Stress," *in Proceedings of the 8^{th} International Symposium on Applications of Ferroelectrics*, pp. 344–348, 1992.

[17] Q.Q. Zhang, S.J. Gross, S. Tadigadapa, T.N. Jackson, F.T. Djuth, and S. Trolier-McKinstry, "Lead Zirconate Titanate Films for d_{33} Mode Cantilever Actuators," *Sens. Actuators A*, vol. 105, no. 1, pp. 91–97, 2003.

[18] S.P. Timoshenko and S. Woinowsky–Krieger, *Theory of Plates and Shells*. Singapore: McGraw–Hill, 1959.

[19] *ANSYS 5.5 manual, ANSYS, Inc., Canonburg, PA, 1998.*

[20] A.J. Moulson and J.M. Herbert, *Electroceramics*. Chapman and Hall, London, 1990.

Chapter 4

Processing and Characterization of Zirconia and PZT Films

Ferroelectric or dielectric films have be deposited by various methods such as pulsed laser deposition (PLD), metalorganic chemical vapor deposition (MOCVD), sputtering, and chemical solution deposition [1–4]. Each method has its own advantages and disadvantages. In terms of capability of large–area deposition, MOCVD, sputtering and sol-gel methods are more competitive than others. Generally, MOCVD can provide good coverage on steps and trenches with high–aspect ratios and uniformity in the thickness and composition throughout the wafers. However, low deposition rate limits its use to grow relatively thin (< 1 μm) films [2]. Sputtering can be utilized to control film morphologies and provide high deposition rates. In some cases, high stresses are generated in films due to ion bombardment, which can lead to distortion in micromachined structures [3]. Compared to these two techniques, chemical solution deposition is useful for depositing high quality ferroelectric films with relatively low levels of tensile stress (100–200 MPa) for thicknesses up to and greater than 7 μm [5]. For this reason, a sol-gel technique was chosen to deposit zirconia and 1.6–3.0 μm thick PZT films in this study.

This chapter describes the deposition processes and characterization of zirconia and PZT films. The main focus was to deposit crack–free 1.6 μm–3.0 μm thick PZT films on silicon wafers with thermally grown silicon dioxide. Zirconia films were used as buffer layers between the PZT films and the SiO_2 layers. In addition, zirconia layers were also used as protective layers during the XeF_2 release process and as passive layers in unimorph structures instead of thermal SiO_2. Both zirconia and PZT films were deposited by the sol–gel method on 4–inch wafers. The physical and electrical properties of these films were then characterized. The development of residual stresses in the films deposited on silicon wafers is discussed in detail.

4.1 Zirconia Film Preparation

Zirconia is a chemically stable material, which has a high melting point (>2370°C) [6]. The inert nature of this material enables it to act as a barrier layer to prevent reaction between PZT and SiO_2. Xu et al. utilized zirconia layers to passivate silicon wafers with thermal silicon oxides to deposit PZT films [4]. They reported good dielectric and ferroelectric properties using IDT electrodes on PZT films. The process flow for zirconia film deposition is shown in Figure 4.1.

4.1.1 Solution Preparation

Zirconia solution was prepared using 2–methoxyethanol (2–MOE) as the solvent. The precursor was zirconium n–propoxide ($Zr[O(CH_2)_2CH_3]_4$) (Aldrich Chemical Co., Milwaukee, WI). Initially, zirconium n-propoxide was added to 2–MOE in a rotary evaporator flask inside a glove box. The mixture was then reacted at 110°C for 2 hrs in a dry argon ambient. After reaction, the solution was distilled at 110 °C under vacuum to remove by–products. The preparation of the precursor solution was carried out in a Rotary Evaporator (Labconco, Kansas City, MU).

While stirring with a small magnet at room temperature, the solution was modified with 23 vol% acetic acid and 7 vol% acetylacetone (2,4– pentanedione). This improves the quality of the film and makes it possible to deposit particle–free, smooth and uniform films on 4–inch wafers. Acetic acid and acetylacetone are chelating agents; they reduce the tendency of the alkoxide compounds to hydrolyze during deposition [7]. However, solutions with this modification do not have a shelf life of more than one day. It seems that an esterification reaction between acetic acid and 2–MOE, liberating water, causes precursor precipitation [8]. For this reason the solution was modified just before being used. The final concentration of the zirconia solution was 0.4 M.

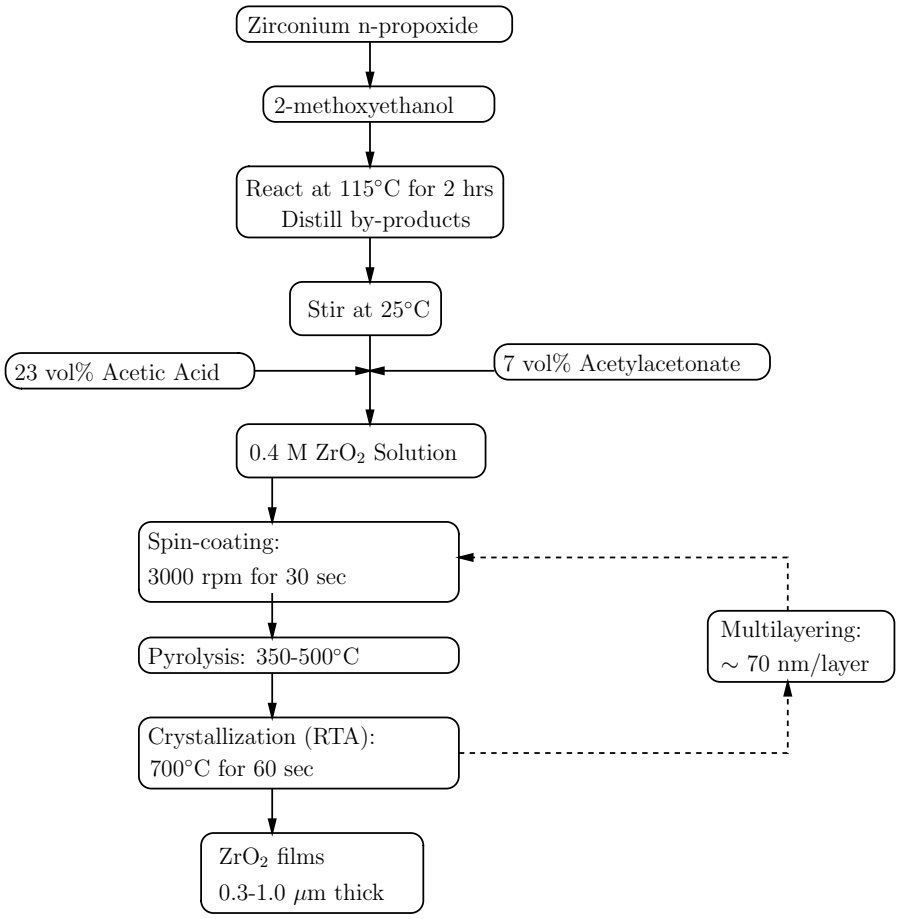

Figure 4.1. Sol–gel spin–on process flow for zirconia films.

4.1.2 Spin–Coating Process

Two kinds of wafers were used for zirconia film deposition. Platinized silicon wafers (1500 Å Pt/ 200 Å Ti/ 1 μm SiO_2/ Si, manufactured by Nova Electronic Materials, Inc.,Richardson, TX) were utilized to characterize the dielectric properties of zirconia films. The preferred orientation of the Pt film was (111). Thermally oxidized silicon wafers (5000 Å SiO_2/Si), which had similar structures as the diaphragm actuators and the micropumps were used to verify the compatibility of the process and to study the development of total stress in the films.

Wafers were preannealed at 700°C for 60 sec in a rapid thermal processing (RTP) unit (AG Associates, Sunnyvale, CA) just before depositing zirconia, to remove absorbed moisture. Often the first layer did not form a uniform coating on a 4–inch wafer if this step was omitted. Zirconia sol–gel solution was then applied on the wafers using a syringe with a 0.1 μm filter (Whatman Inc., Clifton, NJ). The wafers were spun at 3000 rpm for 30 sec using a photoresist spinner (HeadWay Research, Inc., Garland, TX) in a laminar flow hood. The spin-coated layer was pyrolyzed by a two–step process to remove organic compounds. The first pyrolysis step (60 sec) was conducted on a 1 mm–thick aluminum plate located on a hot plate with two steel bars as spacers ($\sim$3.5 mm gap). The temperature on the aluminum plate was $\sim$300°C. The second pyrolysis was performed on a hot plate at $\sim$450°C for 60 sec. Finally, the layer was crystallized by annealing in the RTP at 700°C for 60 sec. Each layer was $\sim$70 nm thick. To get the desired thickness, the spin coating and thermal processes were repeated. Finally, the zirconia layers were annealed in air in a furnace at 700 °C for 2 hrs.

4.2 PZT Film Preparation

PZT films were used as active layers in the diaphragm actuators and micropump structures. For these devices, a 1.5–2.0 μm thick PZT film on 4–inch wafers was required. The process flow for solution preparation and deposition of PZT film is shown in Figure 4.2.

4.2.1 Solution Preparation

The PZT solution was prepared using 2–MOE as solvent. Lead acetate trihydrate ($Pb(CH_3CO_2)_2{\cdot}3H_2O$), zirconium n–propoxide ($Zr[O(CH_2)_2CH_3]_4$), and titanium iso–propoxide ($Ti[OCH(CH_3)_2]_4$) (Aldrich Chemical Co., Milwaukee, WI) were used as precursors. Initially, lead acetate trihydrate was dissolved in 2–MOE in a rotary evaporator flask. It is known that 2–MOE dissolves carboxylate precursors like lead acetate by replacing one of the acetate groups with a methoxyethoxy group [7]. The remainder of the flask was filled with dry argon, and the flask was rotated at 120 rpm inside a silicon oil bath heated to 115°C. After the lead acetate trihydrate was completely dissolved, the solution was dehydrated under vacuum until a white powder was formed in the flask. At the same time, a mixture of zirconium n–propoxide and titanium iso–propoxide was prepared in the glove box. The more reactive titanium iso–propoxide was added into 2–MOE after the zirconium precursor. The mixture was stirred for 10 min at room temperature and added to the flask containing the dehydrated Pb–precursor. The total mixture was reacted for 3 hrs at 115°C under dry argon ambient. After reaction, the solution was distilled under vacuum to remove by–products until half of the solution remained. 22 vol% acetylacetone, 5 vol% acetic acid, and additional 2–MOE were added to modify the solution. The concentration of the solution was 0.75 M with 20 mol% excess lead content to compensate for high Pb loss during the film deposition.

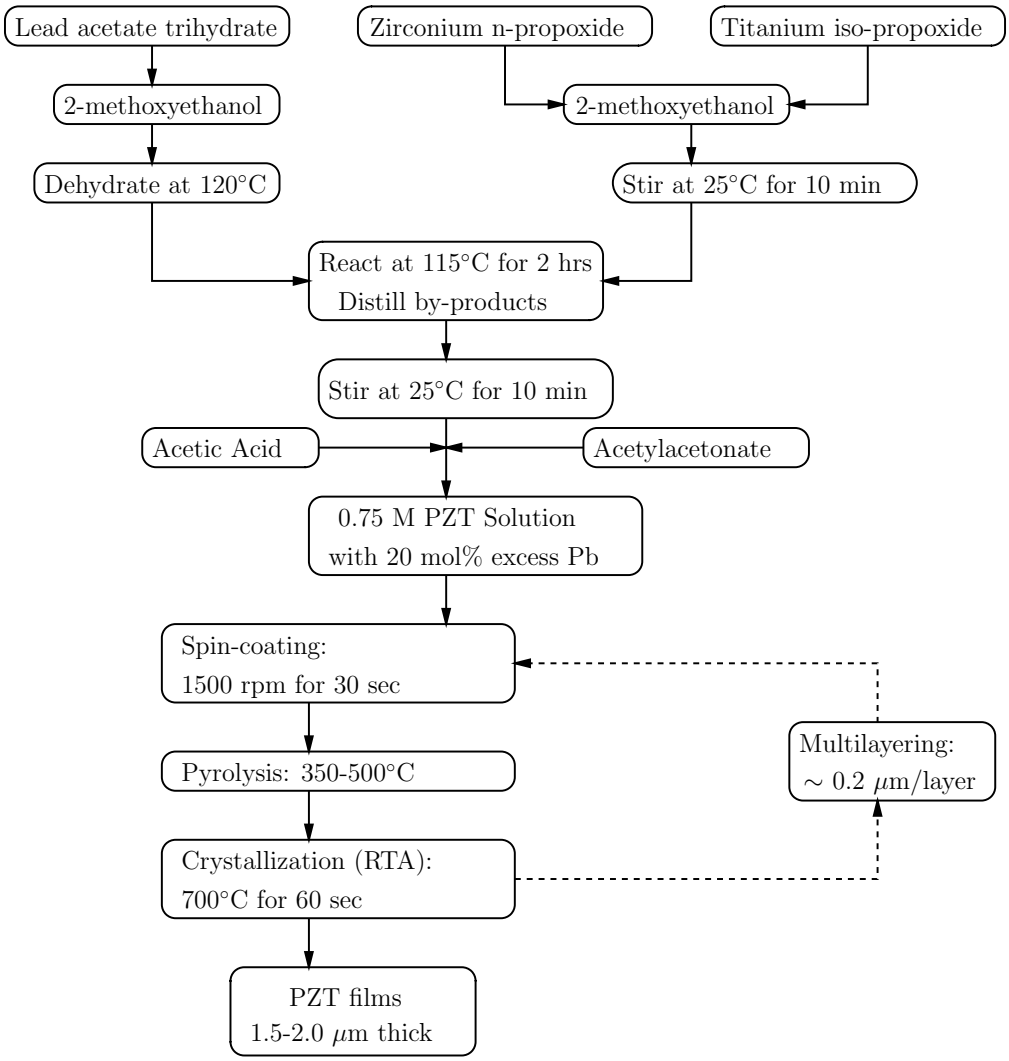

Figure 4.2. Sol–gel spin–on process flow for PZT films.

4.2.2 Spin–Coating Process

PZT (zirconium to titanium ratio of 52/48) films were deposited either on platinized silicon wafers or on zirconia passivated silicon wafers. (section 4.1.2). For PZT deposition, a lower spin–coating speed of 1500 rpm was used to obtain thicker

layers per each coating. To avoid cracking of the PZT films, the wafers were rotated during the pyrolysis process to create a uniform temperature profile across the 4–inch wafers. In addition, the edge bead on the substrate was removed by a cotton swab moistened with 2–MOE before the pyrolysis. During the spin–coating process, a thicker layer is formed at the edge of the wafer (edge bead) and the shrinkage of the thicker layer during the pyrolysis step frequently generates cracks in the PZT film. These cracks propagate from the edge to the center of the wafer [5]. Removal of the edge bead eliminated this problem.

4.3 Characterization of Zirconia and PZT Films

The microstructure and orientation of the zirconia and PZT films were studied using a scanning electron microscope (S–3500N, Hitachi, Inc.) and an x-ray diffractometer (XDS 2000, Scintag, Inc.). The zirconia layer and PZT film thickness were determined from SEM cross–sectional images or by a surface profiler (Alpha Step 500, Tencor, Inc.). To confirm the electrical properties of the films, dielectric constant and hysteresis loop measurements were carried out using a HP4192A LF impedance analyzer and an RT-66A Ferroelectric Test System (Radiant Technology, Inc.). The residual stress of the films were evaluated by a wafer curvature measurement (FLX–2320, Tencor, Inc).

4.3.1 Structural Characterization

It is difficult to deposit crack–free PZT films directly on silicon or silicon with thermally grown oxide by sol–gel spin–on procedures due to Pb-diffusion and formation of a lead silicate glass. To avoid this problem, zirconia layers can be used as buffer layers [4]. In this study, PZT films were deposited on zirconia passivated silicon wafers. It was found that the zirconia films needed to exceed > 0.2 μm in

thickness and had to be annealed at 700°C in air for more than 2 hrs to enable growth of crack free PZT films up to a thickness of 2.0 μm. Figure 4.3 shows cracking of PZT films deposited on SiO_2/Si and ZrO_2(70 nm)/ SiO_2/ Si wafers. The thicknesses of the PZT films were 0.2 μm. It was found that cracking of this type occurred whenever PZT films were deposited on 70 nm thick ZrO_2 films, independent of whether or not the ZrO_2 was pre–annealed at 700°C for 2 hrs. The x-ray diffraction patterns from the cracked films showed a broad peak (2Θ=30°) at the position for the pyrochlore phase. It is possible that a critical thickness and/ or

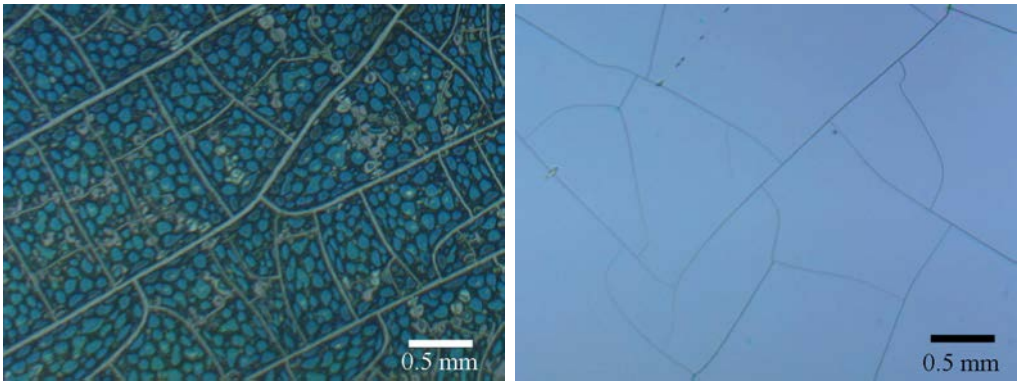

(a) (b)

Figure 4.3. Cracking of PZT films on (a) a SiO_2/ Si wafer and (b) a 70 nm thick ZrO_2/ SiO_2/ Si wafer.

density of the zirconia films is important to block Pb-diffusion from the PZT films to the SiO_2. Figures 4.4 shows x-ray patterns for zirconia and PZT films. The zirconia films were deposited on silicon wafers with 0.5 μm thick SiO_2. The x-ray pattern showed a weak tetragonal–phase peak, indicating poor crystallinity. After annealing at 700°C for 2 hrs, a monoclinic–phase developed. The PZT films on zirconia were randomly oriented. This is expected due to the poor crystallinity of the zirconia film and the lack of any template for oriented growth. The PZT films were pure pervoskite phase without any pyrochlore as observed by the x-ray patterns. The SEM micrograph of the cross section of the wafer (Figure 4.5) shows a sharp interface between the zirconia and PZT layers. There was no visible sign of reaction between SiO_2, ZrO_2 or PZT, indicating that zirconia acted as an effective buffer layer, as has been observed previously [4]. Both films exhibit columnar structures.

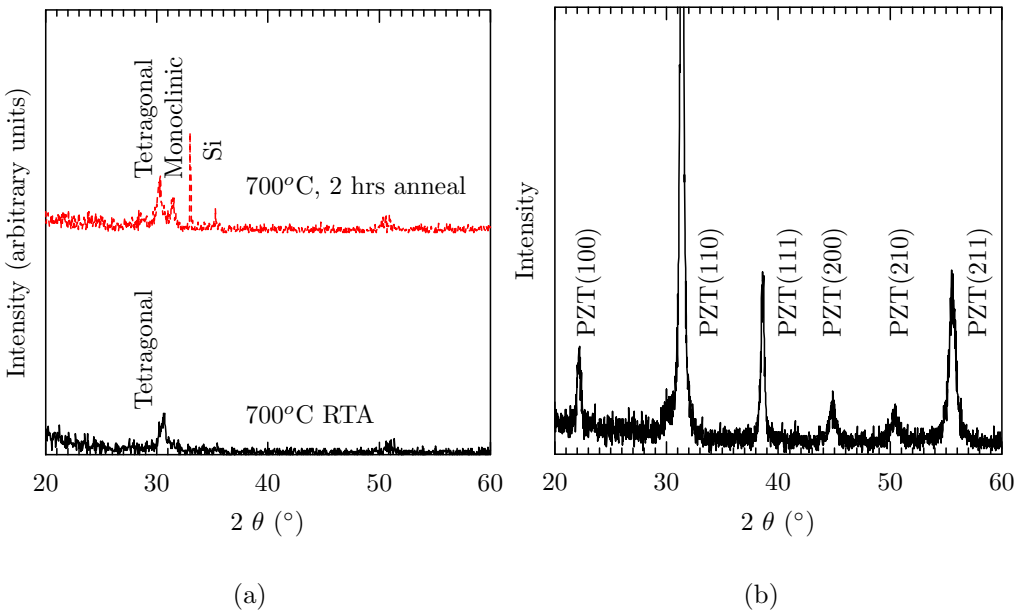

Figure 4.4. X-ray diffraction patterns of (a) zirconia film and (b) PZT film on ZrO_2.

In addition, the interface of each of the crystallized PZT layers is also visible. The thickness of the zirconia and PZT layers were ∼0.3 μm and ∼1.6 μm, respectively.

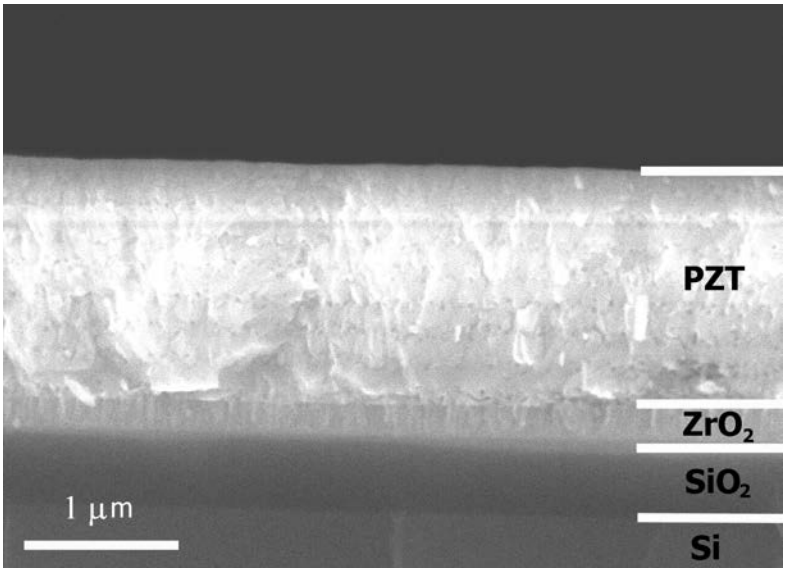

Figure 4.5. SEM micrograph of a wafer cross-section.

4.3.2 Uniformity of PZT Film Thickness

The thicknesses of the films will influence the electrical and the mechanical properties of the released diaphragm actuators and micropump structures. To check the thickness uniformity of a PZT film across a 4–inch wafer, a PZT film was deposited on a platinized silicon wafer and patterned by a two–step etch process using 10:1 buffered oxide etch (BOE= $10HN_4F$: 1HF) and hydrochloric acid [9]. The thickness of the film at several positions on the wafer was characterized by a surface profilometer. The horizontal points in Figure 4.6 were measured in a horizontal line parallel to the primary flat, passing through the center of the wafer. The vertical points were collected along a line perpendicular to the primary flat. The average thickness is 1.25 μm and the standard deviation is 0.031 μm. The film is $\sim$10% thicker in the middle than near the edge. Zirconia films are expected to be more uniform than PZT films since the zirconia layers are deposited with a more dilute solution at a higher spin speed.

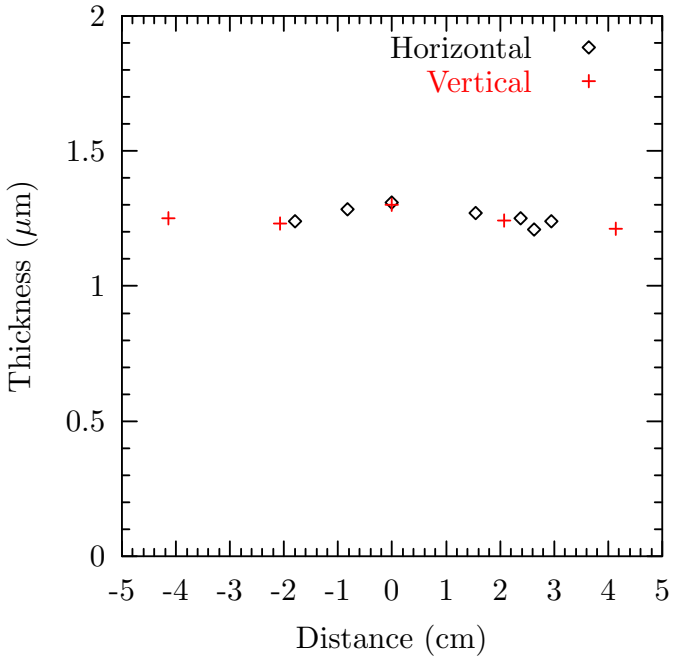

Figure 4.6. Uniformity of PZT film thickness across a 4–inch wafer.

4.3.3 Electrical Analysis

The dielectric and ferroelectric properties of ∼1.2 μm thick PZT films on platinized silicon wafers and ∼1.6 μm thick PZT films on zirconia passivated silicon wafers were characterized. For the electric measurements, Cr/Au or Pt electrodes were formed on top of the zirconia and PZT films. The diameters of planar top electrodes (for films on Pt–coated Si) were in the range of 1.0–1.5 mm. IDT electrodes were used for the PZT film on ZrO_2. The IDT electrodes were ring-shaped with 700 μm diameter. The IDT spacing and width were both 7.5 μm. The capacitances of the films were measured using a HP4192A in the 1 kHz to 1 MHz range with an oscillation voltage of 30 mV. The dielectric constant for the PZT films on Pt was ∼850 with a dielectric loss below 2% at 1 kHz. The polarization was ∼22μC/cm^2 with a coercive field of 61 kV/cm. For the PZT films on zirconia layers with IDT electrodes, the dielectric constant and polarization cannot be directly extracted from the capacitance and charge data due to the complex electric field distributions. The dielectric losses were maintained below 4% from 10 kHz to 1 MHz for the PZT films with the IDT electrodes. The dielectric constant and polarization will be discussed in Chapter 5 with the help of a finite element analysis. Both PZT films show good ferroelectric properties as seen in Figure 4.7. The dielectric constant of a 0.3 μm thick zirconia film was about 20, with dielectric losses of 4% at 1 kHz.

4.3.4 Residual Stress Analysis

In micromachined devices, residual stress strongly affects the mechanical behavior of the structures. For example, a stress distribution across the thickness of a micromachined cantilever makes the structure curl. To prevent this problem, the stress of each layer should be balanced [10]. In addition, the deflection of micromachined silicon nitride diaphragms due to a pressure differential decreases with an increase in tensile stress in the diaphragm [11]. Such stresses will also affect the magnitude of the piezoelectrically–induced deformation of the diaphragm.

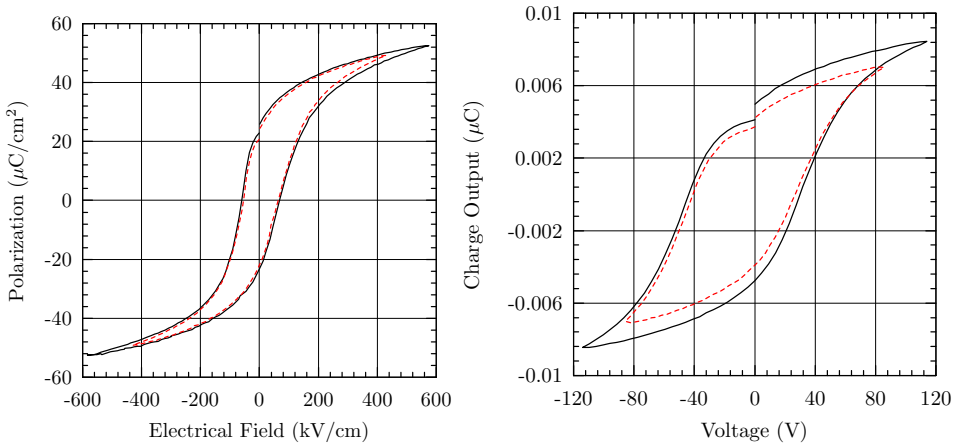

Figure 4.7. Ferroelectric hysteresis loops of PZT films on (a) platinized wafers and (b) zirconia passivated wafers.

At the wafer–level, the residual stress of a film on a substrate can be evaluated by Stoney's equation [12]:

$$\sigma = \frac{1}{(\rho_2 - \rho_1)} \left[\frac{E}{1-\nu}\right] \frac{T^2}{6t} \tag{4.1}$$

where σ is the film stress, and ρ_1 and ρ_2 are the initial curvature and the curvature after the film deposition on the substrate, respectively, *E/(1-ν)* is the biaxial elastic modulus of the substrate, T is the thickness of the substrate, and t is the film thickness. This equation is useful because the film stress can be estimated without any mechanical information for the film. The only parameter required for the film is the thickness.

Using Equation 4.1, the residual stress of the stack (1.6 μm PZT/ 0.3 μm ZrO_2/ 0.5 μm SiO_2) shown in Figure 4.8 was evaluated. The substrates used were 4–inch silicon wafers with 0.5 μm thick thermal oxide on both sides. The thicknesses of the wafers were 510–570 μm. Initially, the curvatures were measured using a Tencor FLX–2320 thin film stress measurement system. This system scans a wafer using a laser of wavelength of either 670 nm or 750 nm, resulting in detection of the

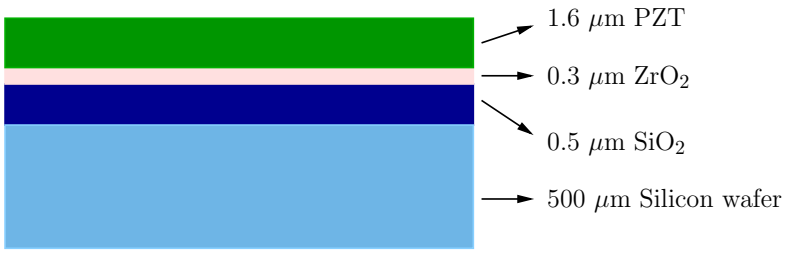

Figure 4.8. Multilayer stack on wafer for stress measurement.

curvature. This experiment used two scan lines passing through the center of the wafers. One line was parallel to the primary flat of a wafer and the other line was perpendicular to the flat. The thermal silicon oxide on the back side of the wafers was stripped using BOE, with the front side of the wafer covered with photoresist. The curvature of the wafers was then measured to calculate the residual stress of the thermal oxide. The curvature was subsequently measured after deposition of each of the films. The time delay between the deposition and the measurement was usually about 30 min. Figure 4.9 shows the results.

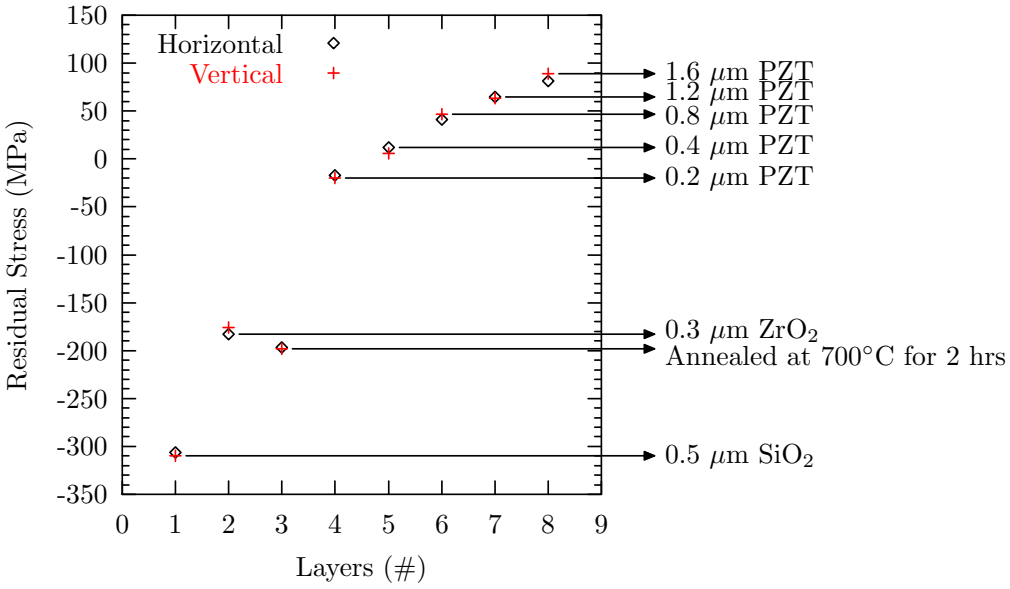

Figure 4.9. Residual stress of mutilayer films on 4–inch SiO_2/ Si wafers.

The stress of the initial thermal oxide layer was compressive (-300 to -310 MPa). Deposition of 0.3 μm zirconia film increases the total stress to -180 MPa. Annealing the wafer at 700°C for 2 hrs results in a total stress of -200 MPa. The first layer

of PZT increased the total stress to 0 MPa. The total stress of the stack (1.6 μm PZT/ 0.3 μm ZrO_2/ 0.5 μm SiO_2) was 80 MPa. With PZT deposition, the total stress saturates at around 100 MPa. To verify the effect of annealing on the thermal oxide, the experiment was repeated with an additional annealing step as shown in Figure 4.10.

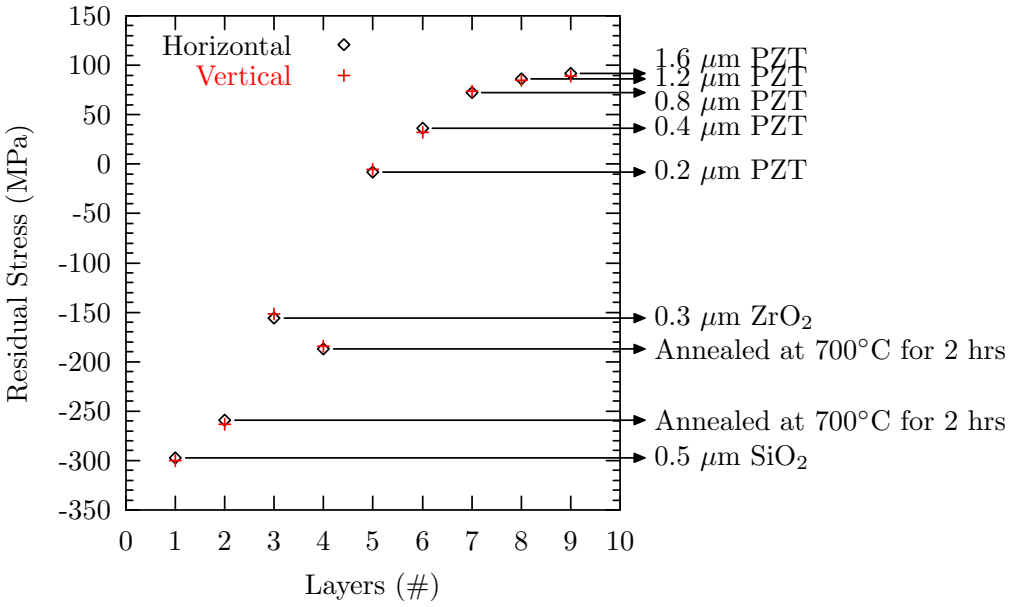

Figure 4.10. Residual stress of mutilayer films on 4–inch SiO_2/ Si wafers with an additional annealing.

An additional annealing step at 700°C for 2 hrs reduced the stress of the thermal oxide by 13%. The final stress of the stack was ∼90 MPa. Thus, by using an additional annealing step for the thermal oxide, the final stress of the stack can be controlled. However, this complicates interpretation of the stress in the PZT and ZrO_2 layers because there may be simultaneous stress changes in the SiO_2 during the heat treatment steps following sol–gel deposition.

To eliminate the effect of stress changes due to the thermal oxide, the same film stacks were produced directly on Si wafers. Figure 4.11 shows the evolution of residual stress with film thickness. The stress of the as-deposited zirconia film was ∼80 MPa and the annealing process drops the stress to -40 MPa. The deposition of the first PZT layer increased the total stress to 210 MPa. With the deposition

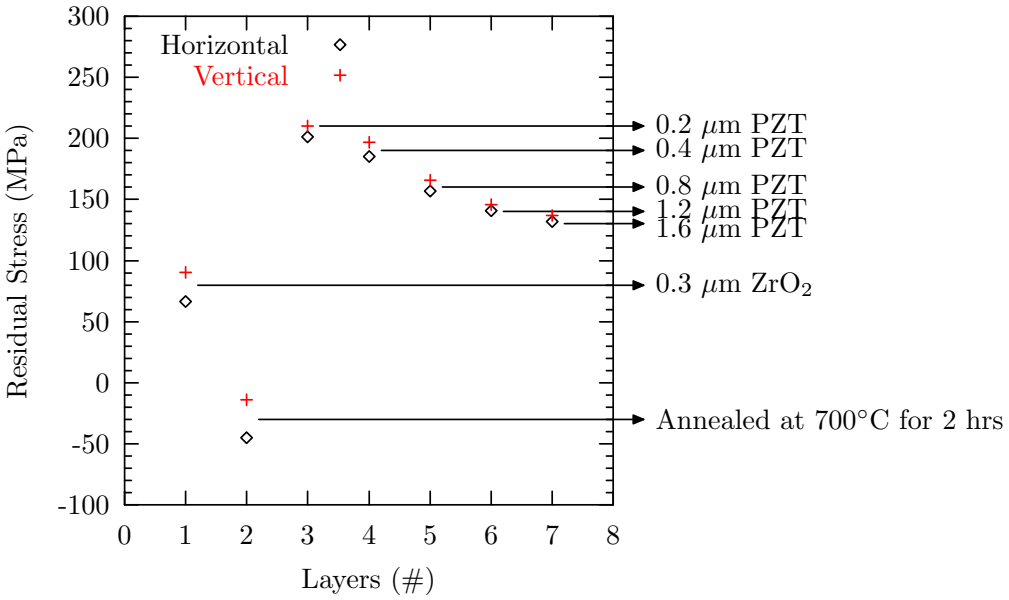

Figure 4.11. Residual stress of mutilayer films on 4–inch Si wafers.

of PZT layers, the total stress approaches 100 MPa. From the total stress, the stress of each layer can be calculated by Equation 4.2.

$$\sigma_t t_t = \sum_{i=1}^{n} \sigma_i t_i \tag{4.2}$$

where σ_t and t_t are the total stress and thickness of the stack and σ_i and t_i are the stress and thickness of each layer. n is the number of the layers. Figure 4.12 shows the calculated stress of each individual layer.

The residual stress mainly comes from the mismatch in thermal expansion coefficients between the films and the substrates [13]. This stress due to thermal expansion mismatch can be expressed by the following equation:

$$\sigma = \frac{E_f}{(1-\nu_f)}(\alpha_f - \alpha_s)\Delta T \tag{4.3}$$

where E_f and ν_f are the Young's modulus and Poisson's ratio of the film, α_f and α_s are thermal expansion coefficients of the film and the substrate and ΔT

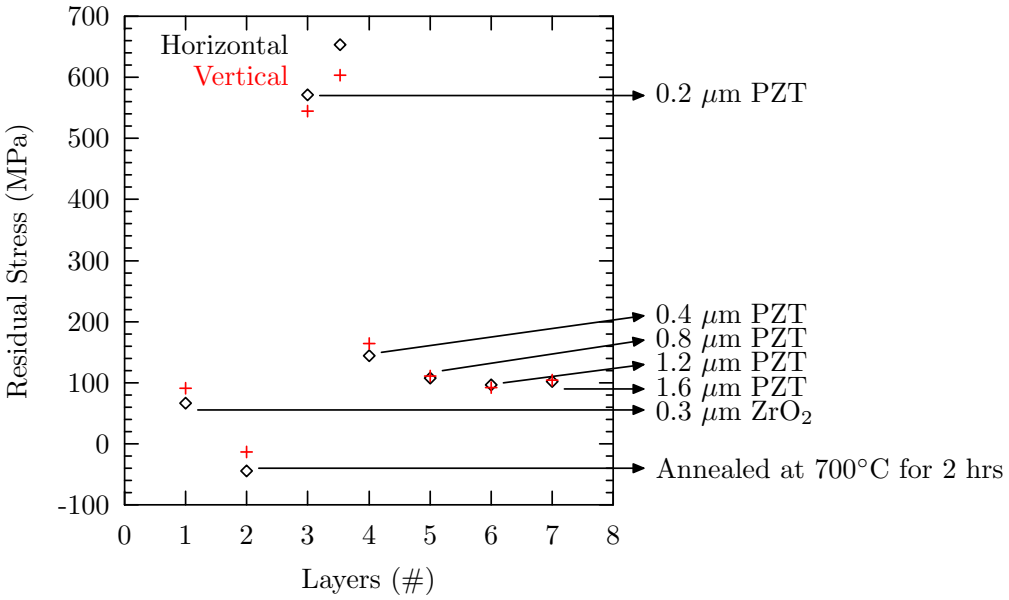

Figure 4.12. Apparent residual stress of multilayer films on 4–inch silicon wafers with an additional annealing.

is the temperature difference between the deposition temperature (700°C) and room temperature. The calculated stresses of the films are summarized in Table 4.1 [5]. From Figure 4.12, the stress for each PZT film (about 0.4 to 1.6 μm thick)

Table 4.1. The calculated residual stress from thermal mismatch.

Materials	α_{TCE}	Young's Modulus (GPa)	Poisson's ratio	Stress (MPa)
Si	2.6	150	0.17	–
PZT	2.0–6.7[1]	70–100	0.3	100–144
ZrO_2[2]	8.4	160–205	0.27	835–1000

[1] $\alpha_{TCE,ferroelectric}$ = 2.0 ppm/°C and $\alpha_{TCE,paraelectric}$ = 6.7 ppm/°C.
[2] fully stabilized zirconia.

in Table 4.1. However, the apparent stresses of the zirconia and the first PZT layer are significantly different from what is expected. Changes in the stress of the zirconia film is thought to explain this. Zirconia films on either Si or SiO_2/ Si wafers exhibited stresses of 20–100 MPa after the deposition. After an annealing process at 700°C for 2 hrs, the stresses of the zirconia films became more compressive (to -40 MPa). This stress change can be explained by the phase transformation between the tetragonal phase and the monoclinic phase of the zirconia films. As shown in Figure 4.4, the annealing step developed the monoclinic phase, which

generates a volume expansion of ∼4% [6]. The films also showed aging of stress with time as seen in Figure 4.13. Stress relaxation in films can be explained by either structural changes or adsorption of moisture into the film through the grain boundaries [14]. For structural relaxation, as the stress itself is the driving force, a change in the sign of the stress will not occur. There is no driving force at zero stress. Thus, in zirconia films, where stress changes with time from tensile to compressive, adorption of moisture in air is a reasonable mechanism for the stress change. Water molecules absorbed into the pores leads to compressive stress in the film [14]. As another mechanism, when ZrO_2 reacts with moisture and hydrates, repulsion between the OH dipoles can induces a compressive stress component in the films [15].

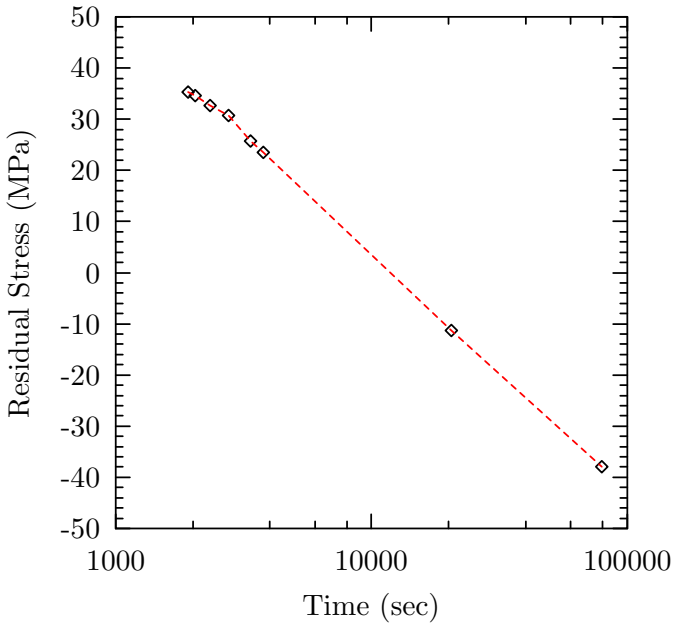

Figure 4.13. Residual stress of zirconia film as a function of time.

Due to the stress aging of zirconia films, it is not easy to estimate the actual stress of a zirconia layer in either PZT/ ZrO_2/ Si or PZT/ ZrO_2/ SiO_2/ Si stacks. It is expected that aging of buried zirconia films will be negligible because the PZT layer blocks direct contact with moisture. As an approximation, the stress of the zirconia film was calculated assuming the stress of the first PZT layer (in Figure 4.11) to be in the range of 100 to 150 MPa. The calculated stress of the zirconia film was 230–270 MPa. In addition, the best linear fit to the data in

Figure 4.13 yields an initial stress value of ∼188 MPa. These values are much smaller than those calculated in Table 4.1. However, this stress value would be reasonable considering that the structure of the zirconia film (in Figure 4.4) is partially amorphous. Subtracting the total stresses of a PZT/ ZrO_2/ Si stack (in Figure 4.11) from that of a PZT/ ZrO_2/ SiO_2/ Si stack (in Figure 4.9), the stress of the thermal oxide is calculated to -145 MPa after the final film deposition. The stresses of the films are summarized in Table 4.2.

Table 4.2. The expected residual stress of the films.

Film	Initial stress (MPa)[1]	Final stress (MPa)[2]
SiO_2	-300	-147
PZT		100–150
ZrO_2	-40 – 100 MPa	230–270[3]

[1] stress before the PZT film deposition
[2] stress after the PZT film deposition
[3] calculated stress assuming stress of the first PZT layer is 100–150 MPa.

4.4 Conclusions

1.6–2.0 μm PZT and zirconia films were prepared on 4–inch oxidized silicon wafers by sol–gel processes. Both solutions used 2–MOE as solvent. The zirconia acted as a buffer layer to prevent the reaction between the PZT and SiO_2. It was found that the zirconia films should be thicker than 0.2 μm and needs to be annealed at 700°C for more than 2 hrs to deposit crack–free PZT films. The cross-section of the wafer shows sharp interfaces between the layers, indicating no significant reaction. The PZT films on the zirconia films showed good dielectric and ferroelectric properties. PZT films deposited by the sol–gel method showed good uniformity (less than ±3% variation across a 4–inch wafer). The average residual stress in a 1.6 μm PZT/ 0.3 μm ZrO_2/ 0.5 μm SiO_2 stack was ∼80 MPa.

References

[1] T. Yoshimura and S. Trolier-McKinstry, "Growth and Piezoelectric Properties of $Pb(Yb_{1/2}Nb_{1/2})O_3$–$PbTiO_3$ Epitaxial Films," *J. Appl. Phys.*, vol. 92, no. 7, pp. 3979–3984, 2002.

[2] E. Hong, J.C. Shin, J. Choi, C.S. Hwang, and H.J. Kim, "Preparation and Characterization of $Pb(Zr,Ti)O_3$ Thin Films by Metalorganic Chemical Vapor Deposition Using a Solid Delivery System," *J. Mater. Res.*, vol. 15, no. 6, pp. 1284–1290, 2000.

[3] I. Kanno, H. Kotera, K. Wasa, T. Matsunaga, T. Kamada, and R. Takayama, "Crystallographic Characterization of Epitaxial $Pb(Zr,Ti)O_3$ Films with Different Zr/Ti Ratio Grown by Radio–Frequency–Magnetron Sputtering," *J. Appl. Phys.*, vol. 93, no. 7, pp. 4091–4096, 2003.

[4] B. Xu, Y. Ye, L.E. Cross, J.J. Bernstein, and R. Miller, "Dielectric Hysteresis from Transverse Electric Fields in Lead Zirconate Titanate Thin Films," *Appl. Phys. Lett.*, vol. 74, no. 23, pp. 3549 – 3551, 1999.

[5] R. Wolf, "Temperature Dependence of the Piezoelectric Response of Lead Zirconate Titanate Films for MEMS Applications," Master's thesis, The Pennsylvania State University, 2001.

[6] R.H.J. Hannink, P.M. Kelly, and B.C. Muddle, "Transformation Toughening in Zirconia–Containing Ceramics," *J. Am. Ceram. Soc.*, vol. 83, no. 3, pp. 461–487, 2000.

[7] R. Schwartz, "Chemical Solution Deposition of Perovskite Thin Films," *Chem. Mater.*, vol. 9, no. 11, pp. 2325–2340, 1997.

[8] D.P. Birnie, "Esterification Kinetics in Titanium Isopropoxide–Acetic Acid Solutions," *J. Mater. Sci.*, vol. 35, pp. 367–374, 2000.

[9] L.-P. Wang, "Microelectromechanical Systems (MEMS) Sensors Based on Lead Zirconate Titanate (PZT) Films," PhD thesis, The Pennsylvania State University, 2001.

[10] S.S. Lee and R.M. White, "Piezoelectric Cantilever Acoustic Transducer," *J. Micromech. Microeng.*, vol. 8, pp. 230–238, 1998.

[11] W.P.B. Eaton, J.H. Smith, and D.W. Plummer, "A New Analytical Solution for Diaphragm Deflection and Its Application to a Surface–Micromachined Pressure Sensor," *in Proceedings of International Conference on Modeling and Simulation of Microsystems*, pp. 640–643, 1999.

[12] G. Stoney, "The Tension of Metallic Films Deposited by Electrolysis," *in Proceedings of the Royal Society of London*, vol. A82, pp. 172–175, 1909.

[13] B.A. Tuttle, J.A. Voigt, T.J. Garino, D.C. Goodnow, R.W. Schwartz, D.L. Lamppa, T.J. Headly, and M.O. Eatough, "Chemically Prepared Pb(Zr,Ti)O_3 Thin Films: The Effects of Orientation and Stress," *in Proceedings of the 8^{th} International Symposium on Applications of Ferroelectrics*, pp. 344–348, 1992.

[14] G. Atanassov, J. Turlo, J.K Fu, and Y. S. Bai, "Mechanical, Optical and Structural Properties of TiO_2 and MgF_2 Thin Films Deposited by Plasma Ion Assisted Deposition," *Thin Solid Films*, vol. 342, pp. 83–92, 1999.

[15] R. Brenier and A. Gagnaire, "Densification and Aging of ZrO_2 Films Prepared by Sol-Gel," *Thin Solid Films*, vol. 392, pp. 142–148, 2001.

Chapter 5

Micromachined Diaphragm Actuators

This chapter discusses the fabrication and characterization of diaphragm actuators. The purpose is to verify the concept of diaphragm actuators driven with ring–shaped IDT electrodes to generate large deflection (up to several micrometers at the center) as presented in Chapter 3. The structure is a diaphragm–type unimorph consisting of a passive and an active layer. Ring–shaped IDT electrodes formed on top of the active layer are used to actuate the diaphragms. The diaphragm actuators were released by deep reactive ion etching (DRIE). Four aspects of the diaphragm actuators were characterized: structural properties, electrical properties, resonance characteristics and electrically–induced deflection. Finite element analysis was utilized as a supplementary tool to explain the observed results. Characterization of these actuators enabled improvements in the design of the actuators used in micropumps.

5.1 Design of Diaphragm Actuators

Diaphragm actuators were designed to be fabricated by bulk micromachining using DRIE. The diaphragm actuators were prepared by depositing multiple thin film layers on the silicon wafer and removing the silicon under the diaphragm from the back of the wafers using DRIE. Figure 5.1 shows a schematic view of a diaphragm actuator. The diaphragm is a circular unimorph with ring–shaped IDT electrodes. Thermally grown silicon oxide (SiO_2) and sol-gel PZT layers were used as the passive and active layers in the unimorph structure, respectively. As discussed in Chapter 3, ring–shaped IDT electrodes are expected to produce larger deflections (larger than the diaphragm thickness). In addition, this electrode configuration yields expansion in the radial direction of the piezoelectric layer along with contraction in the tangential direction, resulting in downward deflection. Large downward deflection is essential for the micromachined pumps discussed in Chapter 3.

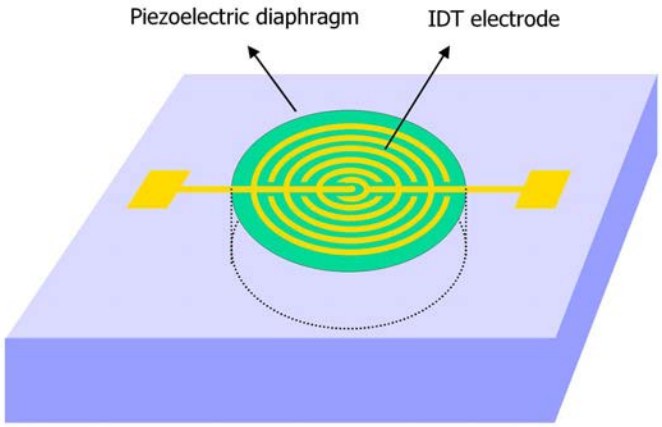

Figure 5.1. Schematic diagram of a diaphgram actuator.

To investigate the effect of actuator geometry on the achievable deflection, diaphragm structures which had different IDT diameters and spacings were designed. The diameters of the ring–shaped IDT electrodes were 500, 600, and 700 μm. The spacings of IDT electrodes were 7.5, 10, and 12.5 μm. The IDT width was commonly 7.5 μm. The ratio of IDT diameter to diaphragm diameter was $\sim$0.8. This ratio was chosen based on finite element analysis (using plate theory) of

d_{31}–mode diaphragm actuators to generate the largest deflection in the same size diaphragm [1] [1]. In addition, some diaphragm structures had parallel IDT structures or solid circular electrodes with various diameters from 500 to 1400 μm as test structures. The parallel IDT electrodes covered circular diaphragms. The IDT width was 7.5 μm and the spacings of the IDT were 7.5, 10, and 12.5 μm.

5.2 Fabrication

Diaphragm actuators were fabricated by a two mask process. Four–inch diameter (100) silicon wafers with ∼0.5 μm thermally grown silicon oxide (SiO_2) were used as substrates. The oxide layer acts as the passive layer in the unimorph structure. Figure 5.2 illustrates the fabrication process. First, zirconia and PZT layers were sequentially deposited on the wafers by the sol-gel methods described in Chapter 4. The thicknesses of the zirconia and PZT layers were ∼0.3 and ∼1.6 μm, respectively. The zirconia film acts as a buffer/barrier layer and enables deposition of crack–free PZT films (see Section 4.3.1). The ZrO_2 layer was annealed at 700°C for 2 hrs in a furnace before PZT was deposited on it. A Cr/Au (150 Å/ 1200 Å) layer was then deposited on top of the PZT film by thermal evaporation (Kurt Lesker E-gun/ thermal evaporator). Evaporation was carried out after the chamber base pressure of less than 10^{-6} Torr was reached. The deposition rates of Cr and Au were ∼0.8 Å/second and ∼2.0 Å/second, respectively. The Cr layer improves the adhesion between Au and PZT. The metal layer was then patterned using standard photolithography with Shipley 1813 photoresist (Shipley, Inc., Marlborough, MA) and wet etch processes as summarized in Table 5.1. Figure 5.3 shows IDT electrodes with three different spacings. Diaphragm patterns were then transferred to the back side of the wafers by an aligner with a bottom–side–alignment microscope (MA-6 mask aligner, Suss MicroTech, Munich, Germany). Finally, the diaphragm structures were released by DRIE (Bosch process [2]). This process

[1] It was subsequently determined that this ratio did not give the largest deflection for diaphragm actuators with ring–shaped IDT electrodes. This will be discussed further in section 5.6.

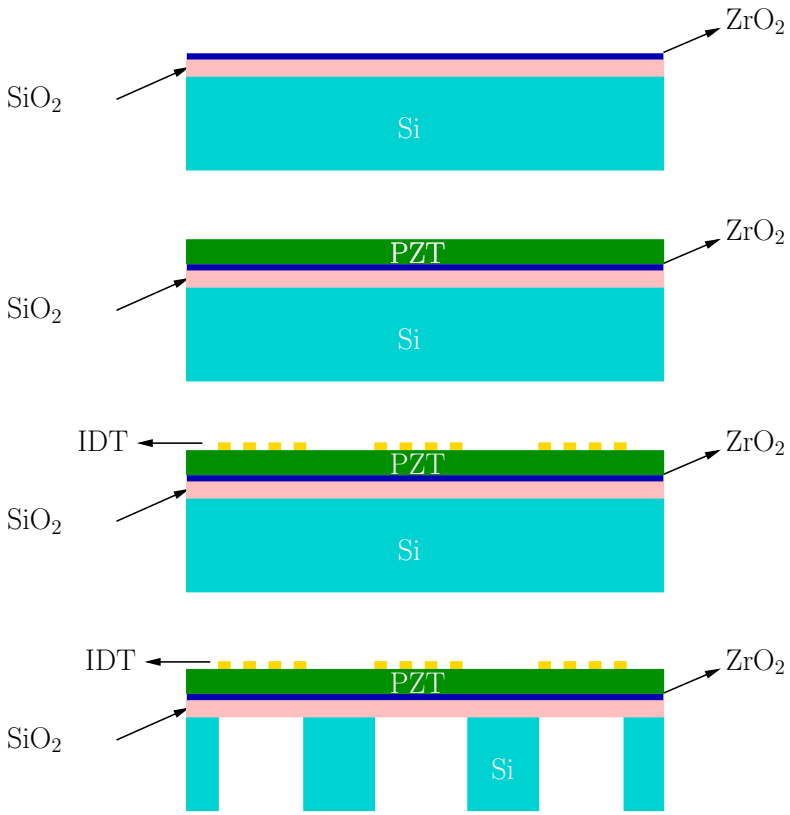

Figure 5.2. Process flow of a diaphragm actuator.

consists of alternating polymerization and silicon etch processes. In the polymerization step, the horizontal surfaces and sidewalls are coated with a thin polymer. In the subsequent step, the polymer at the bottom of the trench is removed due to ion bombardment, exposing silicon that is selectively etched. This enables etching features with high aspect ratio. This DRIE process was conducted by a STS (Surface Technology Systems, South Wales, United Kingdom) DRIE system. The etching of silicon was performed at 15-35 mTorr with a coil power of 1000-3000 Watts using SF_6 gas (200-600 sccm). The power for the passivation process was 500-2000 Watts using C_4F_8 (50-115 sccm). The wafer was clamped electrostatically and the backside was cooled by helium gas.

Table 5.1. Photolithography and etching processes for IDT electrode patterning.

Photolithography process – Shipley 1813 photo resist	
dehydration	5 min on a hot plate at 115^{o}C
HMDS[1]	3000 rpm for 40 sec
spin speed for resist	3000 rpm for 40 sec
soft bake	90 sec on a hot plate at 115^{o}C
exposure	3.5 sec using 12 mW (g-line)
develop	1∼2 min, MF312[2]/DI[3] = 1:1
hardbake	5 min on a hot plate at 115^{o}C
Cr/Au etching process	
Au etching	45 sec, gold etchant[4]
Cr etching	10 sec, chrome etchant[5]

[1] Hexamethyldisilazane: adhesion promoter
[2] Shipley developer
[3] Deionized water
[4] 42% KI: 3% I: 55% H_2O (Transene Inc., Danvers MA)
[5] 6% HNO_3: 16% $(NH_4)_2Ce(NO_3)_6$: 78% H_2O (Transene Inc., Danvers MA)

(a) (b) (c)

Figure 5.3. Ring–shaped IDT electrodes of three different spacings of (a) 7.5, (b) 10, and (c) 12.5 μm.

5.3 Structural Characterization

The zirconia and PZT layers in the diaphragm structures exhibited the same characteristics discussed in Chapter 4. PZT films on ZrO_2 were randomly oriented and had pure perovskite phase without any detectable pyrochlore. A SEM micrograph of the cross section of the wafer showed sharp interfaces between SiO_2, ZrO_2 and PZT. Figure 5.4 shows a released diaphragm actuator. As shown in the figure, the circular boundary of the diaphragm actuator is well defined by the DRIE pro-

cess. However, the diameters of diaphragm actuators were enlarged by around 10% since the DRIE process was not optimized. These diameters were measured using a calibrated optical microscope.

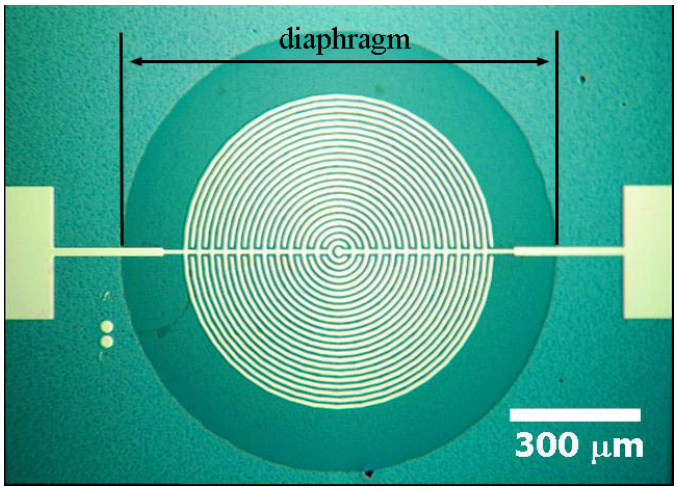

Figure 5.4. Released diaphragm actuator.

5.4 Electrical Characterization of Ferroelectric Layers

The dielectric and ferroelectric properties of the PZT layers in released diaphragm actuators were measured to verify that the fabrication process did not degrade their characteristics. This is important as the PZT properties directly influence the performance of diaphragm actuators. In addition, ring-shaped IDT electrode structures are interesting due to use of the in–plane dielectric (or ferroelectric) properties of the PZT layers, rather than the out–of–plane properties.

5.4.1 Measurement Set–up

Dielectric Measurement The capacitance and dielectric loss of PZT films were measured using a HP4192A LF impedance analyzer (Hewlett–Packard, Palo Alto, CA). All measurement were conducted at a frequency of 10 kHz and oscillation voltage of 30 mV, unless otherwise mentioned.

Ferroelectric Measurement The charge–voltage hysteresis loops of PZT films were measured with a RT66A standardized ferroelectric test system (Radiant Technologies, Albuquerque, NM). To apply high voltages up to 200 V, a voltage amplifier (790 Series, Power Amplifier, PCB Piezotronics, Inc., Depew, NY) was connected to the RT66A.

5.4.2 Dielectric Characterization

The measured capacitances and dielectric losses of PZT films in diaphragm actuators are shown in Figure 5.5 as a function of frequency. The capacitances were in the range of 5–30 pF depending on the IDT diameter and spacing. There was little change in these values when compared to those measured before diaphragm actuators were released. The measured capacitances were proportional to the IDT diameters and inversely proportional to the IDT spacing. The capacitances were decreased by 4% from 10 kHz to 1 MHz. The dielectric losses were 0.015 at 10 kHz and in all cases were maintained below 0.025 through this frequency range.

The relative dielectric permittivity is a parameter commonly used to compare dielectric materials. In a dielectric material with two parallel top and bottom electrodes, its dielectric constant is calculated by Equation 5.1 [3].

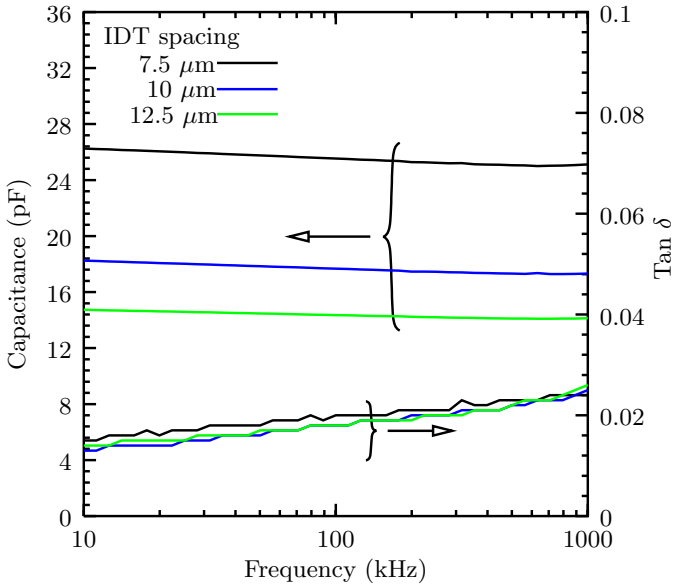

Figure 5.5. Capacitance and dielectric loss of 700 μm IDT–diameter diaphragms with three different IDT spacings.

$$\epsilon_r = \frac{Cd}{A\epsilon_0} \tag{5.1}$$

where C is the capacitance, d is the distance between top and bottom electrodes, A is the area of those electrodes, ϵ_r and ϵ_0 are the relative dielectric constant and permittivity in vacuum, respectively. In Equation 5.1, an underlying assumption is of uniform electric fields formed inside the dielectric material between the electrodes. However, this assumption is not valid for a capacitor with IDT electrodes due to the complex electric field formed inside the structure. Xu et al. tried to use Equation 5.1 with two modifications to calculate the relative dielectric constant [4]. They used the product of the thickness of the PZT film and the length of the IDT electrode as the capacitance area, and the center–to–center distance between the two IDT electrodes as the distance between the two electrodes. The calculated dielectric constants were specified to range from 1044–1890. This shows the limitation of Equation 5.1 to calculate relative dielectric permittivity of a capacitor with IDT electrodes. In addition, it is difficult to consider the effect of other layers (such as the ZrO_2 under the PZT films) in this equation. To obtain a

more realistic estimate, finite element analysis was conducted in this work using a commercial finite element analysis package (ANSYS, Inc., Connonsburg, PA).

Finite Element Analysis A simple 2–dimensional model, shown in Figure 5.6, was used to obtain the voltage drop, electric field distribution and the capacitance of a structure with IDT electrodes. In the model, the dielectric stack was assumed to be composed of SiO_2, ZrO_2 and PZT layers. In addition, 10 μm thick air layers above and below the structure were added to simulate a completely released diaphragm. Since the electrode is part of two capacitors on either side of it, only half of the width of the electrode was included in the model.

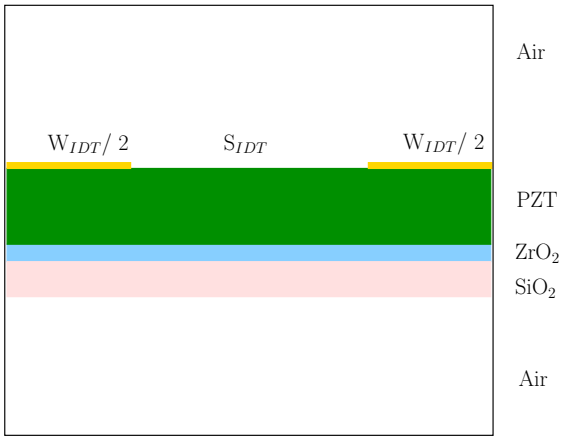

Figure 5.6. Model for a capacitor with IDT electrodes.

This model was meshed using Plane121 elements, which are 2 dimensional, 8 node electrostatic elements [5]. The number of meshes was increased until the result converged to a value within 1% deviation. The size of the resulting mesh was 0.2 μm. Material properties and parameters which were used in the model are summarized in Table 5.2.

The voltage drop and electric field of the model structure were simulated as shown in Figure 5.7. In these figures, it is clear that the voltage drop mainly occurs between the IDT electrodes, rather than under the IDT electrodes. In Figure 5.7 (a), the lines represent equipotential lines. For this reason, the electric field

Table 5.2. Material properties and parameters used in the capacitor model (Figure 5.6).

Material	Relative dielectric constant	Thickness (μm)
PZT	850	1.6
ZrO_2	20[1]	0.3
SiO_2	4	0.5
Air	1	10

[1] This value was measured in Chapter 4.

between the IDT electrodes is relatively uniform and parallel to the layers. The electric field under the IDT electrodes is weaker by a factor of 10 than that between the IDT electrodes and perpendicular to the layers. The electric field component ratios parallel: perpendicular to the PZT layers were around 1800 between IDT electrodes (at point A in Figure 5.7 (b)) and 2 under the IDT electrodes (at B point in Figure 5.7 (b)). A strong electric field is formed at the corners of the IDT electrodes.

The electric field and dielectric displacement distribution in a multilayer dielectric structure (see Figure 5.8) can be explained by the following two equations [6]:

$$E_{t1} - E_{t2} = 0 \tag{5.2}$$

$$D_{n1} - D_{n2} = \rho_s \tag{5.3}$$

where E_{t1} and E_{t2} are the tangential components of the electric field on either side of an interface and D_{n1}, D_{n2} are the normal components of the electric flux density on either side of the interface and ρ_s is the surface charge density. When there is no surface charge at the interface, Equation 5.3 can be rewritten as:

$$\epsilon_1 E_{n1} = \epsilon_2 E_{n2} \tag{5.4}$$

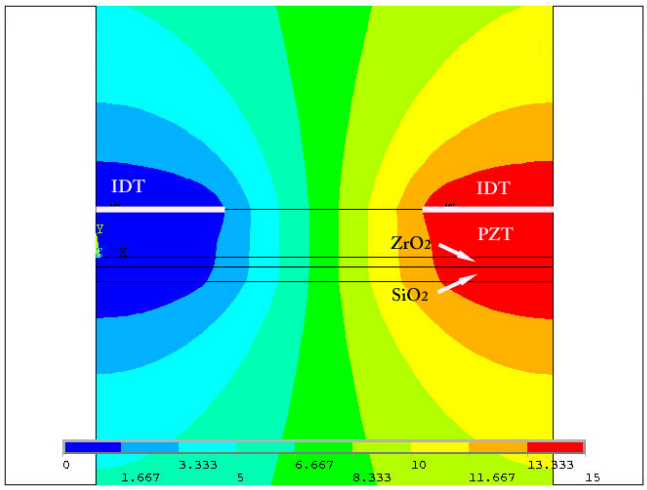

(a)

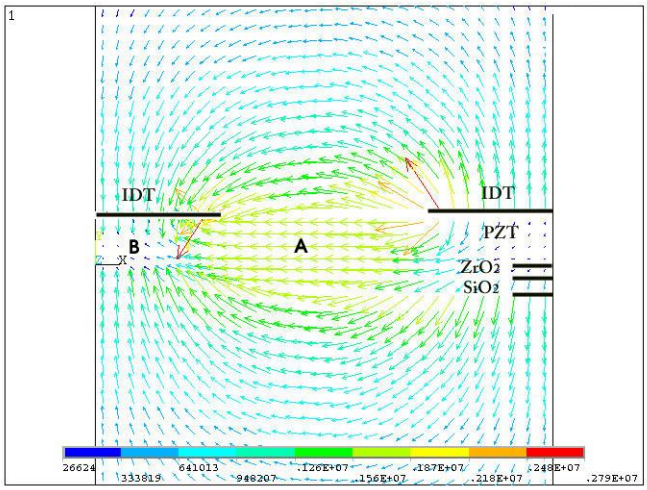

(b)

Figure 5.7. (a) Voltage drop and (b) electric field distribution between IDT electrode with a width and spacing of 7.5 μm when 15 V is applied. Scales given in V and V/m, respectively.

From Equation 5.2 and Equation 5.4, it is clear that the electric field is confined to the high dielectric constant material when it passes from a low permittivity to a high dielectric permittivity. The normal component of the electric field is reduced by the ratio of the dielectric constants of the two materials while the tangential

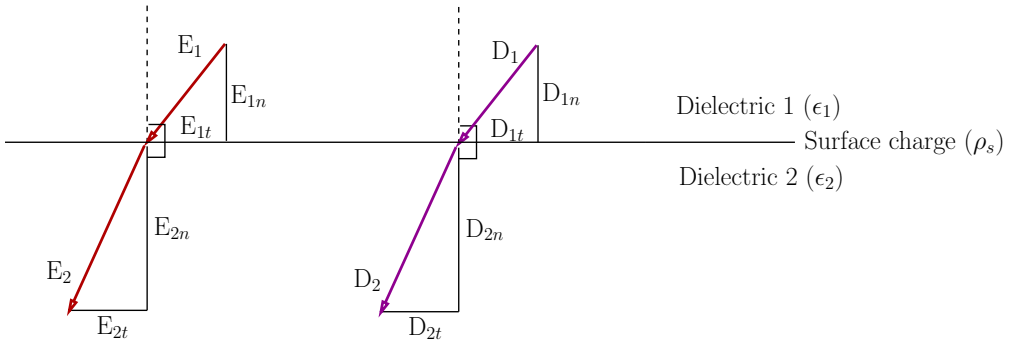

Figure 5.8. Electric field and dielectric displacement at the interface between two dielectrics.

components of electric field does not change. As a result, the electric field becomes more parallel to the layer. When the electric field passes from a high permittivity to a low permittivity material, the electric field gets more vertical at the interface.

Capacitances in the model (in Figure 5.6) were extracted as functions of the PZT thickness and IDT spacing, as shown in Figure 5.9. For PZT films with thicknesses

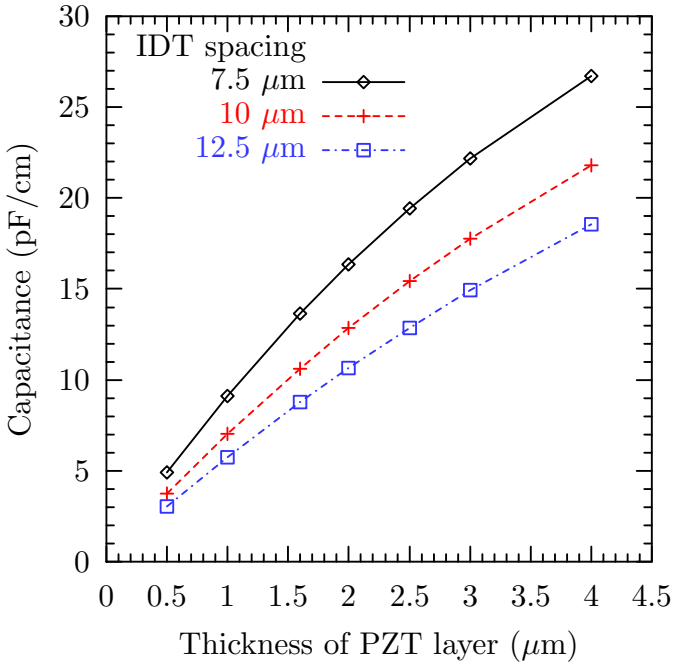

Figure 5.9. Calculated capacitances as functions of PZT thickness and IDT spacing.

less than 1 μm, the capacitance increases monotonically with thickness. It tends to

saturate at greater thickness. At greater depths, the interaction is minimal as the electric field is weak. In addition, the capacitance decreases as the IDT spacing increases as observed in Figure 5.5. It is important to notice that the capacitance in Figure 5.9 is the line capacitance (namely, the capacitance per unit length). To convert a measured capacitance from a diaphragm actuator into this capacitance value, the measured capacitance is divided by the length of the IDT electrodes. For ring–shaped IDT electrodes, summation of the circumference at the center of each gap between two IDT rings becomes the length, as given by:

$$l = \sum_{i=1}^{n} \left(2\pi \left(w + \frac{s}{2} + (w+s)(i-1) \right) 10^{-4} \right) \tag{5.5}$$

where l is the effective length, w and s are the width and spacing of IDT electrode, respectively, and n is the number of the electrode gaps. The unit of the line capacitance is F/m.

To estimate the relative dielectric constant of PZT films in diaphragm actuators, the capacitance as a function of relative dielectric constant of PZT layer was calculated and compared with the measured values. The relative dielectric constants of ZrO_2 and SiO_2 used are those given in Table 5.2. Errors caused by changes in dielectric constants of these materials are expected to be minimal since these materials have much lower dielectric constants than PZT. Figure 5.10 shows the capacitance as a function of the relative dielectric constant for the PZT layer. It linearly increases with relative dielectric constant. The estimated average relative dielectric constants of the PZT films in the diaphragm actuators was 664 with a standard deviation of 28.5. Table 5.3 summarizes the results. These values are smaller than that (850) from films with top and bottom electrodes as discussed in Section 4.3.3. This difference may come from the following reason. In the IDT electrode configuration, the in–plane dielectric constant largely controls the capacitance. The in–plane dielectric constant is expected to be smaller than the out–of–plane dielectric constant, since tensile stress in the PZT layer can increase

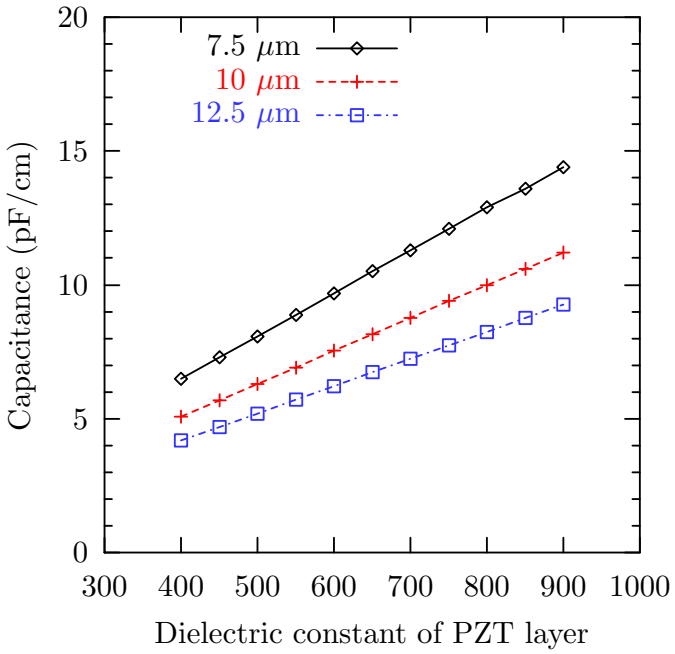

Figure 5.10. Simulated capacitance as a function of relative dielectric constant of PZT layer.

the tendency for the c–axis to be parallel to the film plane. Given the dielectric anisotropy in PZT, this could lower the permittivity in the radial direction.

Table 5.3. Calculation of the relative dielectric constant of PZT film.

IDT diameter (μm)	IDT spacing (μm)	Capacitance[1] (pF)	Capacitance[2] (pF/m)	Dielectric constants[3]
	7.5	26.47	10.38	645
700	10	18.61	8.27	659
	12.5	15.42	7.42	718
	7.5	20.07	10.39	645
600	10	12.91	7.92	631
	12.5	10.20	7.04	681
	7.5	13.67	10.99	683
500	10	9.0	8.104	646
	12.5	7.10	7.61	737

[1] measured capacitance from diaphragm actuators
[2] obtained by dividing the measured capacitance by the length of IDT electrodes using Equation 5.5
[3] obtained from Figure 5.10

5.4.3 Ferroelectric Properties

Voltage–induced charge output versus voltage hysteresis loops measured from diaphragm actuators was shown in Figure 5.11. The loops show excellent ferroelectric properties.

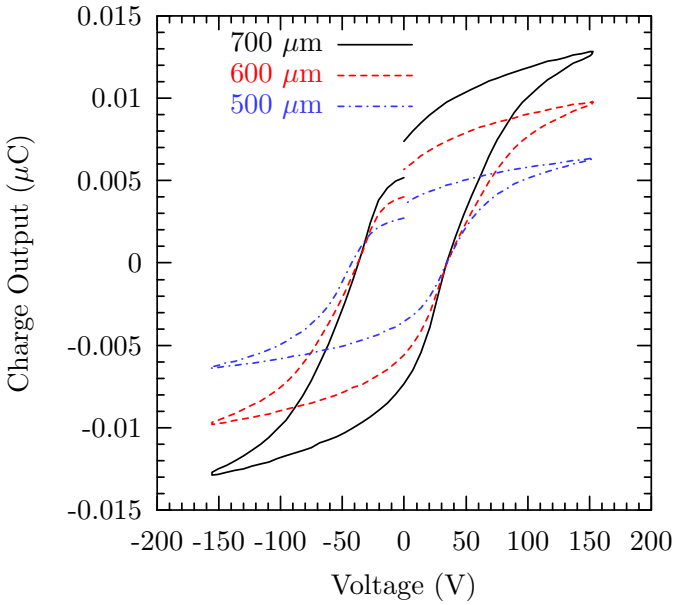

Figure 5.11. Voltage–induced charge output from three different IDT diameter diaphragm actuators.

To convert the voltage–induced charge output to polarization, the value was divided by the effective area, which was the IDT length (Equation 5.5) times the thickness of the PZT layer. The coercive field was obtained by dividing the applied voltage by the IDT spacing. As shown in Figure 5.6, the electric field was uniform between the IDT electrodes in the PZT layer. In addition, the voltage drop occurs mainly between the two IDT electrodes rather than under the IDT electrodes. Figure 5.12 shows the results. The calculated polarization–electric field hysteresis loops from three different size IDT electrode diaphragms overlapped one another, proving that the calculation of effective areas is reasonable. The remanent polarization is around 20 μC/cm^2 and the coercive field is $\sim$50 kV/cm. This value is comparable with the polarization and coercive field obtained from PZT films deposited on Pt-coated silicon wafers (see Section 4.3.3).

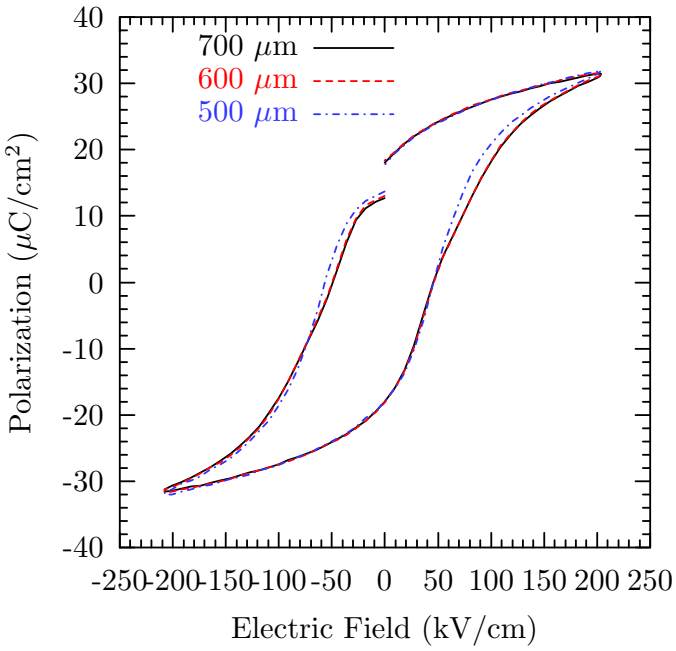

Figure 5.12. Calculated hysteresis loops of diaphragm structures of different diameter with IDT electrodes shown in Figure 5.11.

5.5 Vibration Characterization

The vibration characteristics of micromachined structures are of interest, both in terms of application in functional devices and in studying the material properties. In micromachined piezoelectric accelerometers, the first resonance determines the maximum operation frequency, since significant nonlinearity of the output signal occurs around the resonance frequency [7]. Many resonant sensors utilize shifts in the resonance frequency as probes to detect external stimuli [8, 9]. In micromachined cantilever structures, the resonance frequency depends on both the mass and Young's modulus of the constituent materials along with the geometric parameters such as the length, width and thickness of the structure. Assuming these geometric parameters, the Young's modulus of the structure can be determined from the resonance measurement. In addition, in clamped structures such as bridges and diaphragms, the residual stresses can be calculated from the resonance frequency.

In the limiting case, diaphragm structures behave as either membranes or plates.

Depending on the behavior, diaphragms show different characteristics in the mechanical and vibrational characteristics [10] [11]. For this reason, it is important to verify whether diaphragm actuators behave either as membranes or plates. In this section, the resonance frequency of diaphragm actuators were utilized to characterize their behavior. In addition, the residual stress of each diaphragm actuator was evaluated using the load–deflection method [11, 12]. The vibration characteristics of diaphragm actuators were evaluated under various conditions, such as ambient pressure, bias voltage and oscillation levels. Diaphragm actuators were excited either mechanically or electrically. The vibration modal shape at the resonance frequencies were evaluated by a vibrometer.

5.5.1 Measurement Set–up

Electrical Resonance Measurement Electrically excited resonances from diaphragm actuators were characterized by two different instruments. A HP4194A impedance–gain analyzer (Hewlett–Packard, Palo Alto, CA) was used to measure the impedance of diaphragm actuators as a function of frequency. One advantage of this method is that it is easy to analyze the vibration characteristics as a function of ambient pressure and temperature using either a vacuum chamber or oven, respectively. Figure 5.13 shows the setup for measuring impedance as a function of ambient pressure. The pressure in the chamber was monitored using a

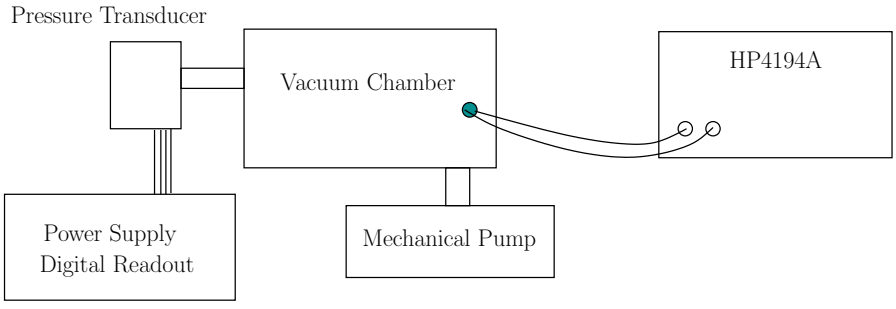

Figure 5.13. Set–up for electrical resonance measurement.

MKS Baratron Type 122 pressure transducer. A MKS PDR–C–2C power supply and digital readout was connected to the pressure transducer. Using this setup, resonance measurements were conducted at chamber pressures ranging from 760 Torr to below 1 Torr. In this measurement, a chip containing several diaphragm structures was bonded to a ceramic package with spacers between the chip and the package to prevent the diaphragms from being sealed. A scanning vibrometer (Polytec, Inc) was used to evaluate both resonance frequencies and the modal shapes of diaphragm actuators. The vibrometer is an optical instrument that can map the vibration of small structures by measuring velocity or displacement of selected points. For electrical resonance measurements, PZT films were poled at 3 E_C (coercive field) for 10 min at room temperature just before the measurements.

Mechanical Resonance Measurement Mechanical resonance was characterized by a scanning vibrometer which was used for the electrical resonance measurements. Instead of electrical signals, a shaker, which was activated by a 2–inch diameter piezoelectric actuator (Piezo systems, Inc., Cambridge, MA), was used to excite the diaphragm actuators.

Load–Deflection Measurement Figure 5.14 shows the set–up for measuring deflection as a function of applied pressure. A vacuum chuck with a suitable window and vacuum channel was machined from a solid aluminum block. The upper surface was finished using a 3 inch diameter fly cutter, which created a flat, smooth surface, providing a good seal with the diaphragm. A lever valve was used to subject the device to the vacuum created by a rotary vacuum pump. A needle valve was then used to regulate the applied vacuum level by controlled flow of air back into the system. A MKS Baratron Type 127 pressure transducer was connected to a MKS PDR–1–1C power supply and digital readout to monitor the pressure inside the chuck. The midpoint displacement measurement was conducted using a Wyko interferometer.

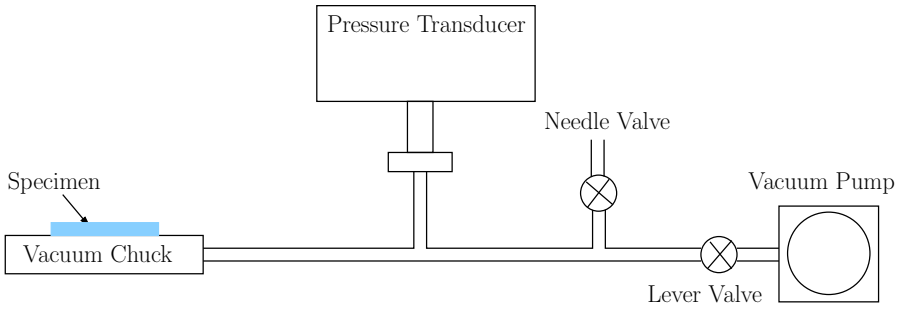

Figure 5.14. Load–deflection experimental set–up from [13].

Both electrical and mechanical resonance measurements using a scanning vibrometer were carried out by Northrop Grumman Corporation. In addition, the set–up for the load–deflection measurements was devised by R.L. Smith during his M.S. study [13].

Electrically–Induced–Deflection–Under–Pressure Measurement Figure 5.15 shows the set–up for measuring electrical deflections of diaphragm actuators under pressure. Compared to the load–deflection measurement set–up (see Figure 5.14), this set–up was designed to apply a positive pressure to the backside of the diaphragm actuator.

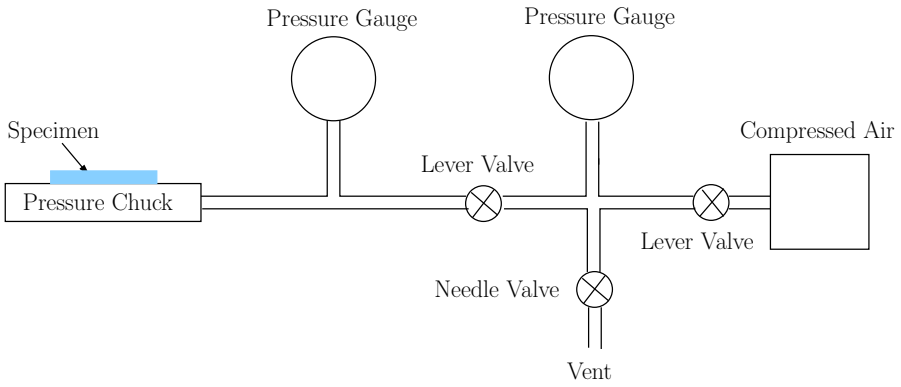

Figure 5.15. Deflection–under–high–pressure experimental set–up.

Compressed air was used as a pressure source. A needle valve then controlled the applied pressure level by changing the flow of air into the vent. To monitor the pressure inside the chuck and the line, two dial-type pressure gauges covering the

pressure range from -100 kPa to 200 kPa (Air Products, Allen town, PA) were used. A chip with several diaphragm actuators was attached to the chuck and the joint between the chip and the chuck was sealed by glue (extra fast setting epoxy by Harcros Chemicals, Inc., NJ). After electrical connections were made to the diaphragm actuators, electrically induced deflections under pressures were measured using a Zygo interferometer.

5.5.2 Membrane versus Plate Models for Diaphragm Actuators

Depending on details of the structure, diaphragms can act either as plates or membranes. In the case of an edge-clamped circular diaphragm, the natural frequencies are given by one of the following equations [11]: (the vibration equations of circular diaphragms are presented in Appendix A)

$$f = \frac{\alpha_1}{2\pi R}\sqrt{\frac{T}{\rho h}} \tag{5.6}$$

$$f = \frac{\alpha_2}{2\pi R^2}\sqrt{\frac{D_E}{\rho h}} \tag{5.7}$$

where f is the resonance frequency of the diaphragm, α_1,α_2 are constants determined by the vibration modes, R is the radius of the diaphragm, h is the diaphragm thickness, ρ is the diaphragm density, D_E is the flexural rigidity[2] of the diaphragm and T is the initial tension of the diaphragm.

[2] $\mathrm{D}_E = \frac{Eh^3}{12(1-\nu^2)}$, where E and ν are the Young's modulus and Poisson's ratio of the diaphragm, h is the diaphragm thickness

In the case of a membrane, the initial tension, which is usually induced by residual stresses in the deposited films, plays an important role in determining the resonance behavior. The resonance frequencies are inversely proportional to the size of the membrane as shown in Equation 5.6. In contrast, for a plate, the flexural rigidity, which indicates the stiffness of the structure, is more important and the resonance frequencies are inversely proportional to the square of the radii of the diaphragms as shown in Equation 5.7.

Figure 5.16 shows the three lowest resonance peaks for 700, 840, and 980 μm diameter actuators. To verify whether diaphragm actuators behave as membranes or plates, the resonance frequencies were measured and the three dominant resonance frequencies for diaphragms of different size were plotted as a function of the inverse of the diaphragm radii (1/R), as shown in Figure 5.17. As seen in Figure 5.17, these resonance frequencies have a 1/R dependence, indicating that the diaphragm actuators behave as membranes. For plates, the frequencies are inversely proportional to the square of the radii.

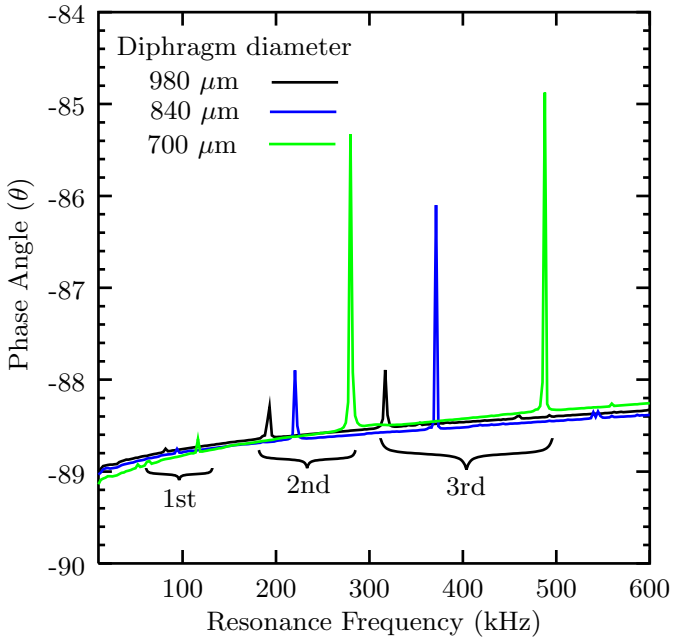

Figure 5.16. The three lowest resonance frequencies from several diaphragm actuators.

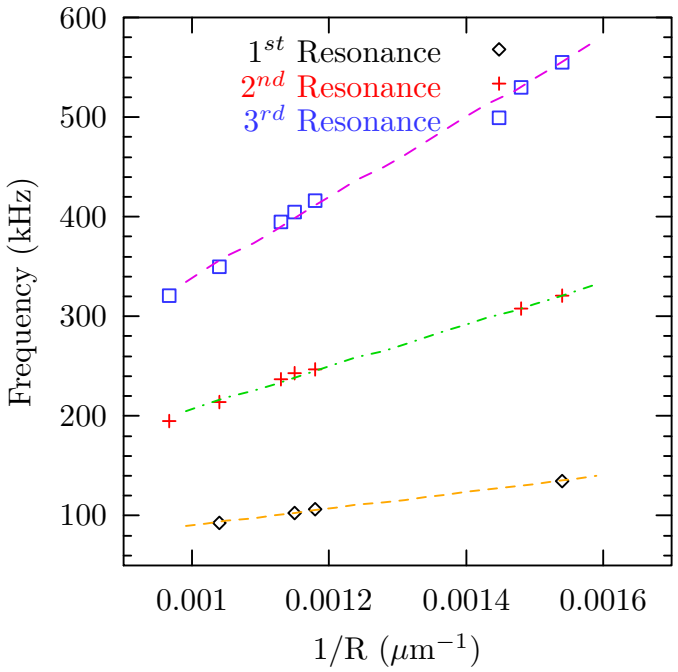

Figure 5.17. The three lowest resonance frequencies as a function of 1/R (diameter of diaphragm actuator).

5.5.3 Load Deflection Measurement

In section 5.5.2, it was shown that the diaphragm actuators behave as membranes rather than plates. For membranes, the residual stress in the structure is critical in understanding the vibration characteristics (Equation 5.6). In Chapter 4, the residual stress of a wafer with diaphragm actuators was evaluated by wafer curvature measurement. However, this method only evaluated the average residual stress of the structure across the wafer. For this reason, load–deflection measurements (bulge tests) were conducted to determine the residual stress of each diaphragm actuator.

Load–Deflection Model The load–deflection relationship of an edge clamped circular membrane, assuming that the deflection is small compared to its radius, is expressed by Equation 5.8 [11, 14].

$$P = \frac{8t}{3r^4}\frac{E}{1-\nu}d^3 + \frac{4t\sigma_0}{r^2}d \tag{5.8}$$

where P is the differential pressure, t is the diaphragm thickness, r is the radius of the diaphragm, d is the out–of–plane displacement, E is the Young's modulus, ν is the Poisson's ratio, and σ_0 is the residual stress. By measuring deflections as a function of differential pressure and fitting the data to Equation 5.8, the biaxial modulus[3] and residual stress can be obtained using known geometric parameters.

Load–Deflection Results Load–deflection experiments were conducted for diaphragms of different sizes. The diameters of tested diaphragms were between 800 and 1,400 μm. The deflections were measured at pressures up to 100 kPa. The maximum midpoint deflections at 100 kPa were in the range of 12.5 to 24 μm. A typical plot of differential pressure versus the midpoint deflection for a 980 μm diaphragm is shown in Figure 5.18

To estimate the biaxial modulus and the residual stress of the diaphragm actuator, the curve in Figure 5.18 was fitted to Equation 5.8. The R^2 value is 0.99939, indicating a very good fit between the model and the data. For diaphragm actuators, the Young's modulus was calculated by using the Poisson's ratio of 0.269 in Equation 5.8. The Poisson's ratio was calculated using a mixing rule for multilayer structures (Equation 5.9) [15] and the Poisson's ratios of layers in the diaphragm actuators in Table 5.4.

$$\nu_{eff} = \frac{1}{t}(\nu_1 t_1 + \nu_2 t_2 + \nu_3 t_3) \tag{5.9}$$

where ν_i and t_i are the Poisson's ratio and thickness of the i^{th} layer.

[3] biaxial modulus = $\frac{E}{(1-\nu)}$

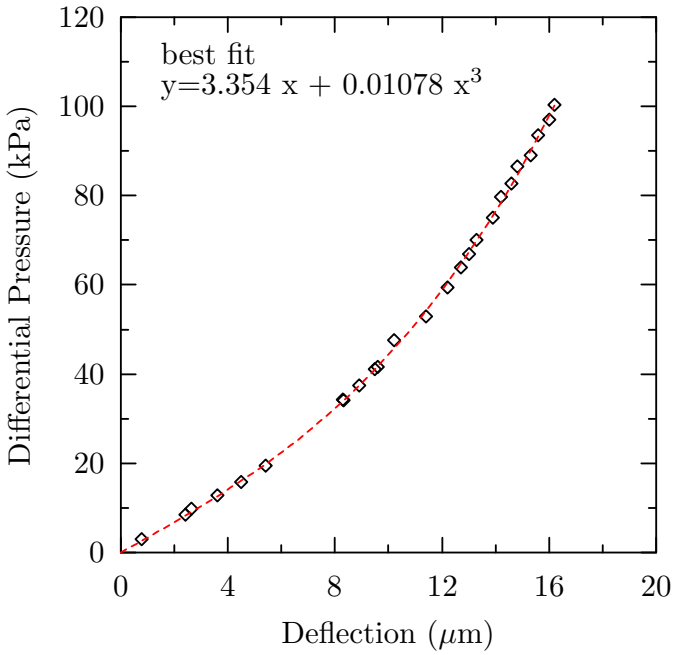

Figure 5.18. Deflections at the center of a 980 μm diameter diaphragm actuator as a function of differential pressure across the surfaces (data obtained from R.L. Smith, Northrop Grumman Corp.).

Table 5.4. Material properties of layers in diaphragm actuators [16].

Layer	Density (kg/m^2)	Thickness (μm)	Young's modulus (GPa)	Poisson's ratio
PZT	7600	1.6	101	0.3
ZrO_2	5500	0.3	160	0.27
SiO_2	2200	0.5	70	0.17

The estimated Young's modulus and residual stress are summarized in Table 5.5.

The average Young's modulus was 65.9 GPa with a standard deviation of 3.3 GPa. In addition, the average residual stress was 79.1 MPa with a standard deviation of 3.6 MPa. It was found that more reasonable residual stresses could be obtained when only deflection data below 5 μm at the mid–point were used [17]. For large deflections over 5 μm, neglecting the bending stress which arises due to the stiffness at the boundary of a diaphragm actuator may degrade the accuracy of the calculated residual stress. An ideal membranes does not have stiffness. However, in reality, diaphragms have finite stiffnesses. For this reason, in large deflection at

Table 5.5. Young's modulus and residual stress of diaphragm actuators based on large deflection response.

Diameter (μm)	$E_{effective}$ (GPa)	Residual Stress (MPa)
1375	68.7	83.6
1100	65.5	80.1
1100	69.7	79.3
950	61.9	78.8
800	63.5	73.5
Average	65.9	79.1
Standard Deviation	3.3	3.6

the mid–points, the stiffness of the diaphragms will influence the deflection. Table 5.6 summarizes the results using deflection data below 5 μm.

Table 5.6. Residual stress of diaphragm actuators based on medium deflection response.

Diamter (μm)	Residual Stress (MPa)
1375	84.0
1375	88.1
1250	84.7
1250	87.0
1100	86.1
1100	85.1
Average	85.8
Standard Deviation	1.5

As shown in Table 5.6, using medium deflection data, the standard deviation of residual stresses is reduced to 1.5 MPa. The resulting average residual stress is 86 MPa. Compared to the value (80 MPa) obtained from the wafer curvature measurement in Section 4.3.4, this is a reasonable value. The resulting Young's modulus was $\sim$66 GPa. This value is smaller than what is expected from Table 5.4. As described in Chapter 4, the zirconia may be porous, which would greatly reduce its Young's modulus, resulting in a significant reduction in the Young's moduli of the diaphragm actuators.

Finite Element Analysis Using information on the residual stess and Young's modulus of diaphragm actuators obtained in the previous section, load–deflection curves of various diameter diaphragms were simulated. The model was a circular diaphragm, which was clamped at the edge. The model was meshed using Shell99 elements, which can model multilayer structures [5]. In the modeled diaphragm, the average stress of 86 MPa was induced through a static analysis. Pressure loads were then applied on top of the diaphragms. Figure 5.19 shows expected results of various diaphragm actuators in size. The results were consistent with measured data.

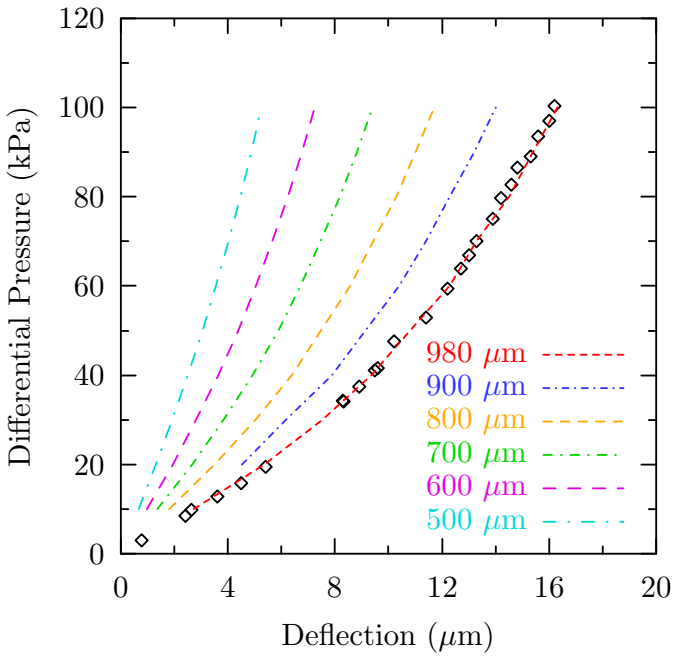

Figure 5.19. Simulated deflections of various diameter diaphragm actuators as a function of differential pressure and data (◇) from Figure 5.18.

5.5.4 Electrical versus Mechanical Resonance

The vibration characteristics of diaphragm actuators under electrical and mechanical excitation are compared in this section. In electrical excitation, a stress (or strain) is induced in the PZT film by electrical oscillation, generating the vibration. In contrast, in mechanical excitation, the diaphragm structure was forced

to vibrate with a shaker. Therefore, in electrical excitation, the IDT electrode configuration, which imposes a specific stress (or strain) distribution across the diaphragm, is expected to influence the vibration. The resonance frequencies observed for these two excitations are summarized in Table 5.7. There is no obvious difference in the positions of the resonance frequencies.

Table 5.7. Resonant frequencies for diaphragm actuators excited electrically and mechanically.

Diameter	01–mode		Difference	02–mode		Difference
(μm)	mechanical	electrical	(%)	mechanical	electrical	(%)
1000	80.94	81.88	1.1	191.3	190.6	-0.4
850	91.25	91.25	0.0	213.4	218.1	2.2
700	113.4	112.5	-0.8	274.7	275.0	0.1

However, the resonance modes resulting from electrical and mechanical excitations show obvious differences. It was found that electrical excitation favors symmetric modes, as shown in Figure 5.20.

The first vibration corresponds to the 01–mode of membrane vibration, which has one nodal circle, and the second vibration corresponds to the 02–mode. This vibration mode has two nodal circles without any nodal diameter. In addition to these two modes, the 11– and 21– modes, which are asymmetric, are expected. However, these modes were not observed experimentally in electrical excitation. It was hypothesized that failure to detect the asymmetric modes is due to the symmetry of the IDT electrodes. To verify this idea, resonance modes of a diaphragm excited mechanically were characterized. In mechanical excitation, the IDT electrode configuration is not expected to influence the vibration. Since ring–shaped IDT electrodes did not provide a good reflection surface for the interferometer, a diaphragm wih a solid circular electrode was used. It was found that asymmetric modes as well as symmetric modes could be excited as shown in Figure 5.21 and Figure 5.22.

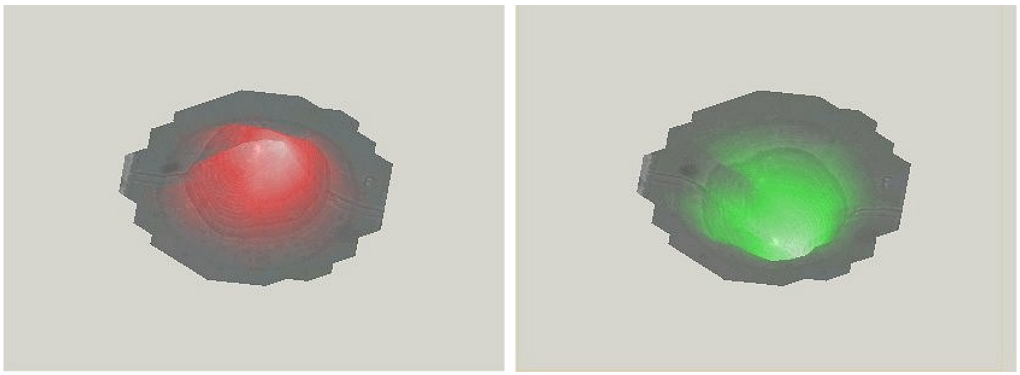

(a)

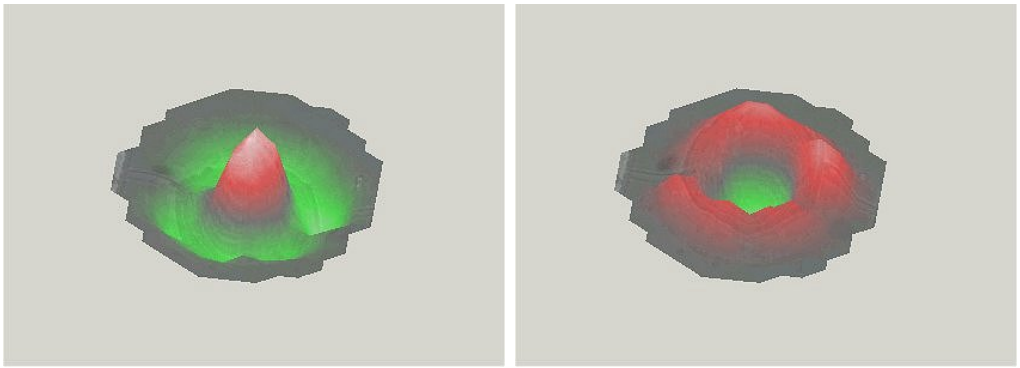

(b)

Figure 5.20. Symmetrical vibration modes (a) 01–mode, (b) 02–mode for a diaphragm actuator due to electrical excitation (courtesy R.L. Smith, Northrop Grumman Corp.).

Vibration Constant The residual stresses of diaphragm actuators were around 86 MPa. The tension (206 N/m) in the diaphragm actuators can be calculated by multiplying the residual stress with its thickness. By averaging the weighted theoretical densities of each layer to obtain the density of the diaphragm (in Table 5.4), constants for the 01, 02, and 03 vibration modes were calculated. Table 5.8 summarizes the result.

The calculated values are larger than the theoretical values. The error is partially due to uncertainty in the layer density of diaphragm actuators. For higher modes, the deviation between these two values increases. As presented in Table 5.8, when

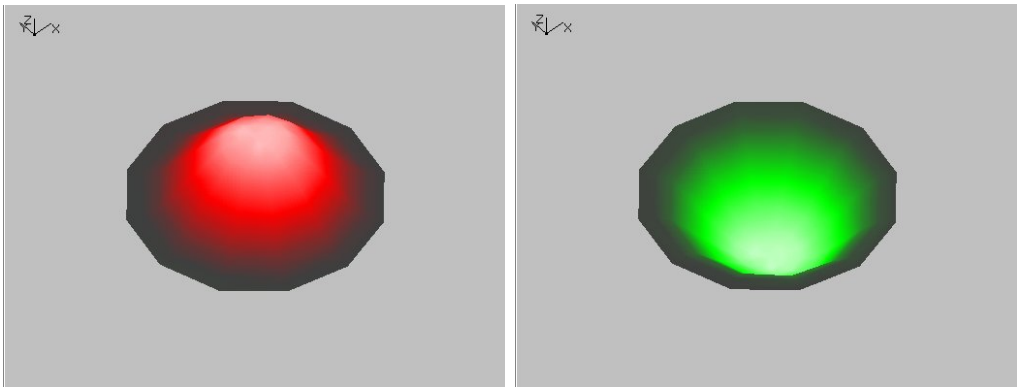

(a)

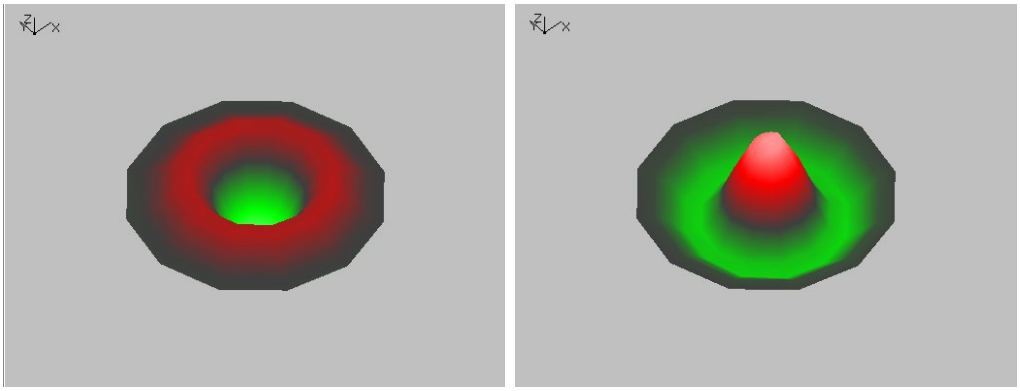

(b)

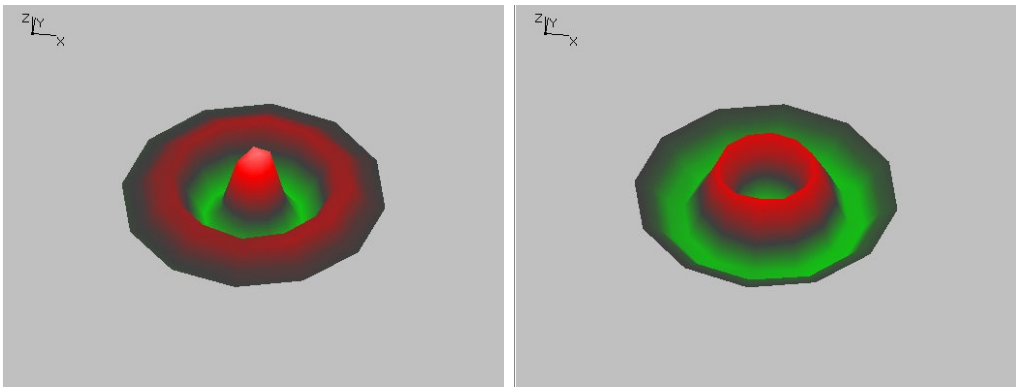

(c)

Figure 5.21. Symmetrical vibration modes (a) 01–mode, (b) 02–mode, and (c) 03–mode for a diaphragm actuator due to mechanical excitation (courtesy R.L. Smith, Northrop Grumman Corp.).

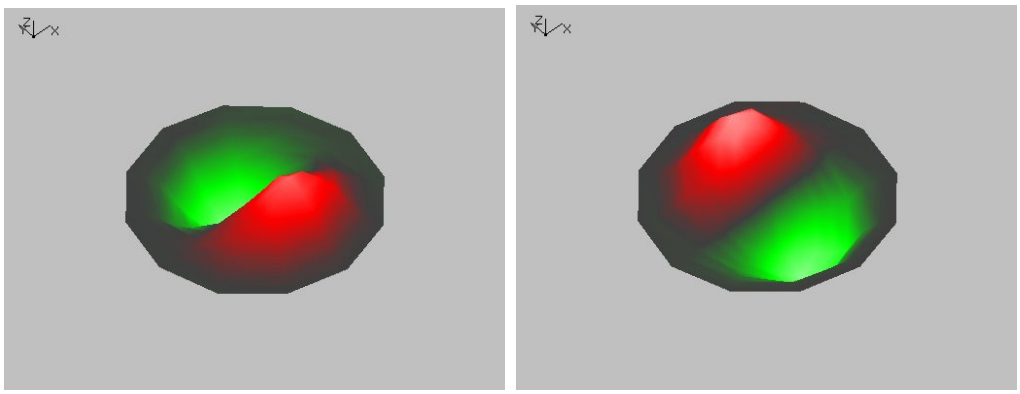

(a)

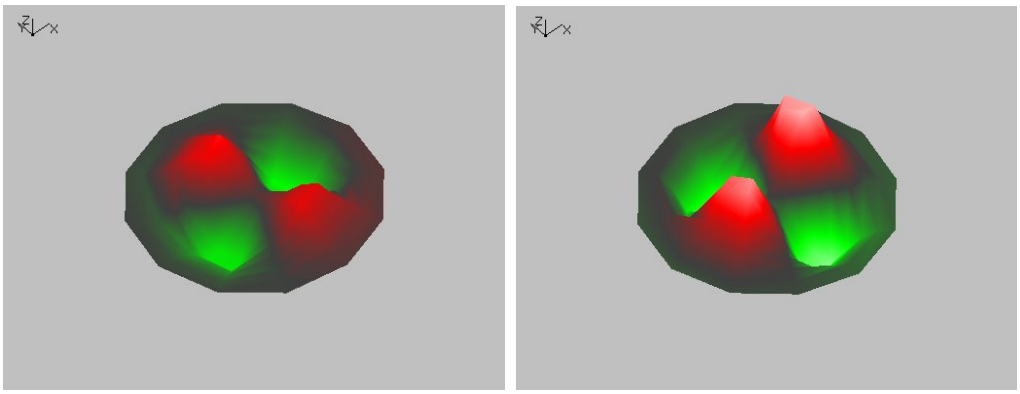

(b)

Figure 5.22. Asymmetrical vibration modes excited mechanically, (a) 11–mode and (b) 21–mode (courtesy R.L. Smith, Northrop Grumman Corp.).

the residual stress of a diaphragm actuator is extracted using resonance frequencies, the first mode is preferred to the other higher modes to obtain more accurate residual stresses from diaphragm actuators.

Table 5.8. Comparison of theoretical and calculated values of α_{mn}.

Mode (mn)	01–mode	02–mode	03–mode
Theoretical values	2.404	5.520	8.654
Calculated values (Standard deviation)	2.4653 (0.046)	5.693 (0.107)	9.572 (0.362)
Deviation	2.5%	3.1%	10.6%

5.5.5 Air Damping Effect

Figure 5.23 shows the admittance curves of a resonating diaphragm as a function of ambient pressure. This measurement used the 2^{nd} resonances from diaphragms since these resonances exhibited strong responses. As shown in this figure, the resonance frequencies change by 1% when the pressure changes from 727 Torr to 5 Torr. The primary cause is damping due to mass loading, which is dependent on the ambient pressure [18].

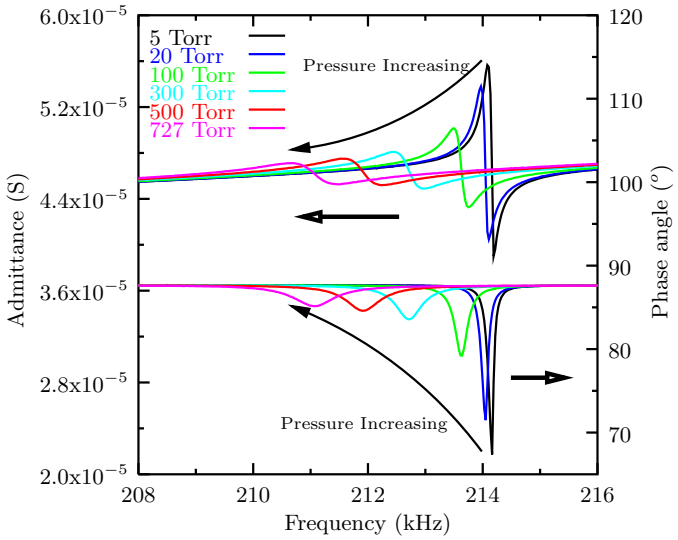

Figure 5.23. Admittance and phase of the 2^{nd} resonance peak of a 980 μm diameter diaphragm.

To evaluate the damping, the quality factor was calculated for pressures below 1 Torr up to 726 Torr. The quality factors were extracted by two methods, namely, a graphical and an analytical approach. Graphically, the locus of the admittance was used. From Figure 5.24, it is seen that the diameter of the locus increases

with decreasing ambient pressure. The quality factor was then calculated using

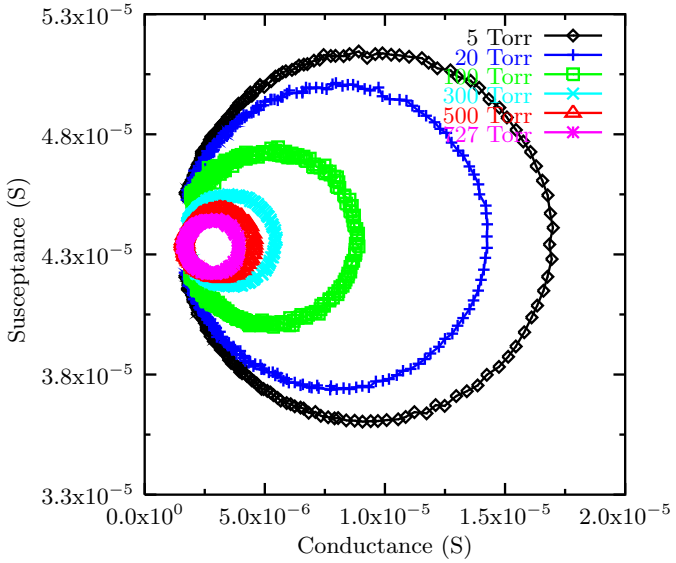

Figure 5.24. Admittance locus for the 2^{nd} resonance peak of a 980 μm diameter diaphragm as a function of ambient pressure.

Equation 5.10 [19].

$$Q = \frac{f_{max,G}}{f_{max,B} - f_{min,B}} \tag{5.10}$$

where Q is the effective quality factor, $f_{max,G}$ is the frequency at the maximum conductance, $f_{max,B}$ is the frequency at the maximum susceptance, and $f_{min,B}$ is the frequency at the minimum susceptance.

In addition to calculating the quality factor, the admittance curves were also fitted using an equivalent circuit shown in Figure 5.25 [19]. The circuit consists of a static capacitor in parallel with a motional arm, which has a resistance, a capacitor and an inductor. Using Mathematica (Wolfram, Inc.), the admittance curves were fitted to the admittance equation (as a function of frequency) derived from the equivalent circuit shown in Figure 5.25 and the best–fit parameters were obtained. For the admittance curve of a 980 μm diameter diaphragm at 5 Torr, the parameters are

shown in Table 5.9

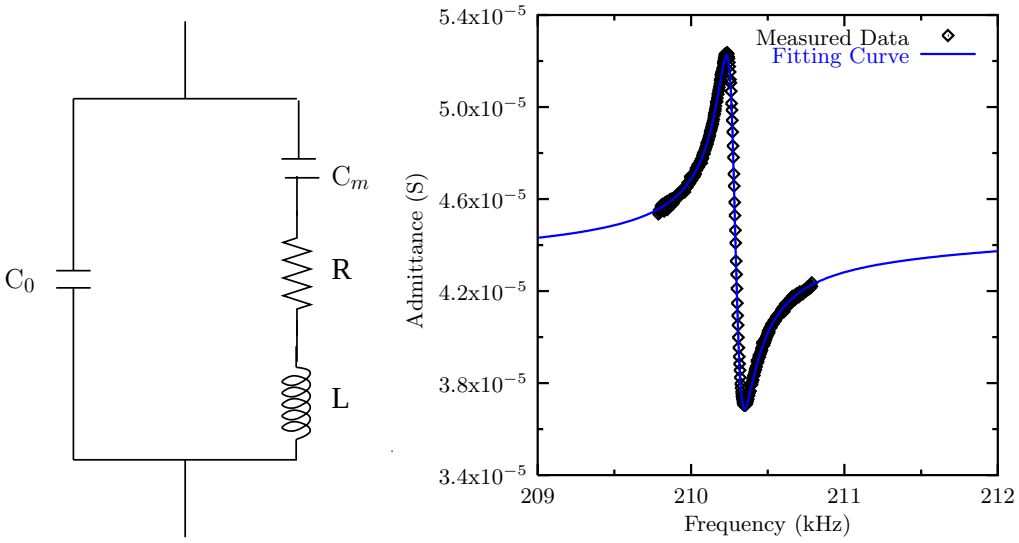

(a) (b)

Figure 5.25. (a) Equivalent circuit and (b) curve fitting of admittance data of a 980 μm diameter diaphragm measured at a pressure of 5 Torr.

Table 5.9. Best fitted values of the parameters for the equivalent circuit.

Parameter (unit)	C_0 (pF)	C_m (fF)	R (kΩ)	L (H)
Value	33.22	6.39	64.89	89.64

From these values, the quality factor was calculated by Equation 5.11:

$$Q = \frac{1}{R}\sqrt{\frac{L}{C_m}} \tag{5.11}$$

The quality factors for the 2^{nd} resonance of a 980 μm diameter diaphragm actuator calculated by the two methods described above are presented in Figure 5.26. Both methods provide similar numbers, with less than 2% deviation. The quality factor at 727 Torr is 250 and increases up to 2100 below 1 Torr.

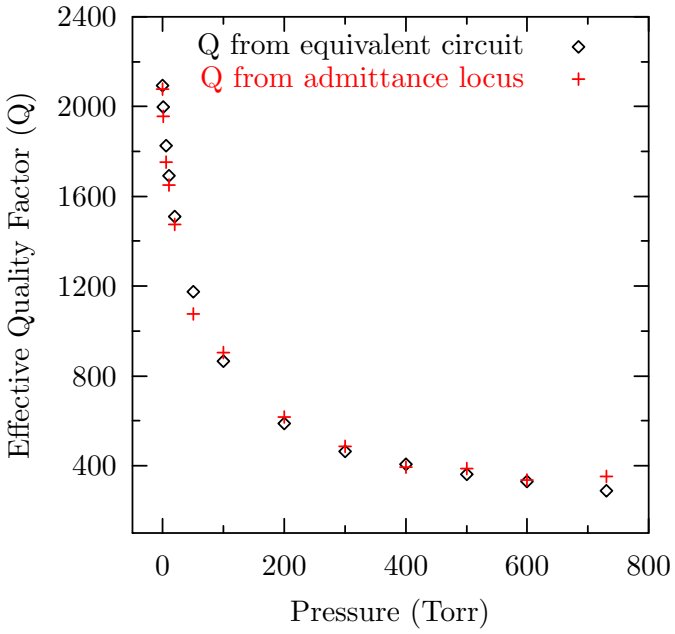

Figure 5.26. Effective quality factor for the 2^{nd} resonance of a 980 μm diaphragm as a function of ambient pressures.

5.5.6 Bias Voltage Effect

Figure 5.27 shows the phase angles of an 840 μm diameter diaphragm actuator with 7.5 μm IDT spacing as a function of applied bias voltage. With forward bias (electrical field parallel to the polarization) applied, the resonance frequency shifted to lower values, indicating the tension of the diaphragm was decreasing (see Equation 5.6). On the other hand, the resonance frequency first shifted to higher values, when reverse bias was applied. At still higher reverse bias (around or above the coercive voltage), the resonance frequencies started to move to lower frequencies.

To explain the bias effect, the configuration of the ring–shaped IDT electrodes should be considered. When a piezoelectric diaphragm is poled, the polarization is aligned parallel to the plane. When a forward bias is applied, the piezoelectric layer expands in the radial direction due to the d_{33} piezoelectric constant. This acts against the initial residual tensile stress, resulting in a decrease in the tension

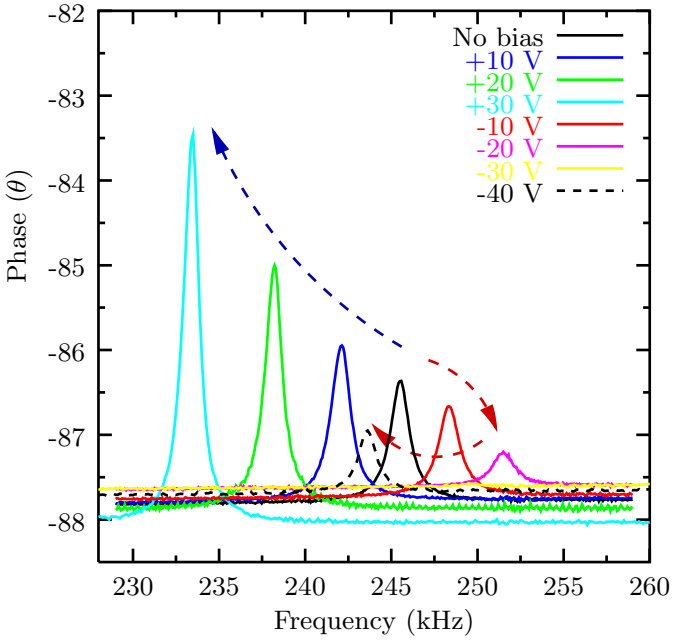

Figure 5.27. Phase angles of an 840 μm diameter diaphragm as a function of bias voltage with an IDT spacing of 7.5 μm.

of the diaphragm. Simultaneously, a tangential contraction occurs due to the d_{31} piezoelectric constant, which might increase the tensile stress of the diaphragm. However, the net response is dominated by the d_{33} piezoelectric response, since d_{33} is around twice as large as d_{31} [3]. As a result, the forward bias decreases the stress (or tension) of the diaphragm, resulting in a shift of the resonance to lower frequencies. On the other hand, when a reverse bias is applied, the resonance will shift to higher frequencies, since the bias increases the tension. However, around the coercive voltage, the PZT is first depoled and then re–poled parallel to the applied bias. From this field onward, the bias becomes a forward bias and decreases the resonance frequencies. Thus, resonance measurements provided a means to detect depoling and repoling of the PZT layer.

Compared to a diaphragm actuator with ring–shaped IDT electrodes, d_{31}–mode diaphragms, which have two parallel top and bottom electrodes, have a different polarization condition. When the d_{31}–mode diaphragm is forward–biased, the diaphragm should try to shrink in both the radial and tangential directions, resulting in increased tensile stress. Under a reverse bias, the tensile stress of the diaphragm

should decrease. To verify this understanding, the bias–effect of a d_{31}–mode diaphragm actuator[4] was characterized (see Figure 5.28). As observed in the figure, the behavior of a d_{31}–mode diaphragm was opposite to that of diaphragm actuator with ring–shaped IDT electrodes.

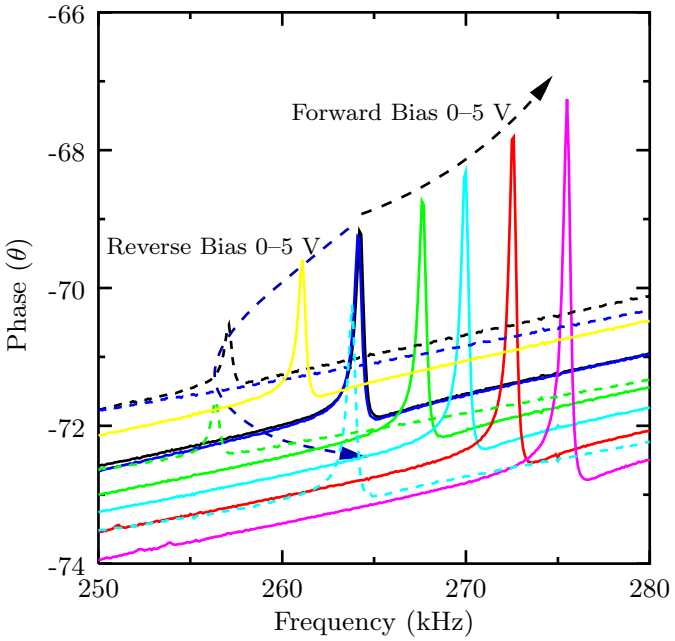

Figure 5.28. Phase angles of a 900 μm diameter d_{31}–mode diaphragm as a function of bias voltage.

To calculate the stress induced by bias voltage, Equation 5.12 was derived from Equation 5.6.

$$\Delta\sigma = \sigma_0 \left(\frac{f_b}{f_0}\right)^2 - \sigma_0 \tag{5.12}$$

where $\Delta\sigma$ is the induced stress, σ_0 is the initial residual stress, f_b is the resonance frequency at a certain bias and f_0 is the resonance frequency without bias.

Using Equation 5.12, the induced stress for the IDT–mode actuators using 86 MPa as the residual stress was calculated to be about -2 MPa at 10 V forward or reverse bias. Because of repoling at higher reverse bias voltages, the stress

[4] d_{31}–mode diaphragm actuators were provided by Northrop Grumman Corporation. The structure was Pt/1.4 μm PZT/Pt/Ti/0.5 μm SiN_x (low stress nitride).

which can generated by reverse bias is limited to below 8 MPa. Due to repoling, diaphragm actuators will have a limit to flex upward under reverse bias as discussed in Chapter 3.

5.5.7 Nonlinear Vibration

Nonlinearity in vibrating structures was investigated. There are two main sources. One is nonlinearity in material properties such as the stiffness and dielectric constant of the vibrating structure. The other comes from the geometric effect. Many PZT bulk resonators show so–called *softening spring effects*, where the resonance frequency decreases with increasing vibration amplitude [20]. This is mainly attributed to a decrease in the stiffness of the structure due to motion of non-180 ° domain walls. Clamped structures such as bridges and diaphragms present *hardening spring effects*, where the resonance frequency increases with increasing vibration amplitude [18]. This effect is caused since the stiffness or tension of the structure increases with an increase in vibration amplitude. For diaphragm actuators, it is interesting to confirm which behavior is observed. If the softening spring effect occurs, it means that the non-180° domain walls are very active. Otherwise, the hardening spring effect means that the geometric effects associated with a clamped structure are dominant.

Figure 5.29 (a) shows the impedance and phase of an 840 μm diameter diaphragm actuator at an oscillation voltage of 0.1 V as a function of the ambient pressure. The second resonance of the diaphragm was used in this measurement since this resonance was a dominant resonance from the diaphragm actuator. With decreasing ambient pressure, the effect of nonlinearity becomes more visible. The phase angles show an abrupt drop with increasing frequency, indicating a hard spring effect [18]. The nonlinearity of the structure was also checked as a function of oscillation voltage, as shown in Figure 5.29 (b). The phase angles were measured at 10 Torr as a function of oscillation voltage. Nonlinearity occurred at ac voltages greater than 0.05 V. The solid lines were obtained in up–sweep and the dashed

lines were obtained on decreasing frequency. With increasing oscillation voltages, the frequency gap between up and down sweeps increased, indicating an increase in the nonlinearity [18].

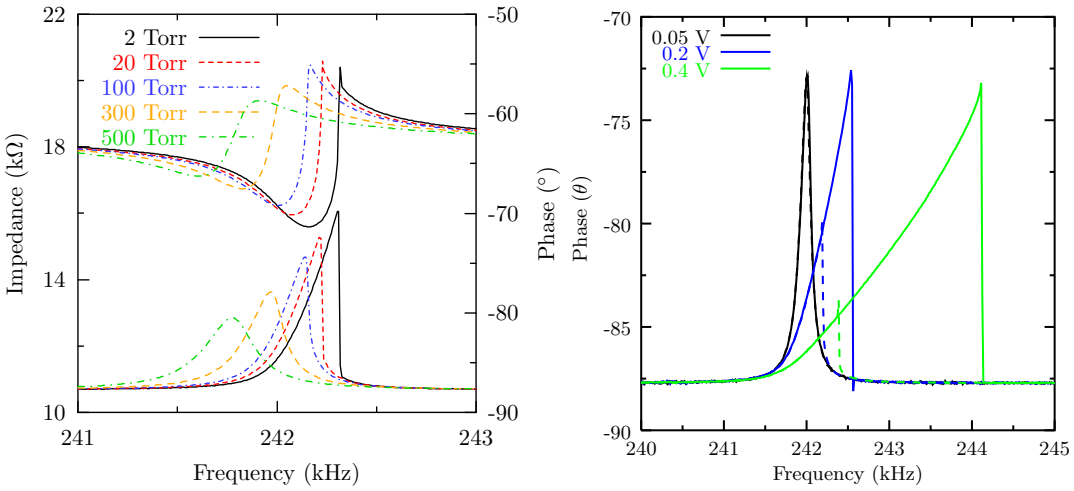

(a) (b)

Figure 5.29. Nonlinear vibration of the 2^{nd} resonance of an 840 μm diameter diaphragm with an IDT spacing of 7.5 μm as a function of (a) ambient pressure and (b) oscillation voltage measured at 10 Torr.

In Figures 5.29, the diaphragms show the hard spring effect. This effect arises due to increases in the vibration displacement at higher oscillation voltages and reduced ambient pressures. Increased displacements induce additional tension in the structures, making the diaphragm actuators stiffer. In the diaphragm structure, geometric nonlinearity is more dominant than material nonlinearity in governing the high amplitude response.

5.5.8 Non–180° Domain Motion

In the previous section, nonlinear effects were measured at relatively low oscillation voltages compared to the IDT spacings of the diaphragm actuators. Therefore, it is possible that the applied oscillation voltages were not enough to activate non-

180° domain walls. Hence, the resonance frequencies were measured without bias after the diaphragm was poled.

Figure 5.30 shows the shift in the 2^{nd} resonance frequency of 840 μm diameter diaphragm under different poling conditions. The diaphragm was poled at voltages between 40 and -25 for 2 min. First, the minimum resonance frequency under forward bias was measured. Poling at 40 V for more than 2 min did not decrease the resonance frequency (when the diaphragm was poled at 3 E_C for 10 min, the resonance frequency fell within the ranges of 240 to 250 kHz (see Figure 5.27)). The maximum resonance frequency was then measured by applying a reverse voltage of -25 V to the diaphragm. When a higher reverse bias was applied to the diaphragm, the diaphragm was depoled and repoled parallel to the applied bias. The resonance frequency started to shift to lower frequencies.

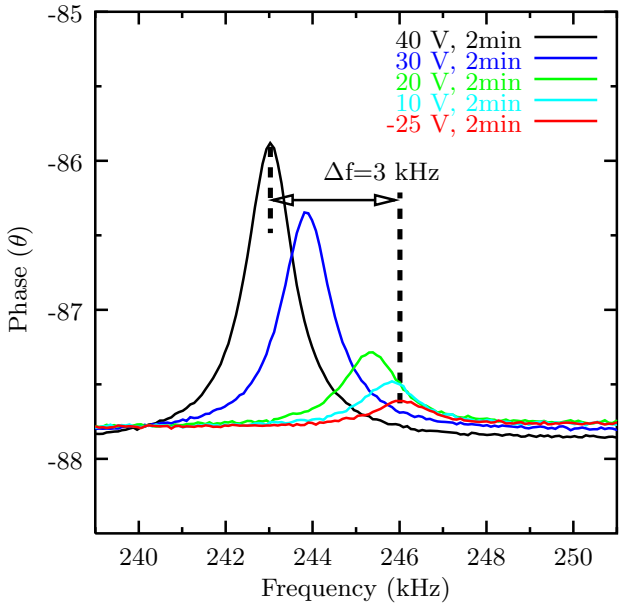

Figure 5.30. Shifts in the 2^{nd} resonance frequency of an 840 μm diameter diaphragm with an IDT spacing of 7.5 μm with different poling conditions.

Shifts in the resonance peaks in Figure 5.30 clearly indicate the motion of the non–180° domain walls. The change in the stress of the PZT film (using the measured residual stress of the diaphragm of 86 MPa) was 3 MPa and the induced strain was

calculated to be 2 to 3×10^{-5} assuming the Young's modulus and Poisson's ratio of the PZT are 66-101 GPa and 0.3 [5].

Uchida et al. calculated strains caused by the non–180° domain wall motion in PZT ceramics [21]. They assumed that PZT ceramics were randomly oriented. When an electric field was applied, domains which had a small angle (less than a characteristic angle) were completely reoriented. When the non-180° domains are completely reoriented, theoretical strains[6] induced parallel to the applied electric fields in PZT(57/43) and PZT(53/47) ceramics are calculated to be 3.5 to 4×10^{-3}. In addition, experimentally, when these ceramics were poled at around 4 E_C, strains induced by motion of the non-180° domains were in order of 10^{-4}. From these results, it is clear that the non-180° domain motion of the poled PZT layer (Figure 5.30) in the diaphragm actuator is limited. The main reason may be due to the stress field associated with the residual stress in diaphragm actuator. Thus, to create additional strain, the diaphragm needs to overcome this residual stress. In addition, the PZT film is still clamped by an elastic passive silicon oxide. Even if non-180 ° domain walls move at poling voltages, the domain walls may recover to the original state due to the restoring force from the passive layer. It would be very useful to quantify this directly by examining the hysteresis of these actuators under large signal unipolar drive.

5.6 Electrically–Induced Deflections

Electrically–induced deflections of diaphragm actuators are important in operation of MEMS pumps since the pumping effect is related to the stroke volume generated when the diaphragm actuators on the chambers flex down (see Chapter 3). Deflections of diaphragm actuators were measured using a Zygo interferometric

[5] 66 GPa is the minimum Young's modulus of the PZT layer from the load-deflection measurements

[6] Equations and data used for this calcuation were taken from [21]

profiler (Zygo, Inc)[7]. A chip with several diaphragm actuators was packaged on a ceramic package (see Section 5.5.1). DC voltages up to 200 V were applied to the diaphragm actuators using a power supply (Harrison 6200 B DC Power Supply) connected to a voltage amplifier (790 Series, Power Amplifier, PCB Piezotronics, Inc., Depew, NY).

Figure 5.31 shows deflection profiles of a diaphragm actuator with ring-shaped IDT electrodes for different applied electric voltages. Without a dc voltage, the diaphragm was almost flat (within ∼0.3 μm). With 120 V applied, the diaphragm was depressed by 4.3 μm at the center and was raised by 0.4 μm near the electrode boundary.

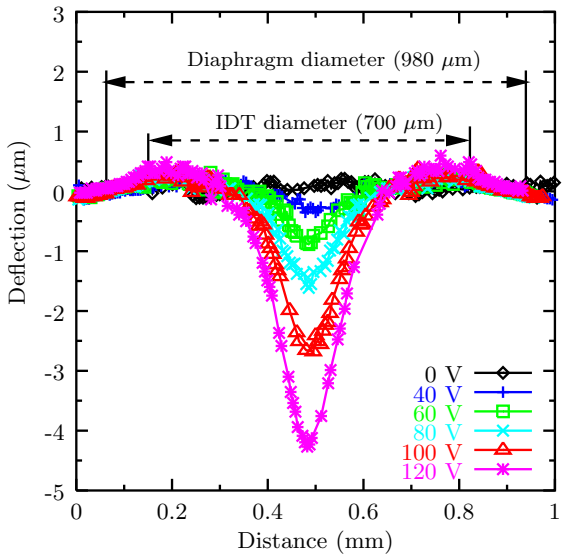

Figure 5.31. Deflections of a 980 μm diameter diaphragm (700 μm diameter IDT electrode) as a function of applied voltage with an IDT spacing of 10 μm.

A 3–dimensional plot of the diaphragm surface (shown in Figure 5.32) shows that the deflection has a funnel shape, where the radial curvatures from the center of the diaphragm are convex when viewed from the top and the tangential curvatures are concave. To obtain micrometer scale vertical deflections, electric fields above the coercive field (50 kV/cm) had to be applied to the diaphragm. In this condition, the piezoelectric layer will always expand regardless of the initial polarization

[7]the Zygo interferometer is similar to the Wyco interferometer which was used in the load–deflection measurements.

direction, since the applied electric fields will reorient the direction of the polarization. For this reason, large deflections of the diaphragm actuators were downward only. These results are consistent with finite element analysis presented in Chapter 3. d_{31}-mode diaphragm actuators and diaphragm actuators with parallel IDT electrodes presented deflections less than 0.5 μm even though higher electric fields than 200 kV/cm were applied.

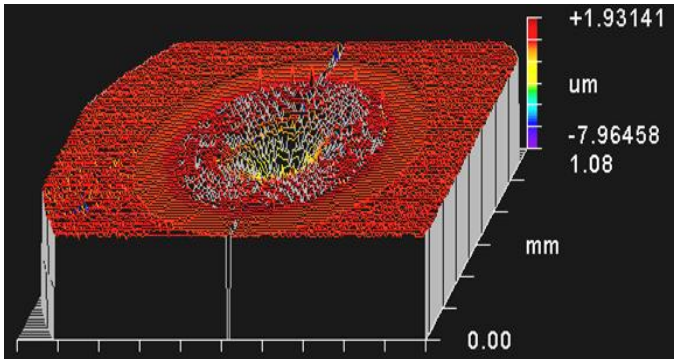

Figure 5.32. 3–dimensional deflection–map of a 980 μm diameter diaphragm (700 μm IDT diameter).

Figures 5.33 show center-deflections from diaphragm actuators with different diaphragm diameters and different IDT spacings. With a given voltage, center-deflections from the diaphragm actuators were proportional to the diameters. In addition, diaphragm actuators with wider IDT spacings generated larger deflections. As mentioned in Figure 5.7 (b), the electric field between the IDT electrodes is largely parallel to the layers. Therefore, PZT layer between the IDT electrodes mainly generate lateral strain (or stress). With a given electric field and finger width, the active region in diaphragm actuators increases with the IDT spacing. However, to obtain large deflections at a low voltage, diaphragm actuators with narrower IDT spacings were appropriate.

In Figures 5.33, a threshold field of around 80 kV/cm for the deflections is observed. Simulation results in Figure 3.16 do not show such a threshold. Probably, this threshold is caused by the residual stress of diaphragm actuators [8]. This threshold field seems to depend on the stress of the layers between the IDT electrodes rather

[8]In the simulation in Figure 3.16, effect of the residual stress was not considered due to difficulty in applying the residual stress to the model.

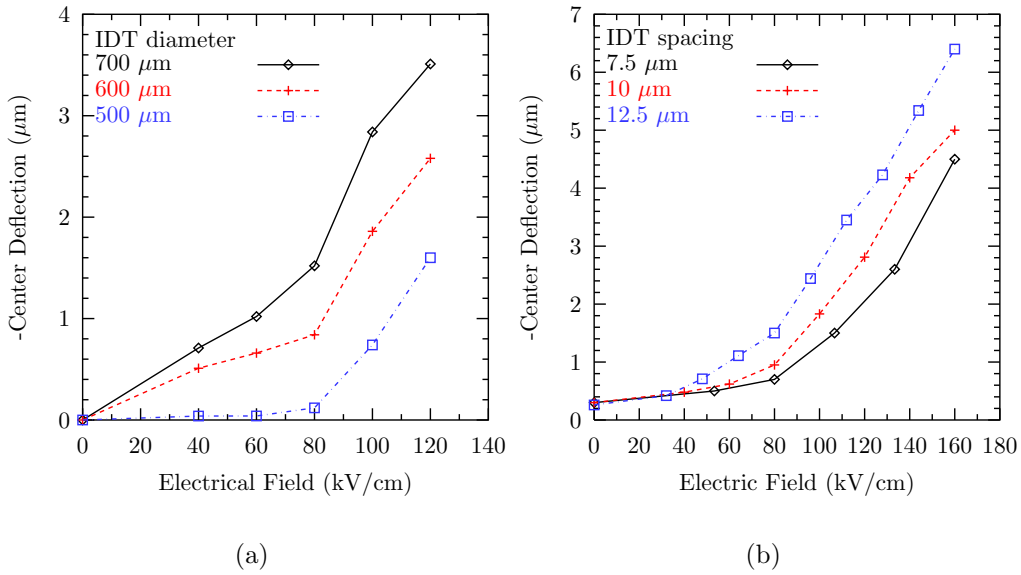

Figure 5.33. Deflections of diaphragm actuators with (a) different IDT diameters (namely 980, 840, and 700 μm) and (b) different IDT spacings of 7.5, 10, and 12.5 μm (700 μm IDT diameter and 980 μm diaphragm diameter).

than the total stress of the diaphragm actuators since diaphragm actuators with different IDT spacings in Figure 3.16 (b) presented the same threshold field. With a given electric field, the change in the total stress induced in diaphragm actuators is proportional to the IDT spacing. Therefore, if the threshold depends on the total stress, diaphragm actuators with different IDT spacing should present different threshold fields.

Assuming that piezoelectric stress from the PZT layer between the IDT electrodes overcomes the residual stress at the threshold electric field, the piezoelectric coefficient (e_{33}) can be estimated as follows:

In the diaphragm actuators, only the PZT layer is electrically active. The stress caused by the PZT layer will overcome the residual stress of the diaphragm at the threshold. Therefore, the piezoelectric coefficient was obtained by dividing the residual stress (86 MPa) by the threshold electric field (80 kV/cm) and multiplying the resulting value by the thickness ratio of the diaphragm to the PZT.

The piezoelectric coefficient (e_{33}) was calculated to be 16 C/m^2. This value is reasonable considering that e_{31} values of randomly oriented PZT films are in the range of -5 to -7 C/m^2 [22]. If this hypothesis on the origin of the threshold field is correct, then it suggests that one good way of increasing the available vertical deflection would be to decrease the tension holding the diaphragm taut.

To check whether electrically-induced deflections are reproducible, the deflection hysteresis of diaphragm actuators was evaluated (see Figure 5.34). The diaphragm actuator was not poled before this measurement. It took around 2-4 min to collect each data point by a Zygo interferometric profiler. Therefore, poling during the measurement couldn't be avoided. The maximum deflections remained constant regardless of the order of the sweep. In addition, the initial value didn't change after a sweep. This indicates that any strain caused by non-180° domain wall motion recovers to its original state at zero bias.

The degree of hysteresis is important for actuators since it provides information on thermal and mechanical loss and is defined by the following equation [23]:

$$Degree\ \ of\ \ hysteresis\ \ \% = \frac{\Delta d}{d_{max}} \tag{5.13}$$

where Δd is the difference in deflection for increasing and decreasing paths at half maximum of the electric field and d_{max} is the deflection at the maximum electric field. The degrees of hysteresis for the diaphragm actuator in Figure 5.34 were estimated to be around 20 % for the first sweep and $\sim$ 10 % for the second and third sweeps. After the first sweep, the diaphragm actuator was poled and the domain structures were reconfigured. Therefore, in the following sweeps, the degree of the hysteresis is expected to be reduced.

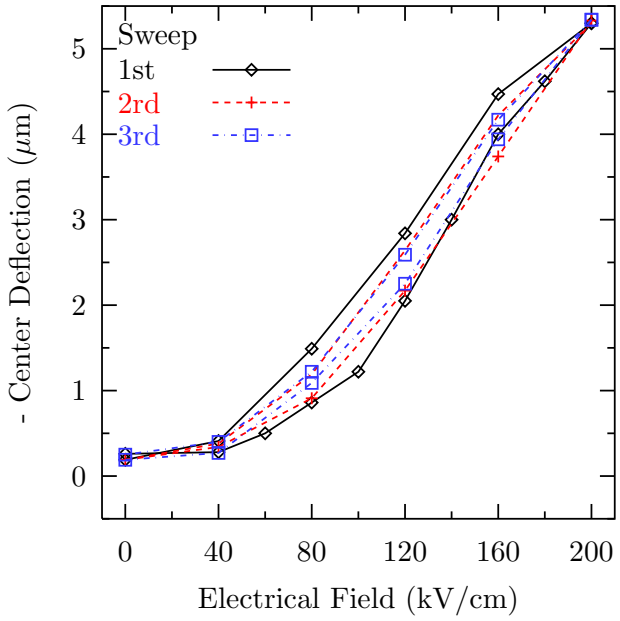

Figure 5.34. Deflection hysteresis of an 840 μm diameter diaphragm actuator (600 μm IDT diameter) with an IDT spacing of 10 μm.

Electrically-Induced Deflections Under Pressures The electrically-induced deflections of diaphragm actuators working against a static pressure were characterized to provide information about whether or not the piezoelectric actuators could work against a load. As shown in Figure 5.35, the center deflection of an 840 μm diaphragm actuator under a differential pressure of 40 kPa without bias was upward and around 6.7 μm, which is consistent with the load deflection data in Figure 5.19. At 160 kV/cm, the center deflection under the same pressure increased to about 7.1 μm. Since the direction of electrically–induced deflection of IDT–mode diaphragm actuators is downward (see Figure 5.31), this seems contradictory. However, as seen in Figure 5.27, the piezoelectrically-induced stress under forward bias reduces the diaphragm stress in IDT–mode diaphragm actuators. Therefore, the increase in deflection with bias is due to the decreased stress of the diaphragm.

Figure 5.36 shows deflection profiles of the 840 μm diameter diaphragm actuator at 160 kV/cm under various differential pressures (0 to 40 kPa). At higher pressures, the deflection profiles bulged. It is interesting to note that the deflection profiles

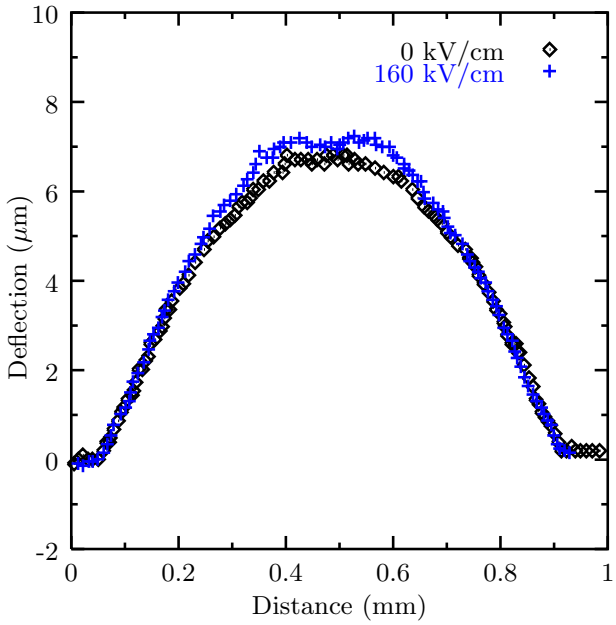

Figure 5.35. Deflections of an 840 μm diameter diaphragm actuator (600 μm IDT diameter with an IDT spacing of 12.5 μm) without bias and at 160 kV/cm under a differential pressure of 40 kPa.

under a differential pressure of 40 kPa continued to show a dimple at the center due to electrically–induced deflection. However, above a differential pressure of 10 kPa, the diaphragm actuator doesn't show downward stroke (center deflection is over 0). With increasing pressure load, the diaphragm started to bulge from the boundary where there is no IDT electrode coverage. Note that IDT electrode coverage of this diaphragm was around 70 %. Hence, increasing the coverage of IDT electrode on a diaphragm actuator might be helpful in increasing the resistance against pressure load. In terms of pump operation, it is necessary to prevent the chambers in a peristaltic pump structure from being pressurized over 10 kPa. Thus, channels between the chambers should be designed to have enough flow-conductance.

5.6.1 Finite Element Modeling

The dependence of the electrically–induced deflections on the IDT configuration was simulated using the same finite element model in Figure 3.14. It was done to

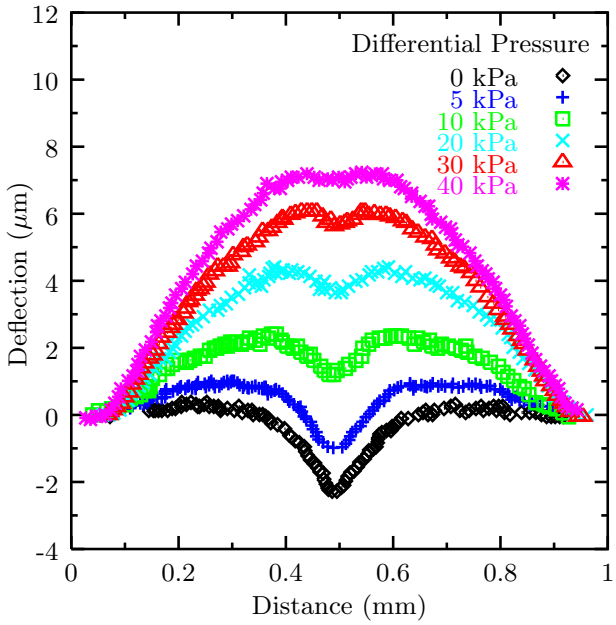

Figure 5.36. Deflections of an 840 μm diameter diaphragm actuator (600 μm IDT diameter with an IDT spacing of 12.5 μm) at 160 kV/cm under various pressures.

optimize the deflections available from diaphragm actuators. Calculated deflections as a function of the diaphragm diameter and IDT diameters are shown in Figure 5.37. The center deflections are proportional to the diaphragm diameter and the ratio of the IDT to the diaphragm.

In addition, the center-deflections were simulated with different thicknesses of the active and passive layers in a diaphragm actuator using the same finite element model in Figure 3.14. Table 5.10 summarizes the results. For a given thickness of active layer, the center-deflections increased with decreasing thickness of the passive layer. When the thickness of the passive layer is fixed, the center-deflections of a diaphragm actuator initially increased with increasing thickness of the active layer and subsequently saturated. This effect can be explained by considering the deformation of the passive layer when the active layer expands.

Assuming a 1-dimentional unimorph structure, when the active layer expands, the passive layer should also expand to generate large deflections. The force balance between the active and passive layers can be expressed by the following equation

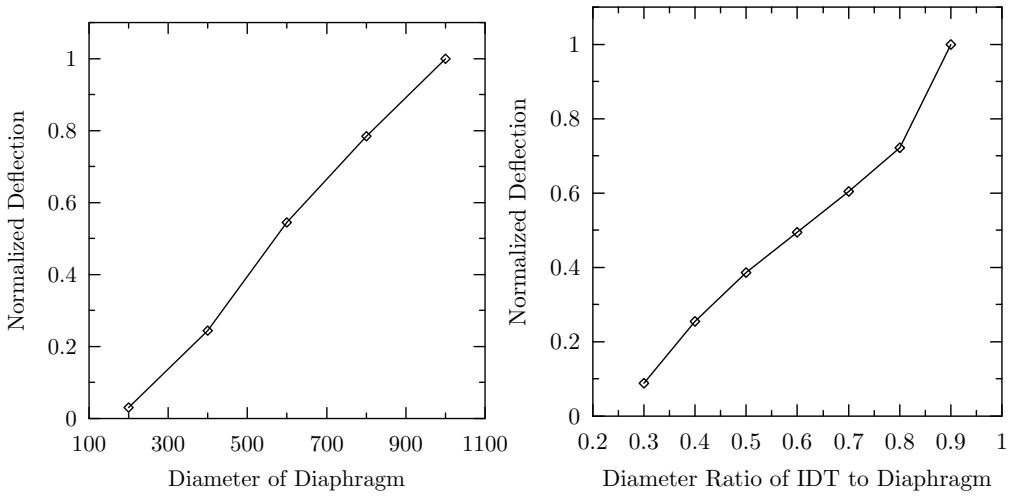

(a) (b)

Figure 5.37. Simulated deflection of a diaphragm actuator as function of (a) diaphragm diameter and (b) ratio of IDT to diaphragm diameter, normalized to the maximum deflection.

Table 5.10. Simulated center-deflections of diaphragm actuators with different thickness ratio of the active and the passive layer.

active layer thickness (μm)	passive layer thickness (μm)	deflection
1	1	1
1.5	1	1.09
2	1	1.12
3	1	1.06
1	0.5	1.19
1	0.2	1.37

[1] The deflections are normalized by the deflection of a diaphragm with a thickness ratio of 1.

[24]:

$$E_a t_a (x_p - x_e) = E_n t_n x_e \tag{5.14}$$

where E_a and E_n are the Young's modulus of the active and the passive layers, t_a and t_n are the thickness of the active and the passive layers, x_p is the induced

strain by the piezoelectric response of the active layer, x_e is the equilibirum strain at the interface between the active and the passive layer.

$$x_e = \frac{(E_a t_a)}{(E_a t_a + E_n t_n)} x_p \tag{5.15}$$

From Equation 5.15, with a given strain of x_p, the equilibrium strain increases when the thickness of the passive layer is reduced or the thickness of the active layer increases. However, when the thickness of the active layer is much larger than that of the passive layer, the strain saturates.

From this result it is clear that to obtain larger deflections from diaphragm actuators, a thin SiO_2 layer and a thick PZT layer are appropriate. However, there is a trade-off, since, a thick PZT layer also increases the residual stress of the diaphragm actuators, making the structures stiffer.

5.6.2 Annular–Ring Shaped IDT Electrodes

In a diaphragm actuator with ring-shaped IDT electrodes, the piezoelectrically-generated stress was concentrated at the center of the diaphragm, creating sharp deflections in the middle (as shown in Figure 5.32). As diaphragm actuators for pump structures, the sharp deflections reduce stroke volume. To overcome this problem, the IDT electrodes were modified to annular shaped IDT electrodes, which had inactive solid circles at the center (see Figure 5.38).

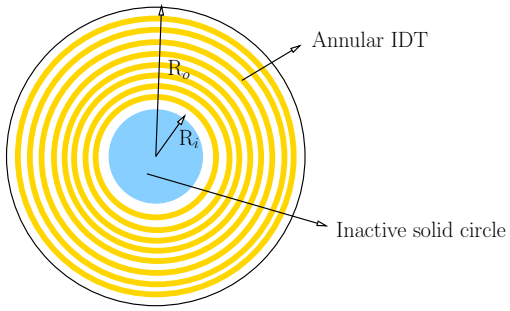

Figure 5.38. Schematic representation of an annular electrode showing the inactive region in the middle of the diaphragm, R_0 is the outer diameter of the IDT electrode (diaphragm diameter) and R_i is its inner diameter.

Deflection profiles of a diaphragm with an annular electrode were simulated as a function of the size of the central solid circle. As seen in Figure 5.39, deflection profiles become flatter with increasing size of the inactive circle. However, at the same time, deflection amplitudes also decreased (see Figure 5.40). To verify this prediction, diaphragm actuators with inactive metal circles at the center were fabricated using the same fabrication process discussed in Section 5.2 except that Pt was used as the top electrode and patterned by a RIE using a gas mixture of Ar (40 sccm) and Cl_2 (10 sccm) at 10 mTorr with a power of 600 W. The diaphragms had 800 μm diameter IDT electrodes covering 85 % of the diaphragms to increase deflections. Figure 5.41 shows a fabricated diaphragm with an annular electrode. The spacing and width of the IDT electrodes were around 4.5 and 10.5 μm, respectively [9].

[9]The IDT spacing became narrower while the IDT electrodes were patterned by the RIE. The designed IDT spacing and width were 7.5 μm.

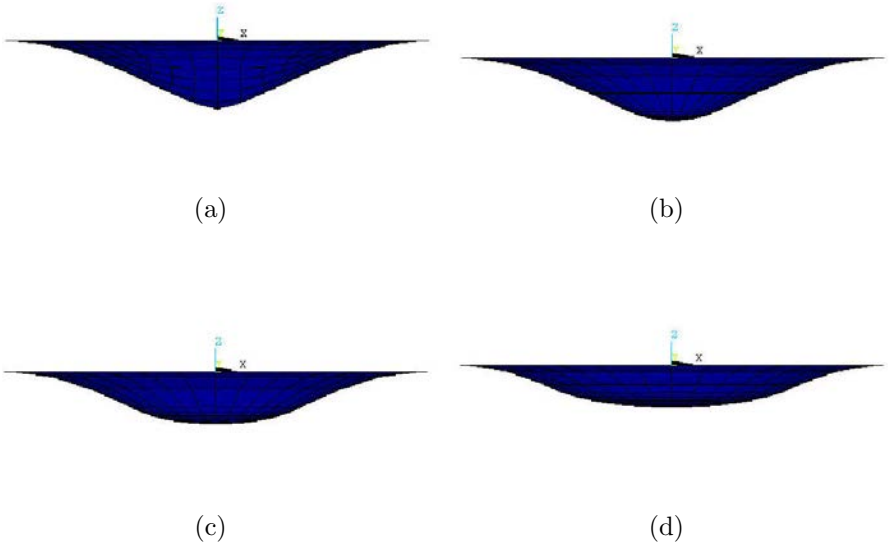

Figure 5.39. Modeled deflection shapes at the ratio of inner diameter of annular IDT electrode to diaphragm diameter of (a) 0%, (b) 20 %, (c) 40 %, and (d) 60 % (% = the ratio of R_i to R_o in Figure 5.38), vertical displacements are all at the same scale.

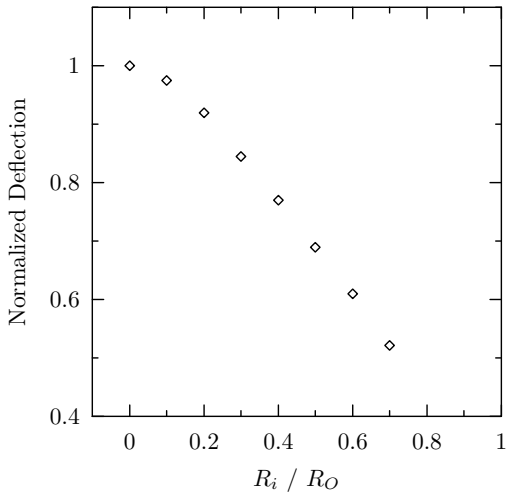

Figure 5.40. Calculated electrically–induced deflections as a function of ratio of inner diameter (R_i) of IDT electrode to diaphragm diameter (R_O) when the same level of stress (20 MPa) is imposed.

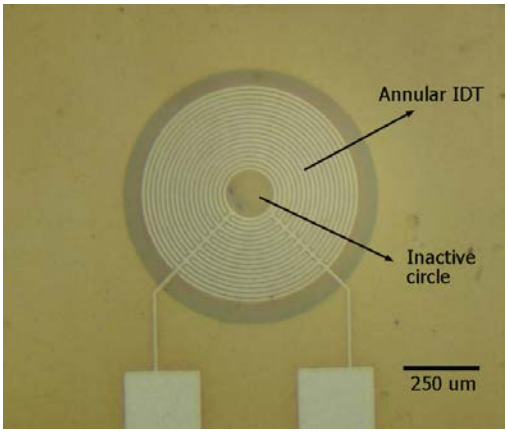

Figure 5.41. Fabricated diaphragm actuator with annular IDT electrodes (150 μm diameter inactive circle).

Figure 5.42 shows the deflections of diaphragms with different inactive circle sizes when 100 V is applied to the IDT electrodes. As expected from the simulations in the previous section, the deflection profiles became flatter with increasing size of the inactive circle. There is a corresponding reduction in the center–deflections. The flat areas are almost the same diameter as the inactive areas in the diaphragm actuators. Thus, annular IDT electrode configurations can be used to increase the

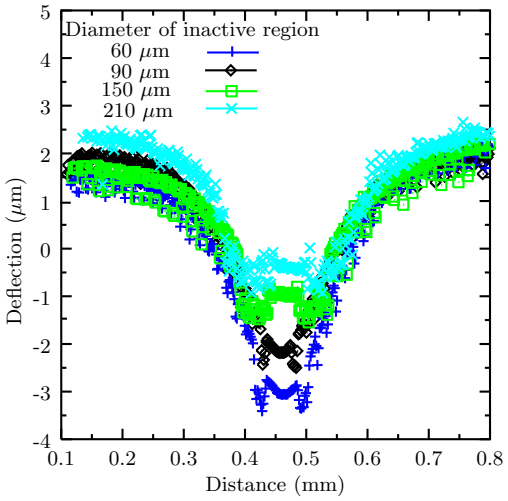

Figure 5.42. Deflections of 800 μm IDT diameter diaphragms with different inactive center circles of 60, 90, 150, and 210 μm in diameter when 100 V is applied to the IDT electrodes.

volume strokes as long as the deflections touch the bottom of a chamber in the MEMS pump structures.

5.7 Conclusions

Diaphragm actuators were successfully fabricated by bulk micromachining. PZT piezoelectrics in the actuators show good dielectric and ferroelectric properties. The dielectric constants are around 660 with dielectric losses below 2 % at 10 kHz. The remanent polarizations and coercive fields were 20 μC/cm^2 and 50 kV/cm, respectively. The diaphragm actuators behaved more like membranes rather than plates since the resonance frequencies were inversely proportional to the diaphragm radii. The residual stress was 86 MPa and the Young's modulus was 66 GPa. The resonance frequencies of the diaphragm actuators were similar regardless of the excitation methods. Under mechanical drive, both symmetric and asymmetric modes were excited. However, in electrical excitation, the symmetric modes were dominant. The quality factor of the diaphragm actuators was 250 at 727 Torr and increased to 2100 below 1 Torr. When a forward bias was applied to the diaphragm actuator, the tensile stress of the diaphragm decreased due to the ring-shaped IDT configuration. Under reverse bias, the tensile stress increased. However, because of repoling under a reverse bias greater than the coercive voltage, the achievable tensile stress generated was limited to 8 MPa. Diaphragm actuators show geometric nonlinearity when the diaphragm vibrates with a high amplitude. Deflection of 700 μm IDT diameter diaphragm with 10 μm IDT spacing was $\sim$4.3 μm at an applied field of 120 V. The deflection behavior can be explained by considering both the d_{31} and d_{33} piezoelectric constants. In addition, an annular IDT electrode configuration, which has an inactive region at the center generated a flatter deflection profile at the center, which is useful to increase the stroke volume for MEMS pumps.

References

[1] S.V. Krishnaswamy, *Private Communication*, 2002.

[2] F. Laermer *U.S. Patent No. 5,501,893 (Mar. 26. 1996).*

[3] A.J. Moulson and J.M. Herbert, *Electroceramics*. Chapman and Hall, London, 1990.

[4] B. Xu, Y. Ye, L.E. Cross, J.J. Bernstein, and R. Miller, "Dielectric Hysteresis under Transverse Electric Fields in Sol–Gel Lead Zirconate Titanate Films Deposited on ZrO_2 Passivated Silicon," *Integrated Ferroelectrics*, vol. 24, pp. 19–31, 1999.

[5] *ANSYS 5.5 manual, ANSYS, Inc., Canonburg, PA, 1998.*

[6] D. Cheng, *Field and Wave Electromagnetics*. Addison–Wesley Publishing Company, Inc., 1989.

[7] L.-P. Wang, "Microelectromechanical Systems (MEMS) Sensors Based on Lead Zirconate Titanate (PZT) Films," PhD thesis, The Pennsylvania State University, 2001.

[8] D.W Burns, J.D. Zook, R.D. Horning, W.R. Herb, and H. Guckel, "Sealed–Cavity Resonant Microbeam Pressure Sensor," *Sens. and Actuators A*, vol. 48, no. 3, pp. 179–186, 1995.

[9] J.C. Andle and J.F. Vetelino, "Acoustic Wave Biosensors," *Sens. and Actuators A*, vol. 44, no. 3, pp. 167–176, 1994.

[10] M. Sheplak and J. Dugundji, "Large Deflections of Clamped Circular Plates under Initial Tension and Transitions to Membrane Behavior," *Journal of Applied Mechanics*, vol. 65, pp. 107–115, 1998.

[11] S.P. Timoshenko and S. Woinowsky–Krieger, *Theory of Plates and Shells*. Singapore: McGraw–Hill, 1959.

[12] M.K. Small and W.D. Nix, "Analysis of Accuracy of the Bulge Test in Determining the Mechanical Properties of Thin Films," *J. Mater. Res.*, vol. 7, 1992.

[13] R. Smith, "Accelerated Fatigue Testing and Reliability Modeling of MEMS Actuator," Master's thesis, The University of Maryland – Baltimore County, 2002.

[14] E.I. Bromley, J.N. Randall, D.C. Flanders, and R.W. Mountain, "A Technique for the Determination of Stress in Thin Films," *J. Vac. Sci. Technol. B*, vol. 1, no. 4, pp. 1364–1366, 1983.

[15] J. Jones, *Mechanics of Composite Materials, 2nd Ed.* Taylor and Francis, Inc., Philadelphia, 1999.

[16] E. Hong, S.V. Krishnaswamy, C.B. Freidhoff, and S. Trolier-McKinstry, "Fabrication of Piezoelectric Diaphragm using Lead Zirconate Titanate (PZT) Films," *presented in Materials Research Society Symposium, Boston, USA*, 2001.

[17] R. Smith, *Private Communication*, 2003.

[18] W. Weaver, Jr., S.P. Timoshenko, and D.H. Young, *Vibration Problems in Engineering*. New York: John Wiley and Sons, 1990.

[19] T. Ikeda, *Fundamentals of Piezoelectricity*. Oxford University Press, New York, 1996.

[20] Q.M. Wang, Q. Zhang, B. Xu, R. Liu, and L.E. Cross, "Nonlinear Piezoelectric Behavior of Ceramic Bending Mode Actuators under Strong Electric Fields," *J. Appl. Phys.*, vol. 86, no. 6, pp. 3353–3360, 1999.

[21] N. Uchida and T. Ikeda, "Electrostriction in Perovskite-Type Ferroelectric Ceramics," *Japan. J. Appl. Phys.*, vol. 6, no. 9, pp. 1079–1088, 1967.

[22] R. Wolf, "Temperature Dependence of the Piezoelectric Response of Lead Zirconate Titanate Films for MEMS Applications," Master's thesis, The Pennsylvania State University, 2001.

[23] A. Dogan, K. Uchino, and R.E. Newnham, "Composite Piezoelectric Transducer with Truncated Conical Endcaps "Cymbal"," *IEEE Transactions on Utrasonics, Ferroelectrics, and Frequency Control*, vol. 44, no. 3, pp. 597–605, 1997.

[24] T.-B. Xu, Z.-Y. Cheng, and Q.M. Zhang, "High-Performance Micromachined Unimorph Actuators Based on Electrostrictive Poly(Vinylidene Fluoride-Trifluoroethylene) Copolymer," *Appl. Phys. Lett.*, vol. 80, no. 6, pp. 1082–1084, 2002.

Chapter 6

MEMS Piezoelectric Peristaltic Pumps

This chapter discusses design, fabrication and characterization of MEMS pumps for a MEMS mass spectrograph on a chip [1]. The micropumps are peristaltic pumps operated by piezoelectric diaphragm actuators. The structures were fabricated by surface micromachining techniques, which used silicon as a sacrificial material and a XeF_2 process for the release. This process development and characteristics of the MEMS pumps are presented in detail here.

6.1 Design of MEMS Pumps

The rationale behind designing micropump structures has been discussed in Chapter 3. Incorporating a pumping system into a MEMS mass spectrometer system requires fabrication of a miniature pump. The required pressure for operation of the MEMS mass spectrometer is achieved by employing a differential pumping

scheme that includes several pump structures. As mentioned in Chapter 3, surface micromachining is expected to miniaturize a pumping system to be incorporated into a MEMS mass spectrometer chip. In this study, two different pump structures in terms of the base structure (chamber and channel) and the IDT configuration were investigated. The second design was modified with ideas learned from the first iteration.

6.1.1 Base Structure of MEMS Pumps

The base structure, which consists of chambers and channels, determines the shape and size of a MEMS pump. The size of this base structure was limited to less than 5 × 2 mm. Two different chamber diameters were used in one design. The large chambers were 750 or 650 μm in diameter and the small ones were 450 or 400 μm. Chambers and channels were 3–4 μm in depth. This depth was chosen based on the deflection data in Chapter 5 and consideration of feasibility in both deposition and the removal of the sacrificial silicon. With increasing depth, a thicker sacrificial silicon is required to fill in the chambers and channels and it will take more time to remove it. The purpose of this study was to demonstrate the fabrication idea of surface micromachined piezoelectric peristaltic pumps presented in Chapter 3 and confirm pumping action using the fabricated pump structures. The designed base structure is presented in Figure 6.1. It consists of five circular chambers and interconnected parallel channels. The chambers at both ends of the structure are portholes, which are used as access holes for XeF_2 gas during the release process. After the pump structures are released, they serve as inlet or outlet ports.

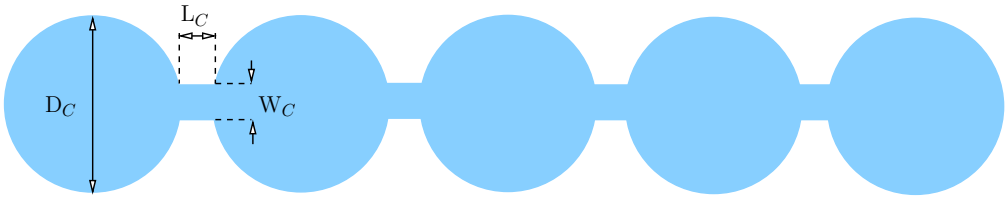

Figure 6.1. Base structure of a MEMS pump.

6.1.2 Layer Structure of MEMS Pump

Figure 6.2 shows the cross–sectional view of a pump structure, consisting of six layers: a passivation silicon oxide, sacrificial silicon (removed in the figure), a passive layer (for the diaphragm actuators), ZrO_2, PZT, and Cr/Au (for the IDT electrode). The layers were selected based on discussions in Section 3.1.3 (fabrication scheme for the peristaltic pump) and Chapter 5.

The pump structures are fabricated using silicon as a sacrificial material and are released by a XeF_2 process. Therefore, an etch stop layer to protect the base structure is required. It is known that XeF_2 does not etch photoresist, thermally grown silicon dioxide, Al, and Au [2, 3]. In this study, thermally grown silicon dioxide was selected due to the high temperature processes required to deposit ZrO_2 and PZT films. Diaphragms in the pump structure (passive, barrier, and active layer) consist of the same type of stack as was used in the diaphragm actuators described in Chapter 5 with some modifications. Instead of a thermally grown SiO_2, a low temperature silicon oxide (LTO) was utilized since it is difficult to grow dense thermal oxide from either amorphous silicon or polycrystalline silicon sacrificial materials. Attempts to do so typically led to oxidation of all of the sacrificial Si, making removal impossible. Like the diaphragm actuators, ZrO_2 was chosen as a Pb–diffusion barrier between the LTO and the PZT. The passive layer consisted of either a LTO layer or a stack of ZrO_2/ LTO. The ZrO_2 layer beneath the LTO was investigated as a protective barrier for the LTO during the XeF_2 release process. The LTO layer was 0.7 μm thick and the thickness of the PZT layer was 2.0 or 3.0 μm. Assuming that the LTO behaves like thermally grown oxide, the residual stresses of PZT/ZrO_2/LTO (or PZT/ZrO_2/LTO/ZrO_2) are in range from 67 to 93 MPa based on stress values of the layers discussed in Chapter 4. With increasing thickness of the PZT layer in the stack, the residual stress will become more tensile. Table 6.1 summarizes the thicknesses of the layers used in the fabrication.

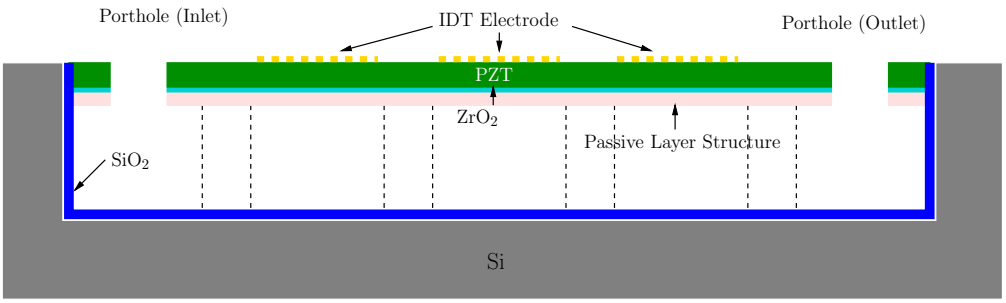

Figure 6.2. Cross–sectional view of a designed micropump structure.

Table 6.1. Layers in the MEMS pump structure.

layer	thickness
Cr/Au	100 Å/1200 Å
PZT	2.0 or 3.0 μm
ZrO_2 (diffusion barrier)	0.3 μm
LTO or ZrO_2/LTO (passive layer)	0.7 μm or 0.3 μm/0.7 μm
Sacrificial silicon[1]	3 or 4 μm
SiO_2	1.2[2] or 2.6[3] μm

[1] Sputtered silicon or low pressure chemical vapor deposition (LPCVD) polysilicon.
[2] Steam oxide grown at 1100 °C.
[3] Steam oxide grown at 1100 °C and annealed in a dry oxygen ambient at 1100 °C for 1 hour.

IDT Configurations The basis of the design for IDT electrodes was discussed in Chapter 5. Figure 6.3 shows two different IDT configurations used in the MEMS pumps. As observed in Chapter 5, diaphragm actuators with ring–shaped electrodes create sharply peaked deflection profiles, which potentially reduce the stroke volume and increase the dead volume. To mitigate this effect, the ring–shaped IDT electrodes (Type I) were modified to annular–ring–shaped IDT electrodes with solid electrodes at the center (Type II) to generate flatter bottoms. As described in Chapter 5, the electromechanically inactive region at the center of a diaphragm actuator generates flatter deflection profiles. At the same time, the center deflections are reduced. Thus, the ratio of the inactive circular region to the IDT electrode was set to 0.2, which reduces the center deflection by only about 10% (see Figure 5.40).

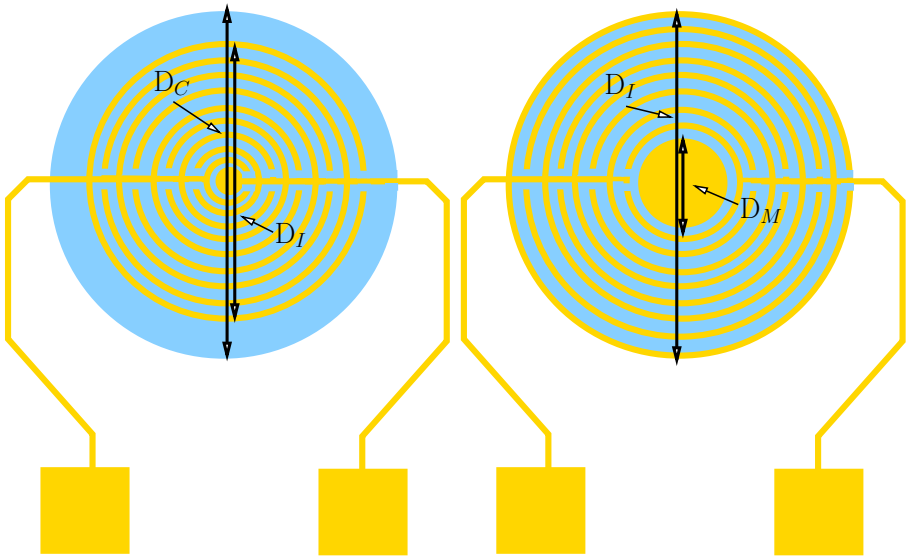

(a) Type I (b) Type II

Figure 6.3. (a) Ring–shaped IDT electrode and (b) annular–ring–shaped IDT electrode.

Summary of the Designs Details of the base structures and IDT configurations of design I and II are summarized in Tables 6.2 and 6.3.

6.1.3 Overview of Fabrication Process

The fabrication process of MEMS pumps had seven photo–mask steps [1]. The processes included one alignment mark transfer process from the front side of a wafer to the back side; this enabled alignment of the wafer after sacrificial silicon covered the front side alignment mark. The mask sets used in the fabrication are listed in Table 6.4. The process flow for the MEMS pump fabrication is described in Figures 6.4 and 6.5. First, alignment marks and base structures are defined on double side polished silicon wafers by a RIE process. The patterned wafers are then passivated with thermally grown silicon oxide. As a sacrificial material, silicon is deposited on the wafers. The field sacrificial silicon is then removed by a

[1] Photolithography mask sets were designed by Northrop Grumman Corporation.

Table 6.2. Parameters of pump structures for Design I.

Base structure – Parallel channel	
Diameter of Chamber (D_C)	750 or 450 μm
Depth	3 or 4 μm
Channel length (L_C)	200 μm
Channel width (W_C)	65 μm
IDT configuration – Type I	
Diameter of IDT electrode (D_I)	60–100% of the chamber diameter (D_C)
IDT width and spacing	7.5 μm

Table 6.3. Parameters of pump structures for Design II.

Base structure – Parallel channel	
Diameter of Chamber (D_C)	650 or 400 μm
Depth	3 or 4μm
Channel length (L_C)	240, 270 μm
Channel width (W_C)	100 μm
IDT configuration – Type II	
Diameter of IDT electrode (D_I)	2–3% larger than the chamber diameter (D_C)
Diameter of inactive metal circle (D_M)	20% of IDT diameter
IDT width and spacing	5 μm

RIE process and the remaining silicon layer is planarized by a chemical mechanical polishing (CMP) process. The passive layer (LTO or ZrO_2/ LTO), ZrO_2, PZT and Cr/Au layers are sequentially deposited. Portholes for XeF_2 gas access are formed at both ends of the pump structures. Finally, the structures are released by a XeF_2 process after the Cr/Au layer is patterned into IDT electrodes.

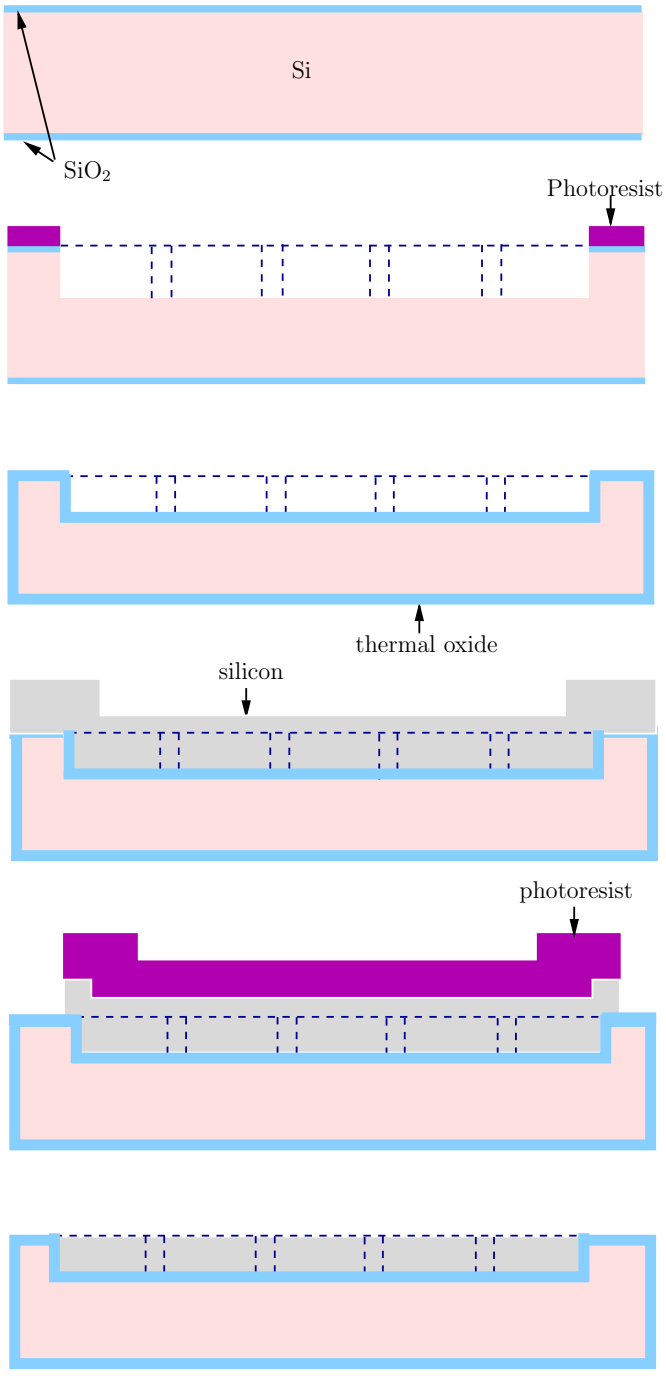

4 inch silicon wafer with 1500 $\mathring{A}$ thermally grown SiO_2 on both sides.

Alignment mark, chambers and channels were defined by RIE.

Chamber wells and channels were passivated with thermal silicon dioxide.

Amorphous (or poly) silicon was deposited.

Field silicon was removed by RIE.

Silicon in chambers and channels was planarized by RIE and CMP.

Figure 6.4. Fabrication process flow for MEMS pump structure.

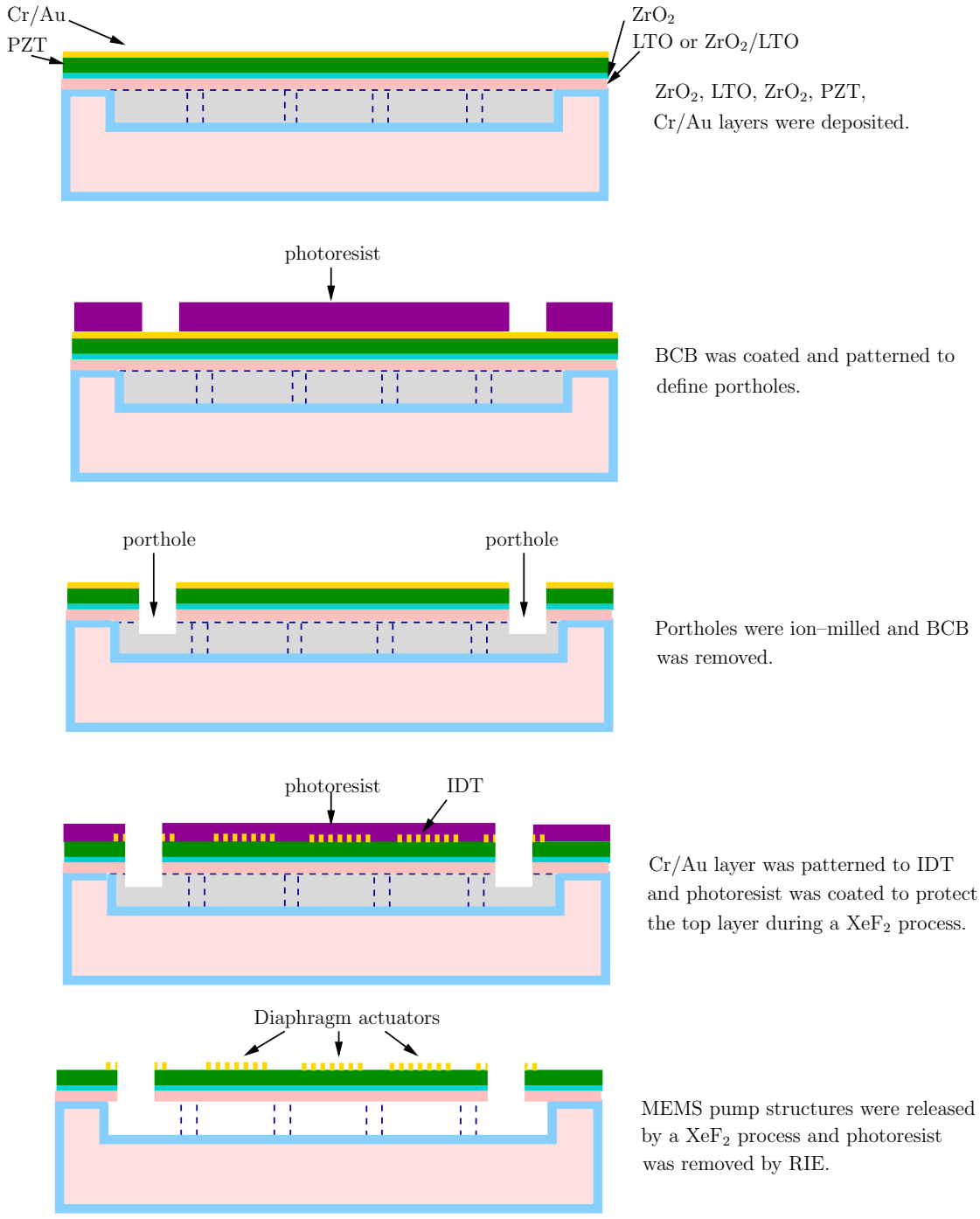

Figure 6.5. Fabrication process flow for MEMS pump structure.

Table 6.4. Photo–masks for MEMS pump fabrication.

Mask	Purpose
front–side alignment mark (FA)	transfer alignment–marks onto the front side
well etching (WE)	define chambers and channels
back–side alignment mark (BA)	transfer alignment–marks onto the back side from the front side and form scribe lines
field silicon removal (FS)	remove field silicon around pump structures
port–hole etching (PE)	define portholes on the ends of pump structures
top metal etching (ME)	define top electrode
protective–coating mask (PC)[1]	cover top layers (except port–holes) prior to XeF_2 release

[1] this mask and the port–hole etching mask are the same.

6.2 Processing Development and Fabrication of MEMS Pumps

Detailed processes in the MEMS pump fabrication are described in terms of the photolithography masks in Table 6.4. The ion-milling, backside aligning, and XeF_2 processes were performed at Northrop Grumman Corporation (Lithicum, MD). The other processes were performed at the Materials Research Laboratory and Nanofabrication Facility at the Pennsylvania State University.

6.2.1 Front–Side Alignment Mark and Well Etching: FA, WE Masks

Four–inch diameter double–side polished silicon wafers (100) with 1500 Å thick SiO_2 were used as substrates. First, alignment marks were patterned on the front sides of wafers using the FA mask. The alignment marks were formed on the front sides of the wafers using negative photoresist (NFR–012, JSR Microelectronics, Inc., Sunnyvale, CA) and a RIE process using a gas mixture of CF_4 and O_2 as summarized in Table 6.5. Using this RIE process, 1000–2000 Å deep alignment

marks were inscribed into the silicon. This was deep enough to see the alignment marks clearly after a passivation oxide was grown on the wafers. A Plasma Therm 720 RIE system (Plasma Therm, Inc., St. Petersburg, FL) was used for the RIE processes.

Table 6.5. Alignment–mark transfer processes.

Photolithography process – NFR–012	
dehydration	5 min on a hot plate at 115^{o}C
spin speed	4000 rpm
soft bake	90 sec on a hot plate at 115^{o}C
exposure	8 sec using 12 mW (g-line)
post–exposure bake[1]	120 sec on a hot plate at 115^{o}C
develop	1∼2 min, MF312[2]:DI = 1:1
hardbake	5 min on a hot plate at 115^{o}C
RIE process	
gas mixture	CF_4 – 45 sccm, O_2 – 5 sccm
power	200 W
pressure	50 mTorr
etch rate[3]	SiO_2– 600 Å/min, Si– 900 Å/min

[1] NFR–012 (JSR Microelectronics, Inc. Sunnyvale, CA) is a chemically amplified photoresist, which needs a post–exposure bake.
[2] MF312 is a developer from Shipley.
[3] The etch rate depends on etched area and condition of a RIE chamber well and the etched part was 6–7 % of the wafer.

Once the alignment marks were transferred, the base structures (chambers and channels) of the MEMS pumps were patterned. Using the same photoresist and RIE processes listed in Table 6.5, the 1500 Å thick SiO_2 on these structures was removed. The photoresist on the wafers was then stripped. With exposed silicon oxide as a mask, the pump structures were etched to a designed well depth (3–4 μm) by a RIE process using pure SF_6 (see Table 6.6). This RIE process was developed to have a high selectivity of over 30 for Si/ SiO_2. Well depths can be easily monitored during the RIE process because the silicon oxide had a limited etch rate. Deviations in the well depths were less than 10 % across a 4–inch wafer. After the remaining thermal oxide was stripped, the wafers were passivated by thermally grown silicon oxide. The passivation oxides were silicon dioxides grown with steam at 1100°C. Two different thicknesses of 1.2 or 2.6 μm were used. For 2.6 μm thick silicon oxide, an additional annealing at 1100° for 1 hour in an oxygen

ambient was carried out to reduce water content inside the oxide. Water can potentially react with XeF_2 and form hydrofluoric acid (HF), which is harmful to both silicon dioxide and PZT layers [3].

Table 6.6. RIE process to define chambers and channels in Si.

RIE process	
gas mixtures	SF_6 – 50 sccm
power	200 W
pressure	200 mTorr
etching rate	0.3–0.4 μm/min

6.2.2 Back–Side Alignment Mark and Silicon Filling: BA, FS Masks

The alignment marks on the front sides of the wafers were transferred to the back by an aligner with a bottom–side–alignment microscope (MA–6 mask aligner, Suss MicroTech, Munich, Germany). The sacrificial silicon was deposited by sputtering or low pressure chemical vapor deposition (LPCVD). Silicon deposited by sputtering was under a high compressive stress. Due to the high convex wafer curvature produced, it led to considerable difficulty in subsequent photolithography steps. To relax the stress, wafers with sputtered silicon were annealed at 700 °C for 5 min in a reducing atmosphere using a RTA. In the case of LPCVD silicon, silicon was deposited on both sides of the wafers at the same time. Therefore, the stress problem in the sputtered silicon can be avoided with the LPCVD silicon and no annealing step was used. Sputtered silicon was deposited at 4-7 mTorr (the process gas was argon) with a power of 400 Watts using a MRC 902 sputter deposition system. LPCVD silicon was deposited using silane (90–180 sccm) inside a process tube which was 212 cm long with an inner diameter of 22.5 cm. The deposition temperature and pressure were 620 °C and 400 mTorr. The deposition rate was 120 Å/min.

The field silicon around the pump structures was then removed by RIE using the FS mask. Figure 6.6 shows an image of the structure after the field silicon was removed. The remaining silicon was then planarized by CMP. The CMP process

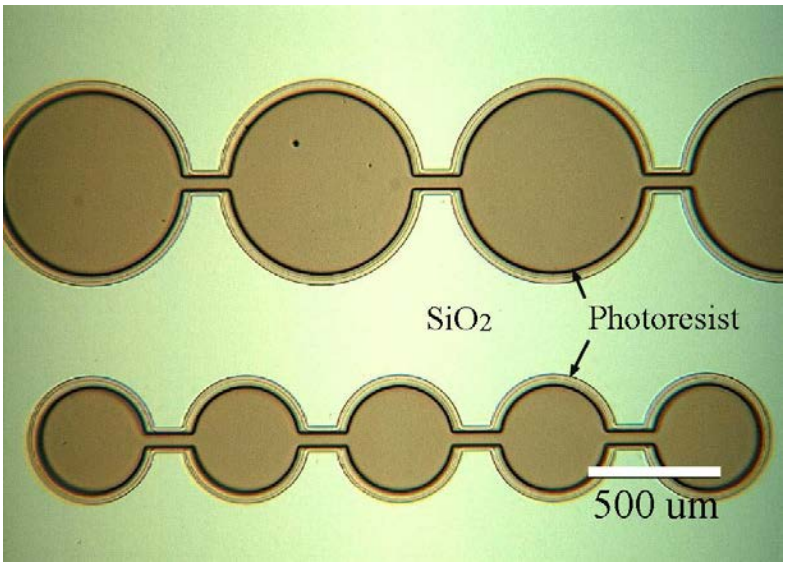

Figure 6.6. Optical picture of pump structures, the field silicon was removed using the FS mask; there is still photoresist on the wafer.

was conducted using Semi–Sperse P–1000 (Cabot Microelectronics, Corp., Aurora, IL), which is a slurry designed for polysilicon and shows high selectivity (> 300:1) to silicon dioxide. The slurry was mixed with DI water in a 3:2 ratio and the polishing rate was 2500–3400 Å/min. Figure 6.7 shows a vertical profile of the silicon on a pump structure after the CMP process. In unoptimized conditions, dishing and overhang were commonly observed. Dishing is a depression in the polysilicon filling the well caused by the polishing pad bending slightly into the recess during overpolishing [4]. Overhang is a high step around the pump structure. It was found that the overhang resulted from over–etching the silicon dioxide during the RIE removal of the field silicon, rather than the CMP process. Once a high step was formed in the SiO_2, it was difficult to remove by CMP without dishing, due to the high selectivity of P-1000 slurry for Si/ SiO_2. Severe dishing and overhang are problematic since diaphragm structures for MEMS pumps are formed directly on top of the sacrificial silicon. The structures will be distorted on the dished surfaces. After the CMP process, chamber wells generally showed 700–5000Å dishing.

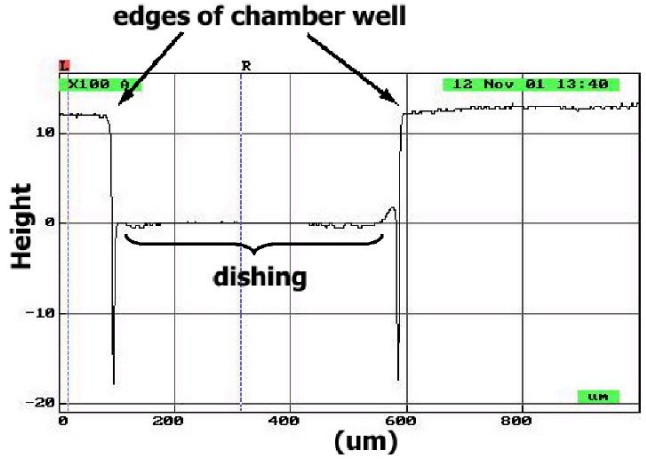

(a)

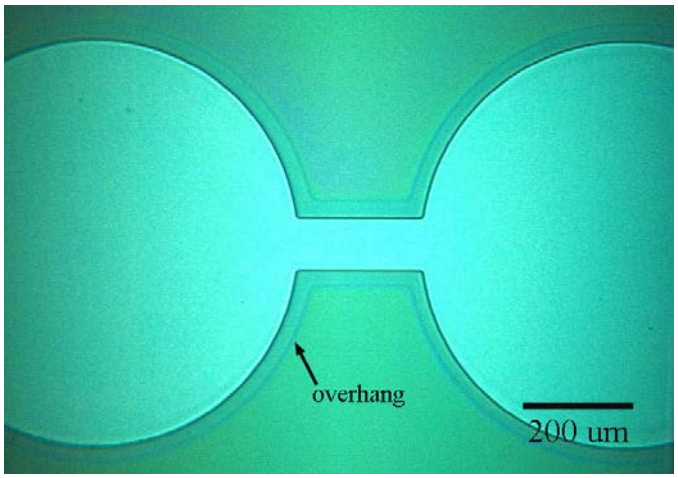

(b)

Figure 6.7. (a) Profilometry scan (showing dishing) of a chamber well and (b) optical picture of a pump structure after a chemical mechanical planarization (CMP) process.

After the CMP process, a passive layer (LTO or ZrO_2/LTO layer) was deposited. Typical deposition conditions for the LTO are summarized in Table 6.7. ZrO_2 and PZT layers were then deposited by methods described in Chapter 5. The thicknesses of the LTO, ZrO_2 and PZT layers were 0.7 μm, 0.3 μm and 2.0 or 3.0 μm, respectively. Cr/Au (100 Å/ 1500Å) layers were deposited using a sputtering system (Kurt J. Lesker, Clairton, PA). The Cr layer was grown by rf sputtering

Table 6.7. Process parameters for growth of LTO layer.

temperature	420 °C
pressure	300 mTorr
gas flow	SiH_4–52 sccm, O_2–90 sccm
thickness	0.7 μm

and the Au layer used dc sputtering. Both metal layers were deposited at 5 mTorr with a power of 200 Watts. The deposition rates of Cr and Au were 1.6 and 2.3 Å/sec, respectively.

6.2.3 Porthole Etching and Top–Metal Etching: PE, ME Masks

As seen in Figure 6.2, portholes were located at both ends of the pump structures and served as access holes for the XeF_2 gas while the pump structures were released. Both wet etching and ion-milling process were investigated for porthole definition.

PZT layers on platinized silicon wafers can be cleanly removed by a two step etch process [5]. In the first step, a 10:1 buffered oxide etch (BOE, which is 10 HN_4F: 1HF) is used to remove most of the PZT. A second etch in 2 HCl: $1H_2O$ solution for 30 seconds at an elevated temperature of 45 °C is used to remove the residue, which primarily consist of metal fluorides such as $Pb_{0.85}Zr_{0.15}F_{2.3}$ and Pb_5ZrF_{14}. However, for micropump structures, it was found that the etchant penetrated both PZT and ZrO_2 layers through the grain boundaries and attacked the LTO under these layers. When the LTO layer was etched, cracks formed in the PZT and zirconia layers due to by–products formed from the LTO and the etchant. Moreover, zirconia was not etched by the etchant. In addition, when the LTO was removed, the etchant also penetrated the sacrificial silicon and attacked the passivation oxide under the silicon, forming circular openings in the passivation oxide.

To avoid the above problems, an ion-milling process was investigated. Since ion–milling physically etches materials by ion–bombardment, the process can etch various chemically stable materials. However, at the same time, ion-milling usually presents a poor selectivity between the etching material and the masking layer. Thus, it is essential to use a proper masking layer. For this purpose, a process using Cyclotene^{TM} (BCB) (Dow chemical company, Midland, MI) was developed. Experimentally, it was found that BCB layers showed good resistance during ion-milling. Table 6.8 summarizes the BCB process.

Table 6.8. BCB layer as a mask for ion-milling.

BCB photolithography process	
adhesion promoter (AP3000)	3000 rpm for 40 sec
BCB coating	apply at 500 rpm and spin up at 1000 or 1500 rpm for 40 sec
soft bake	90 sec at 70 ^{o}C
exposure	8 sec using 12 mW (g-line)
post exposure bake	90 sec at 70 ^{o}C
develop (DS2100)	1 min
	apply developer and develop for 1 min
	spin up at 500 rpm and apply 3 pipet (3 ml) of developer to the wafer
	spin up at 2000–3000 rpm and dry the wafer
hard bake	1–3 hrs at 200 ^{o}C
Descum by RIE	
gas mixture	O_2–45 sccm, SF_6–5 sccm
DC	200 V
pressure	200 mTorr
etch time	1–3 min

The thickness of the BCB layers used was 5.0–6.0 μm. After the developing process, there was still some residual BCB in the opening, which required a descum [6]. In the descum process, a mixture of oxygen and fluorine rich plasma was used in order to remove the silicon content in the BCB resin. The BCB layers were then baked at 200°C for 2–3 hrs. In this condition, they are 70–80% cured [6]. The selectivity of the BCB to a stack of PZT/ZrO_2/LTO for a milling process was around 1. Therefore, a BCB layer slightly thicker than the stack of the pump structure is acceptable as a milling mask. The BCB layer was stripped by Nanostrip

(Cyantek, Inc., Fremont, CA). However, in this process, it was found that the BCB layer slightly reacted with PZT and left a white residue when it was removed by Nanostrip. This problem was solved by retaining the Cr/Au layer between the PZT and the BCB layers during ion-milling. The BCB could be removed without reaction from gold-coated surfaces. The Cr/Au layer was then patterned by standard photolithography and wet etch processes as summarized in Table 5.1. Figure 6.8 shows a port–hole after the ion-milling process. The remaining ZrO_2 layer resulted from an incomplete BCB descum. The problem was solved by increasing the descum time. The ion–milling in this study was conducted using a Nordiko 3000 (Nordiko, Inc., Havant, England). The tilting angle was 70°. Ion-milling parameters were optimized to obtain a milling rate of 0.16-0.18 μm per minute on a a stack of PZT/ZrO_2/LTO. When PZT/ZrO_2/LTO was completely removed, the color of the portholes was gray from the exposed sacrificial silicon.

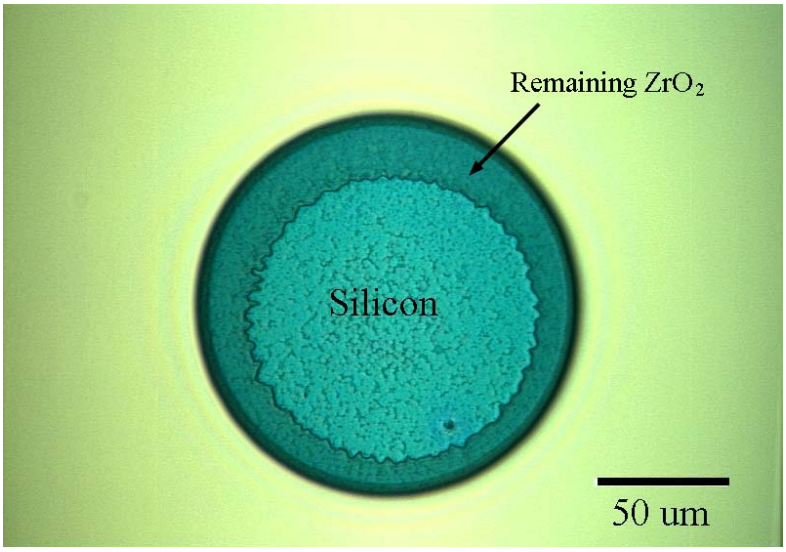

Figure 6.8. Porthole after ion–milling and IDT electrode patterning process, showing remaining ZrO_2.

6.2.4 Release Process: PC Mask

MEMS pump structures were covered with negative photoresist (NFR–012) to protect the PZT and Cr/Au electrodes. Similarly the wafer sides were protected

by painting on a thick layer of resist. Pump structures were then released using XeF_2. XeF_2 is a non–plasma, isotropic dry etchant of silicon [2]. XeF_2 is a white solid which sublimes at a pressure of 4 Torr at room temperature [3]. The etching process occurs by the following reaction:

$$2XeF_2 + Si \rightarrow 2Xe + SiF_4 \tag{6.1}$$

In this chemical reaction, silicon is the only solid. XeF_2 first adsorbs on the silicon surface and dissociates to form fluorine. Fluorine reacts with silicon to form gaseous SiF_4. The products and residual xenon are desorbed. Since there is no liquid present, this process does not cause any stiction commonly observed in released MEMS structures [7].

The XeF_2 process was conducted using a Xetch tool (Xactix, Inc., Pittsburgh, PA). A pulse etching scheme was used. First, XeF_2 gas was introduced into the expansion chamber from the source chamber. When the expansion chamber reached the designated pressure, the charge was stopped. XeF_2 gas in the expansion chamber was introduced into the etching chamber. The machine had two expansion chambers. After waiting for a specified certain duration time (15–25 seconds) for the etching reaction, the etching chamber was evacuated to around 10 mTorr to remove the byproducts. This cycle was repeated until the pump structures were released.

For a given amounts of sacrificial silicon (1.41–1.65$\times 10^{-3}$ cm^3) on the wafers, the volume etching rate per pump structure of sputtered silicon was around 210 μm^3/second and that of LPCVD silicon was $\sim$130 μm^3/second. The volume etch rate was calculated by dividing the amount of etched silicon per pump structure by the etching time (number of cycles $\times$ the duration time, for the etching reaction). Sputtered silicon showed a faster etching rate. It was noticed that attack of the edge or the backside of a wafer by XeF_2 gas slowed down the release process.

Tables 6.9 and 6.10 summarize the details of the stack on released pump structures.

The pump-1 wafer used LTO as the passive layer. The other wafers used ZrO_2/LTO as the passive layer. The protective zirconia under the LTO for pump-2, 4, and 5 wafers was annealed in a furnace at 700 °C for 2–3 hrs. The thickness of the passivation silicon oxide for the pump-1 and pump-2 wafers was 1.2 μm. The other wafers (pump-3, 4, and 5) used 2.6 μm thick passivation silicon oxide.

Table 6.9. Summary of released pump structures.

Wafer ID	Design	Sacrificial silicon	Large structure[1]	Small structure[2]
Pump-1	Design I	sputtered	Partial[3]	Full[4]
Pump-2	Design I	sputtered	No	Full
Pump-3	Design I	sputtered	Full	Full
Pump-4	Design II	LPCVD	Partial	Full
Pump-5	Design II	sputtered	Full	Full

[1] 750 μm in Design I and 650 μm in Design II.
[2] 450 μm in Design I and 400 μm in Design II. process.
[3] Some diaphragm actuators were released but pump structures were not released completely.
[4] Pump structures were released completely.

Table 6.10. Summary of layer structures of released pump structures.

Wafer ID	PZT (μm)	ZrO_2 (μm)	LTO (μm)	protective ZrO_2 (μm)	IDT width (μm)	IDT spacing (μm)
Pump-1	2.0	0.3	0.25[1]		7.5	7.5
Pump-2	2.0	0.3	0.7	0.2	7.5	7.5
Pump-3	2.0	0.3	0.7	0.3	7.5	7.5
Pump-4	3.0	0.3	0.7	0.3	3.5[2]	6.5
Pump-5	2.0	0.3	0.7	0.3	5	5

[1] Thickness of the LTO was reduced from 0.7 to 0.25 μm during the XeF_2 release step.
[1] The IDT electrodes were overetched.

6.3 Structural Characterization

Figure 6.9 shows the cross-section of a diaphragm from pump-1 (which used only LTO as the passive layer) after the small pump structures (450 μm in diameter) were completely released. The diaphragm was cross-sectioned using a focused ion beam.

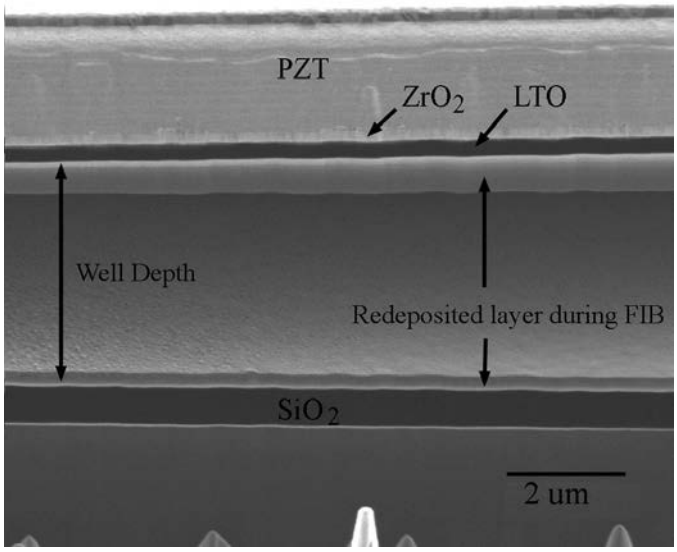

Figure 6.9. Cross–sectional view of a diaphragm from pump-1.

The thickness of the Cr/Au, PZT, ZrO_2, LTO, gap and SiO_2 (passivation oxide) are approximately 0.25, 2.0, 0.3, 0.25, 4.8 and 0.8 μm, respectively. The layers beneath the LTO and on top of the passivation oxide were re-deposited during the focused ion beam cutting. Considering the original thickness of LTO and passivation oxide, these oxide layers were obviously reduced during the XeF_2 release step. The thickness of the LTO was reduced from 0.7 μm to 0.25 μm. Since the LTO layer acts as the passive layer in the piezoelectric unimorph structure, the reduction will make the unimorph structure weaker. In addition, the passivation silicon oxide was etched from 1.2 μm to 0.6 μm. For the pump-1 and pump-2 wafers, the passivation silicon oxide was not thick enough to release the large pump structures completely. The passivation silicon oxides under the portholes punched through before these structures were completely released, so the release was stopped.

This problem was solved using a thicker passivation silicon oxide and a zirconia layer (under the LTO). It is known that XeF_2 reacts with water to form hydrofluoric acid [3]. Therefore, after the 2.6 μm thick passivation silicon oxide (steam oxide)

was grown at 1100 °C, the water content in the oxide was removed by annealing in a dry oxygen atmosphere at 1100 °C for 1 hour.

To protect the LTO layer from XeF_2, sputtered oxide, silicon oxynitride and zirconia layers were investigated as a protective layer against XeF_2. Among them, only zirconia layers didn't show measurable etching. Therefore, a 0.2–0.3 μm thick zirconia layer under the LTO was used as a protection layer.

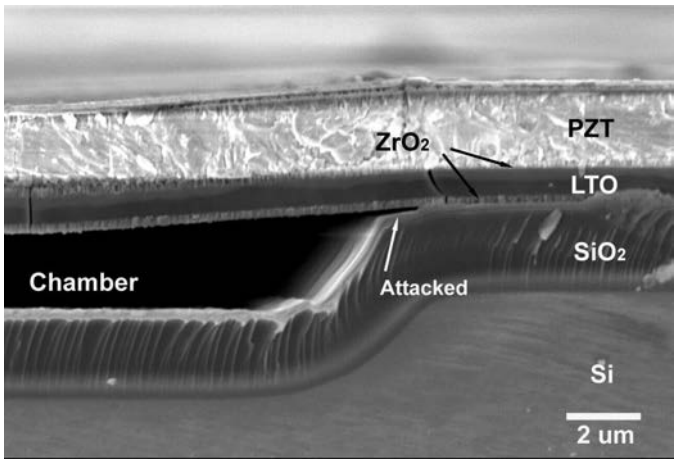

Figure 6.10. Part of a channel of pump structures (pump-3) which had a 2.6 μm thick passivation oxide and zirconia under the LTO. No attack of the passive layer was observed. The vertical cracks in the PZT and the LTO were artificially formed during cross-sectioning.

As seen in Figure 6.10, the zirconia layer acted well as a protective layer. When a thinner (less than 0.14 μm) zirconia layer was used, it was found that XeF_2 penetrated the thin zirconia layer and attacked the LTO and formed pores in the layer. With these modifications in passivation and LTO layers, large pump structures (pump-3 and pump-5) could be completely released. Reduction of the passivation oxide thickness was less than 0.2 μm, indicating that the additional annealing in an oxygen ambient made the passivation oxide more resistant against XeF_2.

For the pump-4 wafer, it was difficult to release large pump structures since XeF_2 attacked the edge and top surface of the wafer. In addition, LPCVD silicon, which was used as the sacrificial material, showed more resistance to XeF_2 etching than

the sputtered silicon.

Even though the zirconia layer provided good protection for the LTO, the interface between the protective zirconia and the passivation oxide was attacked, which potentially made clamping at the boundaries of released pump structures (at the boundaries) poor. Figures 6.11 shows completely released pump structures of Design I and II.

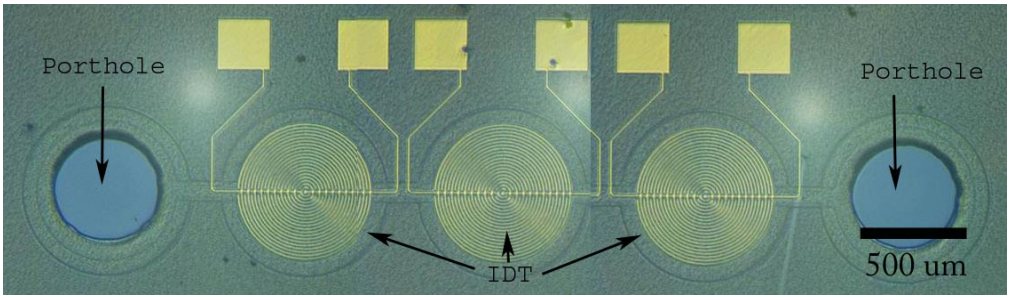

(a)

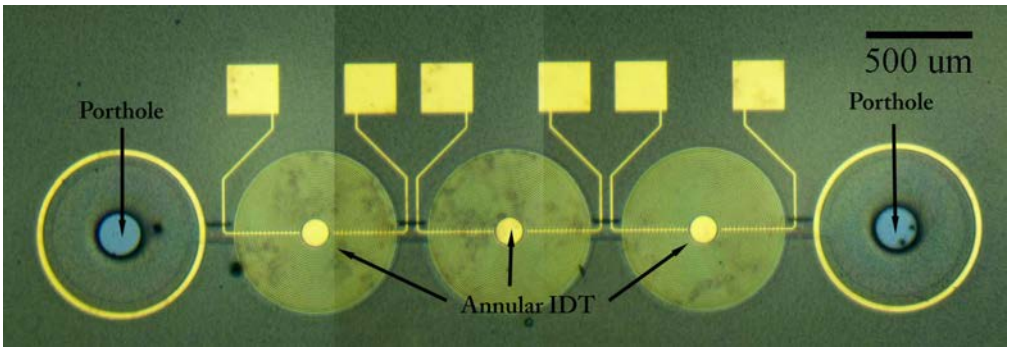

(b)

Figure 6.11. Completely released pump structures of (a) Design I and (b) Design II.

6.4 Electrical Characterization of Ferroelectric Layers

The dielectric and ferroelectric properties of the PZT layers in released pump structures were measured to verify that the fabrication process did not degrade their characteristics. The PZT layers were evaluated by measurements described in Chapter 5. The electrical properties of PZT layers in the pump structures did not show any obvious changes before and after pump structures were released. The remanent polarizations were 20–22 μm/cm^2 and coercive fields were around 50 kV/cm (see Figure 6.12). The polarizations and electric fields were calculated by the same method discussed in section 5.4.3. The dielectric losses were less than 0.02 at 10 kHz.

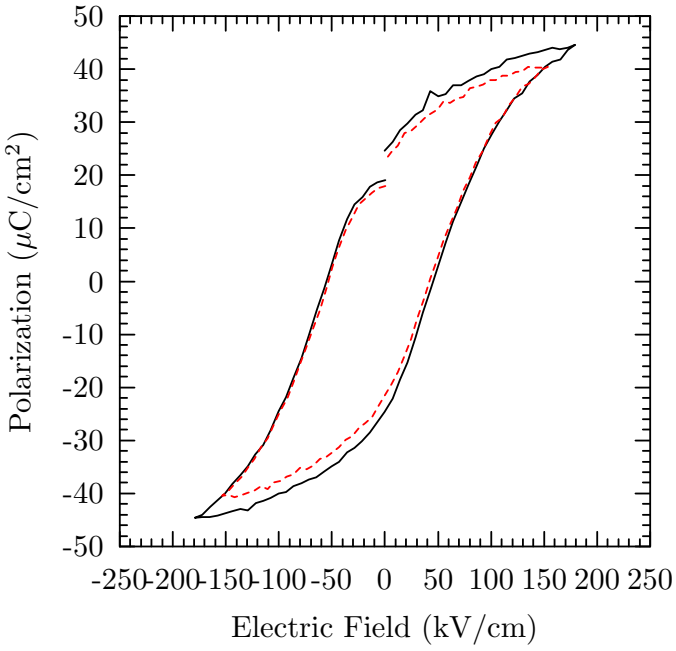

Figure 6.12. Hysteresis loops of a released 650 μm IDT diaphragm in design II.

6.5 Vibration Characteristics

Residual stresses in diaphragm actuators are important in understanding their mechanical behavior. Unlike diaphragm actuators (Chapter 5), it was difficult to make load–deflection measurements to evaluate the residual stresses since a differential pressure should be applied to the inlet and outlet in a pump structure. Therefore, the resonance method (see Section 5.5) was used. Assuming the LTO layer behaves like thermal oxide in Chapter 4, the expected residual stresses in diaphragms in the pump-4 wafer (with 3.0 μm thick PZT) are in the range of 76 to 93 MPa. Using Equation 5.6, the 1^{st} expected resonance frequency should be between 128 and 147 kHz for large diaphragms (650 μm in diameter) in the pump-4 wafer. However, the measured resonance frequencies at 1 atm was around 235 kHz. This value is much higher compared to the expected value.

This discrepancy can be at least partially explained by the squeezed film effect [8]. When a MEMS structure is oscillating in a confined space such as a chamber well, air under the structure is squeezed and behaves like a spring element, which increases the resonance frequencies. This effect is proportional to the size of the MEMS structures and the ambient pressure. Therefore, to eliminate this effect, the resonance frequencies were measured at a lower pressure of 5 Torr. As seen in Figure 6.13, the resonance frequencies shift to lower frequencies. This is in contrast to the behavior of diaphragm actuators (Chapter 5) at low pressures. The resonance frequencies of these diaphragm actuators shifted to higher values with decreasing ambient pressure. It was mainly due to the decrease in the mass–loading by air. In the diaphragm actuators, the squeezed film effect is minimal since these structures had large cavities underneath them. However, for the diaphragms in the pump structures, the increase in the spring constant due to the squeeze film effect dominates over the mass–loading effect.

Table 6.11 summarizes the expected and measured resonance frequencies. With decreasing ambient pressure, the measured values approaches the expected values.

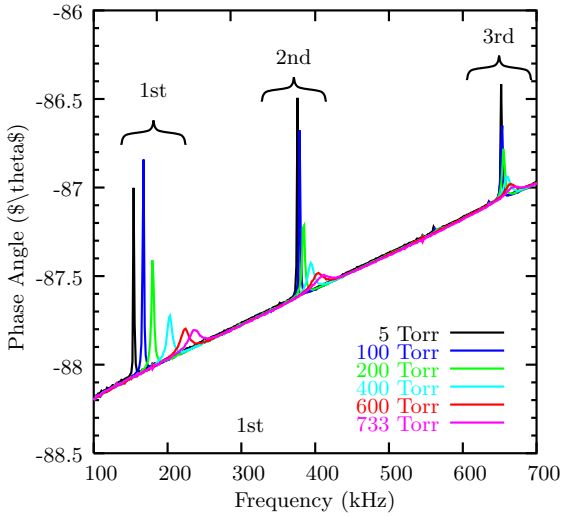

Figure 6.13. Resonance frequencies of 650 μm diaphragm actuator (pump-4) at ambient pressures from 733 Torr to 5 Torr.

This means that the stress development in the diaphragm layers in pump structures is not that different from that of the diaphragm actuators in Chapter 5.

Table 6.11. Resonance frequencies of released pump structures.

Wafer ID	1^{st} resonance (kHz)	2^{nd} resonance (kHz)	3^{rd} resonance (kHz)
Theoretical[1]	128–147	285–338	461–529
733 Torr	235	412	674
5 Torr	154	374	652

[1] calculated by Equation 5.6 using the theoretical vibration constants.

Dynamic Vibration The MEMS pump structures are intended to be operated off–resonance. Diaphragms of 650 μm in diameter showed the 1^{st} resonance at around 150 kHz. However, the pump structures will be operated at less than tens of kHz since the fluid in the chambers cannot follow higher operation frequencies. Therefore, it is important to know the vibration profiles when a diaphragm is operated off-resonance. Figure 6.14 shows the vibration profile of a diaphragm operated at 500 Hz. As seen in this figure, the vibration profile is like the electrically-induced deflection profile, which has a sharp bottom (not like the vibration profile of the 1^{st} resonance mode). The up-stroke of the diaphragm is attributed to inertia (see Figure 6.14(b)). It was also observed that the amplitudes of dynamic vibration of

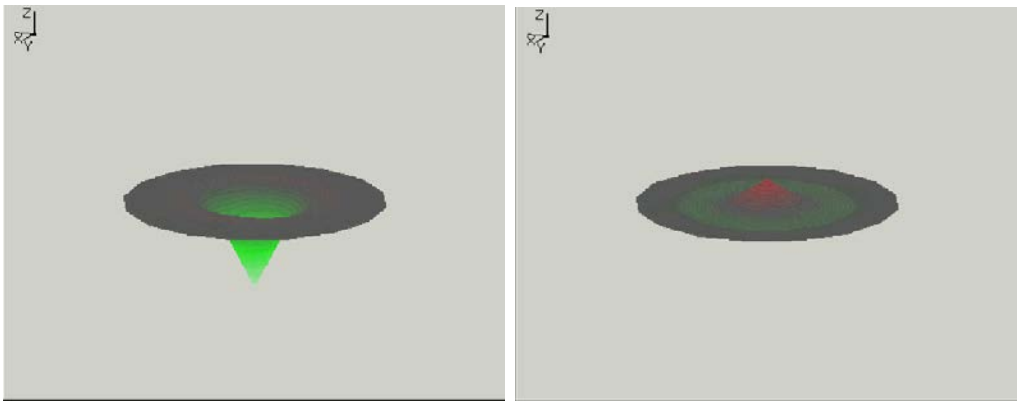

(a) (b)

Figure 6.14. Vibration profile of a 750 μm diaphragm actuator (pump-1) driven at 500 Hz with 60 V. (a) up-stroke and (b) down-stroke.

diaphragm in a pump structure were maintained to the same value up to 5 kHz and dropped to half of the value above 10 kHz. It is expected that when a diaphragm is vibrating at a high frequency, movement of air under the diaphragm through the channels (which are connected to the chambers) can not follow the motion of the diaphragm and hence damps the motion of the diaphragm. Therefore, it is important to optimize the dimensions of the channels to operate a pump structure at higher frequencies.

6.6 Electrically Induced Deflections

The electrically–induced deflections of diaphragm actuators in pump structures are important in their operation. As described in the finite element results in Chapter 5, center deflections are proportional to the ratio of the IDT to the diaphragm diameter for a given voltage (see Figure 5.37). Figure 6.16 shows that center deflections are increasing with the ratio of the IDT to the diaphragm (from the pump-2 wafers).

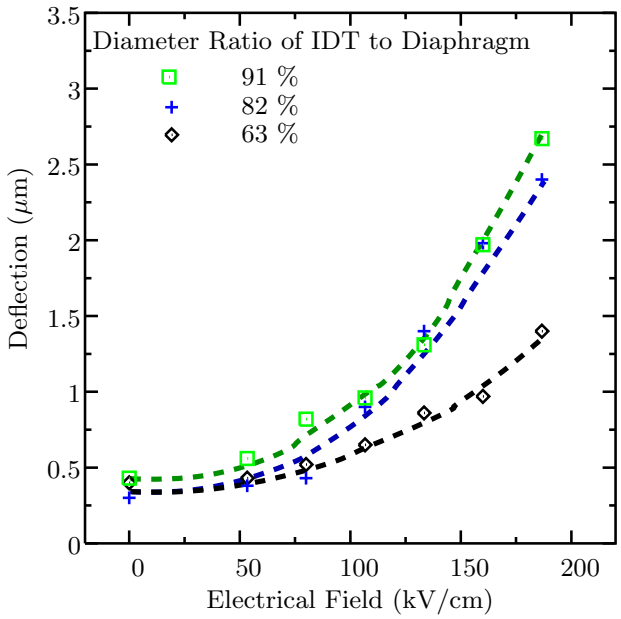

Figure 6.15. Deflections of a 460 μm diaphragm depending of the diameter ratio of the IDT to the diaphragm (from the pump-2 wafer).

Large pump structures in the pump-3 and pump-5 wafers were completely released. However, these pump structures had to be heated to 150 °C for 10-30 min to obtain reasonable deflections. These wafers were exposed to XeF_2 gas for long times (around 7 hours) to release the large pump structures. Therefore, as seen in Figure 6.10, the possibility to attack the interface between the LTO and the passivation oxide was high. The electrically-induced deflections of these pump structures are expected to be reduced due to the adhesion problem between the first zirconia and the passivation oxide. When strain is induced in these diaphragms, some portion of the strain can be relaxed at the boundary and doesn't contribute to the deflections. After the structures were heated at 150 °C for 10-30 min, the deflections were restored to values similar to those of well clamped diaphragms. The mechanism for the restoration is not clear at this point. This effect was temporary and completely diminishes over a span of 12 hours.

For the pump-1, pump-2 and pump-5 wafers, heating didn't have a significant effect on the deflections since the pump structures showed fair clamping conditions. Table 6.12 summarizes the electrically-induced deflections of released pump structures.

Table 6.12. Summary of layer structures of released pump structures.

Wafer ID	Deflection (μm) at 120 V			
	No heating		Heating[1]	
	Large diaphragm[2]	Small diaphragm[3]	Large diaphragm[2]	Small diaphragm[3]
Pump-1	–	1.5–2.2	–	–
Pump-2	–	0.7–2.0	–	–
Pump-3	0.7	0.5	1.6	1.0-
Pump-4	2.0[4]	1.3[5]	–	–
Pump-5	0.6	0.4	3.1[6]	3.5

[1] The samples were heated at 150 °C for 10–30 min.
[2] 750 μm in Design I and 650 μm in Design II.
[3] 450 μm in Design I and 400 μm in Design II. process.
[4] The diaphragm touched the bottom of the chamber at 140 V.
[5] The diaphragm touched the bottom of the chamber at 160 V.
[6] The diaphragm touched the bottom of the chamber at 80 V.

In addition, a difference in the deflection profiles of diaphragms with ring-shaped IDT electrodes and annular IDT electrodes was observed (see Figure 6.16). As discussed in Chapter 5, annular ring–shaped IDT electrodes created flatter bottoms when compared to ring–shaped IDT electrodes.

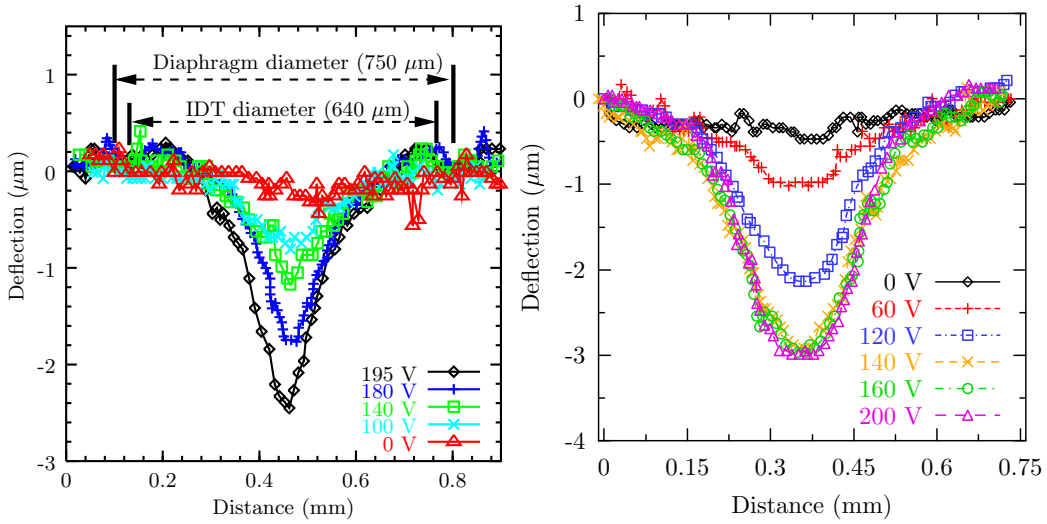

Figure 6.16. Deflections of a (a) 750 μm diaphragm with ring-shaped IDT electrodes (from the pump-3) and (b) 650 μm diaphragm with annular shaped IDT electrodes (from pump-4).

Assuming that the diaphragm actuators touch the bottom of the chamber, the stroke volumes can be calculated by integrating the areas above the deflection profiles in Figure 6.16. The compression ratios (the stroke volume per the chamber volume) were calculated to be around 0.2 for the diaphragm actuator with ring-shaped IDT electrodes and 0.4 for the diaphragm actuator with annular shaped IDT electrodes. Thus, the increase in the compression ratio using the annular-ring shaped IDT electrode was about 100 %. Figure 6.17 shows the expected volume displacements of the pump structures using 650μm diameter diaphragm actuators with annular shaped IDT electrodes. The volume displacements were calculated using Equation 3.4. To obtain reasonable volume displacements, the ratio of reverse flowing volume to the stroke volume should be minimized.

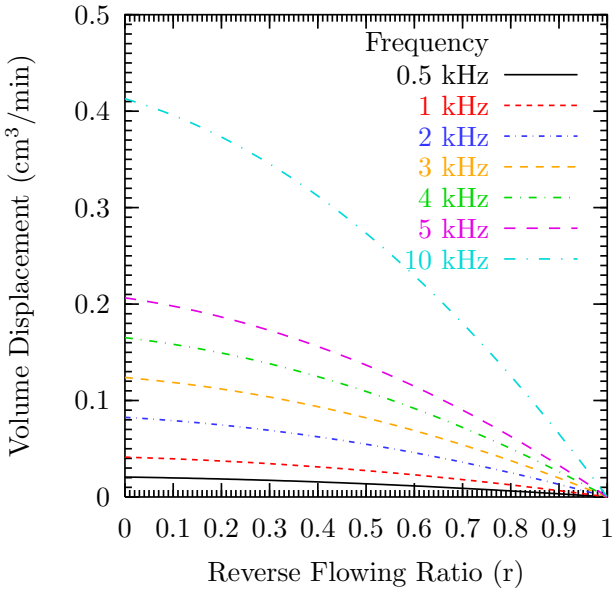

Figure 6.17. Expected volume displacement of a large pump structure (from pump-5) as a function of the operation frequency and the ratio of reverse flowing volume to the stroke volume.

6.7 Performances of MEMS Pumps

Measurement Set–up To operate three–stage pump structures, a sequential pulse train was applied to the three diaphragm actuators. A computer with an 8 channel analog output board (PCI-6731, National Instruments, Austin, Texas) was utilized. Voltage output from the analog output board was 5 V and was amplified up to 300 V using a four channel voltage amplifier built in-house. A program written in Labview 6.1 (National Instruments, Austin, Texas) software was used to control the pulse outputs. Figure 6.18 shows the user interface for the pulse generation program[2]. The program could control the pump frequency, the amplitudes of the output voltage, and states of the diaphragms (open or closed).

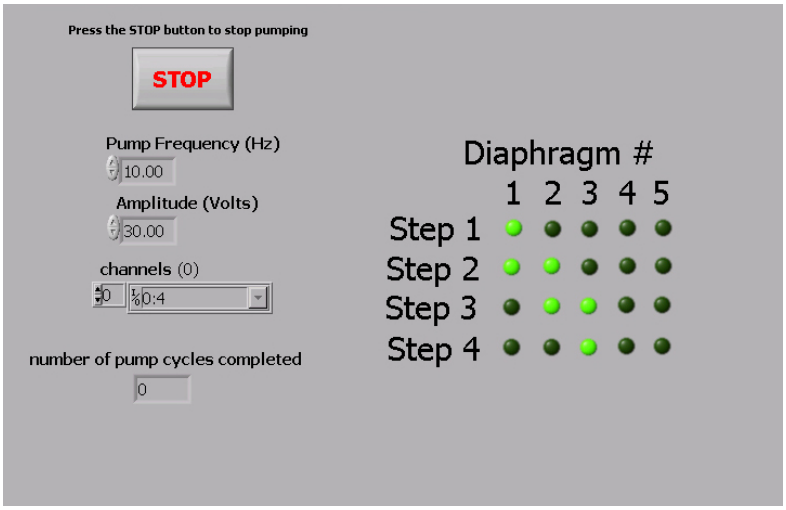

Figure 6.18. Front panel of the pulse generation program.

To check pumping of fluid, the pump structures were mounted on a ceramic package. A steel needle (500–900 μm in diameter) with a plastic tubing was connected to the inlet of the pump structure. The needle was connected to the inlet using a manipulater under a microscope. The joint between the needle and the inlet was sealed by glue (extra fast setting epoxy by Harcros Chemicals Inc., NJ or vacuum epoxy by Kurt J. Lesker Co., Pittsburgh, PA). The other end of the tubing attached to the steel needle can be connected to a pressure transducer or a capillary

[2]The program was provided by Northrop Grumman Corporation.

tube.

Performance of Pump Structures For a completely released pump structure (650 μm in diameter from pump-5), a pulse was applied to demonstrate sequential motion of the three diaphragm actuators. First, the pump structure was heated to 150 °C for 30 min to enhance the electrically-induced deflection. 150 V at 1 Hz was applied to the structure. The low operation frequency was selected to capture the sequential motion easily by a CCD camera (DCM2, Polaroid Corporation, Waltham, MA). Figure 6.19 clearly shows the sequential motion. The diaphragm with a voltage applied flexed downward.

In addition, a pump structure (650 μm in diameter from pump-5) was used to demonstrate pumping of fluid. The structure was filled with diffusion pump oil (Dow Corning 702) through the tubing connected to the inlet of the pump structure. When the pump structure was operated, bleeding of the fluid in the outlet was observed. However, no fluid flow at the outlet was observed. This is thought to be due to the inability of the pump (small stroke volume) to overcome the surface tension of the fluid (30 dynes/cm[3]). This problem may be solved using a proper surfactant. Pump structures have not generated meaningful results in pumping air. The reason might lie in the small stroke volume and significant reverse flow. Therefore, the volume displacement was below the measurement range of the setup. Since the diaphragm actuators only made point contact at the bottom of the chamber, the reverse and foward flow may be almost same. When the diaphragm touched the bottom of the chamber, higher applied electric fields did not make the diaphragm more flat (at the bottom), however, it raised the periphery of the diaphragm (see Figure 6.16 (b)). This behavior is due to the fact that the stress induced by ring-shaped (even annular–shaped) IDT electrodes is concentrated at the center of the diaphragm thus increasing its stiffness.

[3]Product information sheet from Dow Corning for Dow Corning 702 diffusion pump fluid

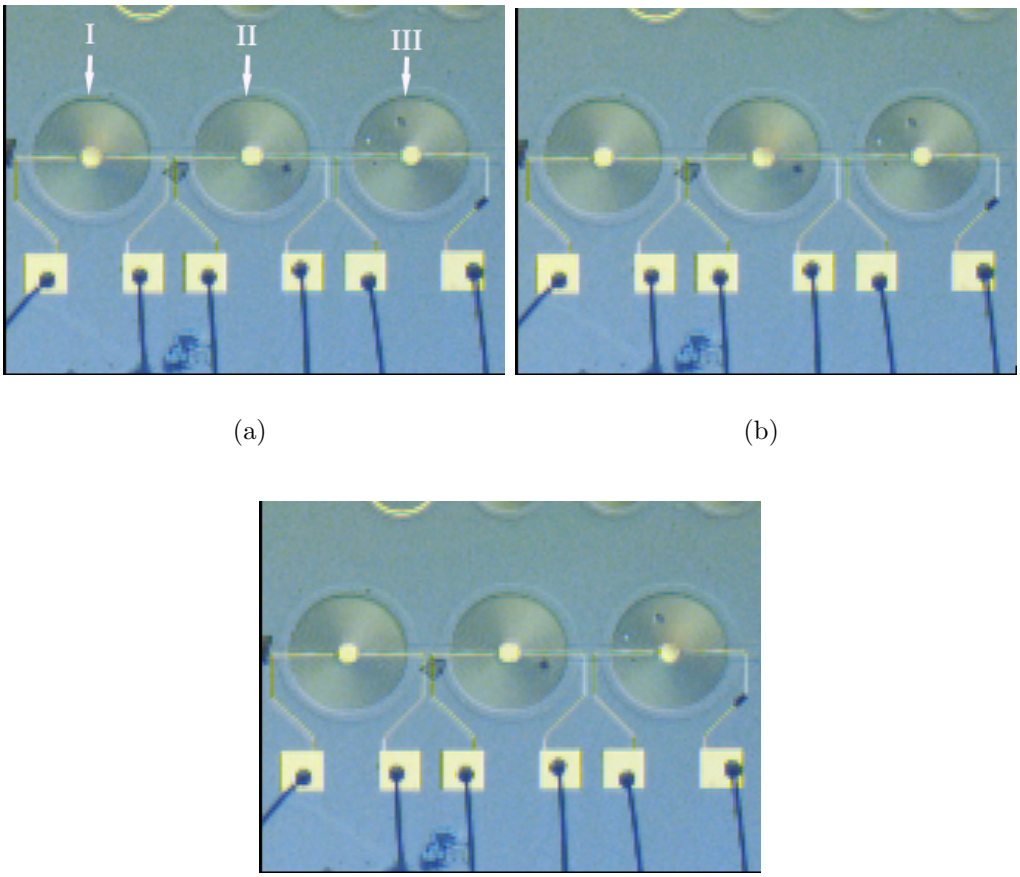

Figure 6.19. Sequential motion of a three stage pump structures (from pump-3). (a) time 1: Diaphragm I flexes down, (b) time 2: Diaphragm II flexes down, (c) time 3: Diaphragm III flexes down

6.8 Conclusions

MEMS pump structures were fabricated by surface micromachining. The sacrificial material was silicon and the pump structures were released by XeF_2. The fabrication process had seven photo–mask steps. First, the base micropump structures was defined and then a passivation oxide (the etch stop layer during the XeF_2 release process) was grown. These wells were filled with silicon and planarized by CMP. Layers for the diaphragm actuators (LTO/ ZrO_2/ PZT/ Cr/Au) were

then deposited. Portholes were defined by ion milling. The Cr/Au layer was then patterned. Using an ion-milling process, 3–4 μm thick diaphragm layers were removed from the portholes. Therefore, a rigid mask layer was required. It was found that Cyclotene^{TM} (BCB) resin could be used as the masking layer. In addition, to protect the LTO layer during release, a zirconia layer was used. The zirconia layer did not show any etching by XeF_2. Piezoelectric layers in released pump structures did not degrade during the fabrication process. During the release step, the boundaries of diaphragm actuator was attacked, resulting in poor clamping. From these diaphragm actuators, deflections large enough to touch the bottom of the chambers could not be obtained. However, well–clamped diaphragm actuators touched the bottoms (3–4 μm deep) at voltages of 80 V to 140 V for 650 μm diameter diaphragms. A sequential deflection of a three stage pump structure was demonstrated. The surface micromachined peristaltic pumps using lead zirconate titanate films has potential as a pumping system for a mass spectrometer system on a chip.

References

[1] C.B. Freidhoff, R.M. Young, S. Sriram, T.T. Braggins, T.W. O'Keefe, J.D. Adam, H.C. Nathanson, R.R.A. Syms, T.J. Tate, M.M. Ahmad, S. Taylor, and J. Tunstall, "Chemical Sensing using Nonoptical Microelectromechanical Systems," *J. Vac. Sci. Technol. A*, vol. 17, no. 4, pp. 2300–2307, 1999.

[2] G. Kovacs, *Micromachined Transducers – Sourcebook*. WCB McGraw Hill, New York, 1998.

[3] P.B. Chu, J.T. Chen, R. Yeh, G. Lin, J.C.P. Huang, B.A. Warneke, and K.S.J. Pister, "Controlled Pulse–Etching with Xenon Difluoride," *in Proceedings of the 1997 International Conference on Solid–State Sensors and Actuators, Chicago, IL, June 16–19*, pp. 665–668, 1997.

[4] G. Fu and A. Chandra, "An Analytic Dishing and Step Height Reduction Model for Chemical Mechanical Planarization (CMP)," *IEEE Transactions on Semiconductor Manufacturing*, vol. 16, no. 3, pp. 477–485, 2003.

[5] L.-P. Wang, "Microelectromechanical Systems (MEMS) Sensors Based on Lead Zirconate Titanate (PZT) Films," PhD thesis, The Pennsylvania State University, 2001.

[6] M. Dow Chemical Company, Midland, *Processing Procedures for CYCLOTENE 4000 Series Resin (Puddle Develop)*.

[7] R. Legtenberg, J. Elders, and M. Elwenspoek, "Stiction of Surface Microstructures after Rinsing and Drying: Model and Investigation of Adhesion Mechanisms," *in Proceedings of the 7^{th} International Conference on Solid–State Sensors and Actuators (Transducers '93)*, pp. 193–201, 1993.

[8] T. Veijola, H. Kuisma, J. Lahdenpera, and T. Ryhanen, "Equivalent-Circuit Model of the Squeezed Gas Film in a Silicon Accelerometer," *Sens. Actuators A*, vol. 48, pp. 239–248, 1995.

Chapter 7

Conclusions

In this thesis, peristaltic pump structures using PZT films were fabricated by surface micromachining. This work has demonstrated that compact pump structures of less than $5 \times 1 \times 0.5$ mm in dimension could be formed on silicon wafers without additional assembly steps, presenting a potential for micromachined pumping systems in MEMS mass spectrometer systems. In addition, piezoelectric diaphragm actuators were designed and verified to generate vertical deflections up to several micrometers. Considering basic bending mechanics, it was found that common d_{31} mode diaphragm actuators could not generate deflections larger than the diaphragm thickness. To overcome this problem, piezoelectric diaphragm actuators with ring–shaped IDT electrodes were proposed. Based on design of micropumps and piezoelectric diaphragm actuators, this study entailed three parts.

Processing and Characterization of Zirconia and PZT Films For diaphragm actuators and micropump structures, a sol-gel process to deposit crack–free 1.6–3.0 μm thick PZT films on 4–inch silicon wafers with thermal oxide was developed. To prevent Pb–diffusion, which causes cracking of PZT films on SiO_2, zirconia was selected as the buffer layer. It was found that the zirconia films should

be thicker than 0.2 μm and needed to be annealed at 700°C for more than 2 hours to serve effectively as buffer layers. A cross-sectional view of these layers showed sharp interfaces, indicating no significant reactions. PZT films deposited on top of zirconia buffer layers showed good dielectric and ferroelectric properties. The standard deviation in the thickness of 1.2 μm thick PZT film across a 4–inch wafer was 3%. Residual stresses of PZT, ZrO_2, SiO_2 were found to be 100–150, 230–270, and -147 MPa in the final stacks. The average stresses of 1.6 μm PZT/0.3 μ ZrO_2/ 0.5 μm SiO_2 stacks were ∼80 MPa.

Micromachined Diaphragm Actuators Piezoelectric diaphragm actuators were fabricated by bulk micromachining that diaphragm actuators driven with ring–shaped IDT electrodes generate large deflections. Sol–gel PZT films were deposited on top of thermally grown silicon oxide with zirconia buffer layers. PZT films in diaphragm actuators showed good dielectric and ferroelectric properties. The relative dielectric constants of the PZT films were calculated to be around 660 and the dielectric losses were below 2 % at 10 kHz. The remanent polarizations and coercive fields were 20 μC/cm^2 and 50 kV/cm, respectively. From resonance measurements on diaphragm actuators, it was known that the diaphragm actuators behaved as membranes. Therefore, residual stresses are important to explain the structural and vibrational mechanics for diaphragm actuators. From load–deflection measurements, the average residual stresses were found to be around 86 MPa and the net Young's modulus was 66 GPa. The resonance characteristics were evaluated to understand the behavior of the diaphragm actuators depending on excitation method, bias voltage, and ambient pressure. The resonance frequencies were identical to within 2 % for electrical and mechanical excitation. However, in the mechanical excitation, both symmetric and asymmetric modes were excited. Electrical excitation generates dominantly symmetrical modes due to the axisymmetric IDT structures. The quality factor of diaphragm actuators was 250 at 727 Torr and increased to 2100 below 1 Torr ambient pressure. When a forward bias was applied to a diaphragm actuator, the tensile stress of the diaphragm decreased due to the ring-shaped IDT configuration. Under a reverse bias, the tensile stress increased. However, because of repoling under a reverse bias greater than the co-

ercive voltage, the stress generated was limited to 8 MPa. For this reason, the diaphragm actuators always flexed downward to obtain a significant deflection of more than 1 μm. Shifts of the resonance peak depending on poling conditions imply motion of non–180° domain walls. However, non–180° domain wall motion of the PZT layer in diaphragm actuators was limited. Diaphragm actuators of less than 1 mm in diameter could generate electrically induced deflections of larger than 5 μm at the center at moderate voltages of around 100 V. In addition, deflection profiles of diaphragm actuators could be modified using ring–shaped IDT electrodes with inactive circular regions at the center.

MEMS Piezoelectric Peristaltic Pumps MEMS pumps were fabricated by surface micromachining. The sacrificial material was silicon and the pump structures were released by XeF_2 to avoid stiction. The fabrication process had seven photo–mask steps. First, the base micropump structures was defined and a passivation oxide (the etch stop layer during the XeF_2 release process) was then grown. These wells were filled with silicon and planarized by CMP. Layers for the diaphragm actuators (LTO/ ZrO_2/ PZT/ Cr/Au) were then deposited. Portholes were defined by ion milling. The Cr/Au layer was then patterned. Using an ion-milling process, 3–5 μm thick diaphragm layers were removed from the portholes. Therefore, a rigid mask layer was required. It was found that Cyclotene^{TM} (BCB) resin could be used as the masking layer. In addition, to protect the LTO layer during release, a zirconia layer was used. The zirconia layer did not show any etching by XeF_2. Piezoelectric layers in released pump structures were not degraded through the fabrication process. Partial oxidation of sacrificial silicon in the wells during the processes increased the times required to release pump structures completely, which led to attack of the boundaries of diaphragm actuators in pump structures. Thus, some released pump structures were poorly clamped at the boundaries. From these diaphragm actuators, deflections large enough to touch the bottom of the chambers could not be obtained. However, well–clamped diaphragm actuators touched the bottoms (3–4 μm deep) at voltages of 100 V to 140 V for 650 μm diameter diaphragms. Sequential deflection of a three stage pump structure was demonstrated. The surface micromachined peristaltic pumps

using lead zirconate titanate films have a potential as pumping systems for a mass spectrometer system on a chip.

Appendix A

Vibration of Circular Diaphragms

Vibration of a circular diaphragm can be described by either a plate or a membrane theory. When a diaphragm behaves like a plate, the restoring force is provided by the elasticity of the diaphragm during its vibration. In case of a membrane, which theoretically does not have a stiffness, membrane tension creates the restoring force. The basic equations of transverse vibration of a circular membrane and plate are reviewed here, based on the discussion in Meirovitch's *Principles and Techniques of Vibration* [1].

A.0.1 Circular Membrane

Transverse vibration of a circular membrane of diameter a, is expressed by the following equations in cylindrical coordinates

$$\nabla^2 W(r,\theta) + \beta^2 W(r,\theta) = 0 \tag{A.1}$$

$$\beta^2 = \frac{\rho\omega^2}{T} \tag{A.2}$$

where W is the transverse displacement, ρ and ω are the density of the membrane and the angular frequency of vibration, and T is the membrane tension. Using the Laplacian in polar coordinates and assuming a solution of the form

$$W(r,\theta) = R(r)\Theta(\theta) \tag{A.3}$$

The following differential equation is obtained.

$$\left(\frac{d^2R}{dr^2} + \frac{1}{r}\frac{dR}{dr}\right)\Theta + \frac{R}{r^2}\frac{d^2\Theta}{d\theta^2} + \beta^2 R\Theta = 0 \tag{A.4}$$

With separation of variables, the above equation reduces to the following equations.

$$\frac{d^2\Theta}{d\theta^2} + m^2\Theta = 0 \tag{A.5}$$

$$\frac{d^2R}{dr^2} + \frac{1}{r}\frac{dR}{dr} + \left(\beta^2 - \frac{m^2}{r^2}\right) = 0 \tag{A.6}$$

where, the constant m^2 is positive. The solutions for Equation A.5 and A.6 can be represented as follows:

$$\Theta_m(\theta) = C_{1m}\sin(m\theta) + C_{2m}\cos(m\theta), \qquad m = 0, 1, 2, ... \tag{A.7}$$

$$R_m(r) = C_{3m}J_m(\beta r) + C_{4m}Y_m(\beta r), \qquad m = 0, 1, 2, ... \tag{A.8}$$

where, $J_m\ (\beta r)$ and $Y_m\ (\beta r)$ are Bessel functions of order m and of the first and second kind, respectively. Therefore, the general solution can be written in the form

$$\begin{aligned} W_m(r,\theta) =& A_{1m}J_m(\beta r)\sin(m\theta) + A_{2m}J_m(\beta r)\cos(m\theta) \\ &+ A_{3m}Y_m(\beta r)\sin(m\theta) + A_{4m}Y_m(\beta r)\cos(m\theta), \qquad m = 0, 1, 2, ... \end{aligned} \tag{A.9}$$

The boundary condition at $r = a$ is

$$W_m(a,\theta) = 0, \qquad m = 0, 1, 2, ... \tag{A.10}$$

The transverse displacement should be finite at all points on the membrane. Terms with Bessel functions of the second kind, which tend to infinity, must be zero. Therefore, Equation A.9 reduces to

$$W_m(r,\theta) = A_{1m}J_m(\beta r)\sin(m\theta) + A_{2m}J_m(\beta r)\cos(m\theta), \qquad m = 0,1,2,... \quad \text{(A.11)}$$

Using the boundary condition,

$$J_m(\beta a) = 0, \qquad m = 0,1,2,... \quad \text{(A.12)}$$

Equation A.11 generates numerous characteristic equations for each value of m, which satisfies Equation A.12. For all frequencies ω_{mn} there are two modes, except when m=0, for which we obtain only one mode. It follows that for $m \neq 0$ the natural modes are degenerate. The modes can be written as

$$W_{0n}(r,\theta) = A_{0n}J_0(\beta_{0n}r), \qquad n = 1,2,... \quad \text{(A.13)}$$

$$W_{mnc}(r,\theta) = A_{mnc}J_m(\beta_{mn}r)\cos(m\theta), \qquad m,n = 1,2,... \quad \text{(A.14)}$$

$$W_{mns}(r,\theta) = A_{mns}J_m(\beta_{mn}r)\sin(m\theta), \qquad m,n = 1,2,... \quad \text{(A.15)}$$

$$\omega_{mn} = \frac{\alpha_{mn}}{a}\sqrt{\frac{T}{\rho}} \quad \text{(A.16)}$$

$$\beta_{mn} = \frac{\alpha_{mn}}{a} \quad \text{(A.17)}$$

where, α_{mn} is a vibration constant that decides vibration mode. α_{mn} constants for a circular membrane which is clamped at the boundary, are summarized in Table A.1.

Table A.1. Vibration constant of a circular membrane.

	(0,*)	(1,*)	(2,*)	(3,*)
(*,1)	2.4048	3.8317	5.1336	6.3802
(*,2)	5.5201	7.0156	8.4172	9.7610
(*,3)	8.6537	10.1735	11.6198	13.0152
(*,4)	11.7915	13.3237	14.7960	16.2235

Figures A.3 and A.4 show symmetric and asymmetric modes of a circular mem-

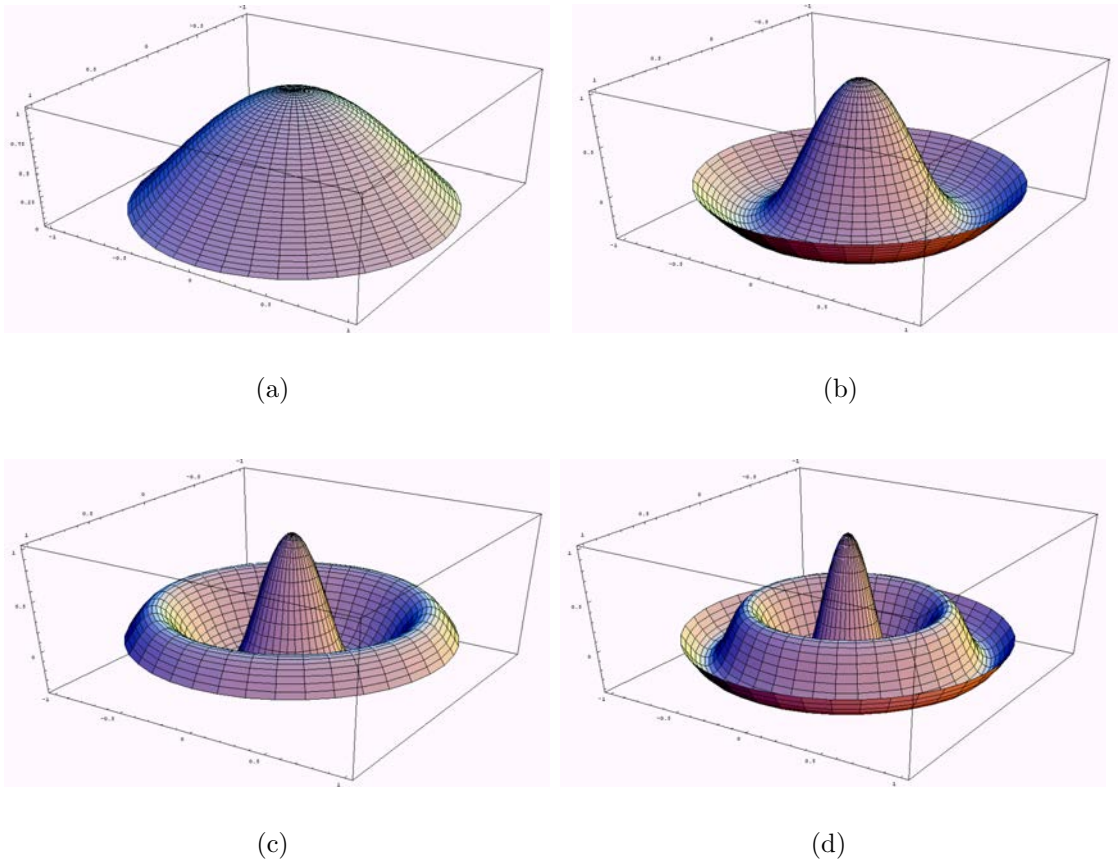

(a) (b)

(c) (d)

Figure A.1. Four lowest symmetric modes of a circular membrane: a) 01–mode, b) 02–mode, c) 03–mode, and 04-mode

brane.

A.0.2 Circular Plates

In the case of a circular plate which is clamped at the boundary, Equation A.18 expresses the transverse vibration in polar coordinates.

$$\nabla^2 W(r,\theta) + \beta^4 W(r,\theta) = 0 \tag{A.18}$$

$$\beta^4 = \frac{\omega^2 m}{D_E} \tag{A.19}$$

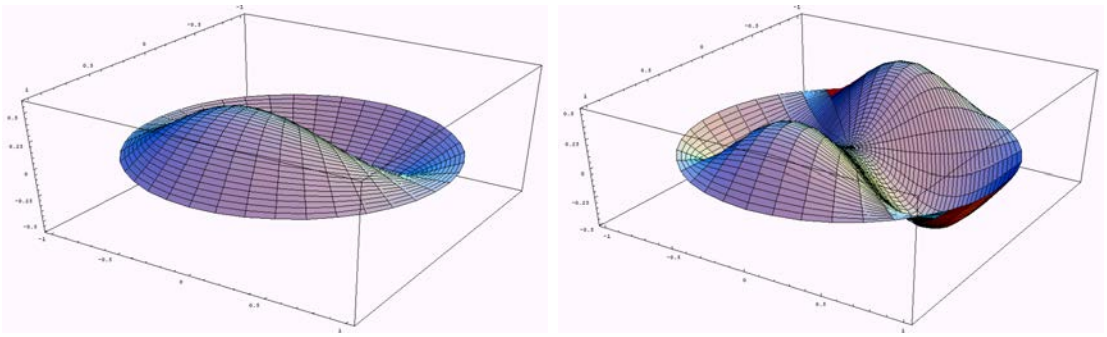

(a) (b)

Figure A.2. Two lowest asymmetric modes of a circular membrane: a) 11–mode, and b) 21–mode.

where W is the transverse displacement, and m and ω are the mass and the angular frequency of the plate, respectively. D_E is the plate flexural rigidity.

The solutions of Equation A.18 are given by Equation A.20.

$$\begin{aligned} W_m(r,\theta) =& [A_{1m}J_m(\beta r) + A_{3m}Y_m(\beta r) + B_{1m}I_m(\beta r) \\ &+ B_{3m}K_m(\beta r)]\sin(m\theta) + [A_{2m}J_m(\beta r) + A_{4m}Y_m(\beta r) \\ &+ B_{2m}I_m(\beta r) + B_{4m}K_m(\beta r)]\cos(m\theta), \qquad m = 0,1,2,... \end{aligned} \tag{A.20}$$

The boundary conditions for a clamped circular plate are

$$W(a,\theta) = 0 \tag{A.21}$$

$$\left.\frac{\partial W(r,\theta)}{\partial r}\right|_{r=a} = 0 \tag{A.22}$$

Using the boundary conditions along with the fact that the solution must be finite at every point on the plate, Equation A.20 reduces to

$$W_{0n}(r,\theta) = A_{0n}[I_0(\beta_{0n}a)J_0(\beta_{0n}r) - J_0(\beta_{0n}a)I_0(\beta_{0n}r)], \qquad n = 1,2,... \tag{A.23}$$

$$\begin{aligned} W_{mnc}(r,\theta) =& A_{mns}[I_m(\beta_{mn}a)J_m(\beta_{mn}r) - J_m(\beta_{mn}a)I_m(\beta_{mn}r)]\sin(m\theta), \\ & m,n = 1,2,... \end{aligned} \tag{A.24}$$

$$W_{mns}(r,\theta) = A_{mnc}[I_m(\beta_{mn}a)J_m(\beta_{mn}r) - J_m(\beta_{mn}a)I_(\beta_{mn}r)]\cos(m\theta), \quad m,n = 1,2,... \tag{A.25}$$

$$I_m(\beta a)J_{m-1}(\beta a) - J_m(\beta a)I_{m-1}(\beta a) = 0 \tag{A.26}$$

$$\omega_{mn} = \frac{\alpha^2}{a^2}\sqrt{\frac{D_E}{m}} \tag{A.27}$$

$$\beta_{mn} = \frac{\alpha_{mn}}{a} \tag{A.28}$$

where, α_{mn} is a vibration constant that decides vibration mode. The α_{mn} values for a circular plate, which is clamped at the boundary, are summarized in Table A.2.

Table A.2. Vibration constant of a circular plate.

	(0,*)	(1,*)	(2,*)	(3,*)
(*,1)	3.1962	4.6109	5.9057	7.1435
(*,2)	6.3064	7.7993	9.1969	10.5367
(*,3)	9.4395	10.9581	12.4022	13.7951
(*,4)	12.5771	14.1086	15.5795	17.0053

Figures A.3 and A.4 show symmetric and asymmetric modes of a circular plate. Compared to vibration modes of a circular membrane, the modes show zero slopes at the boundary.

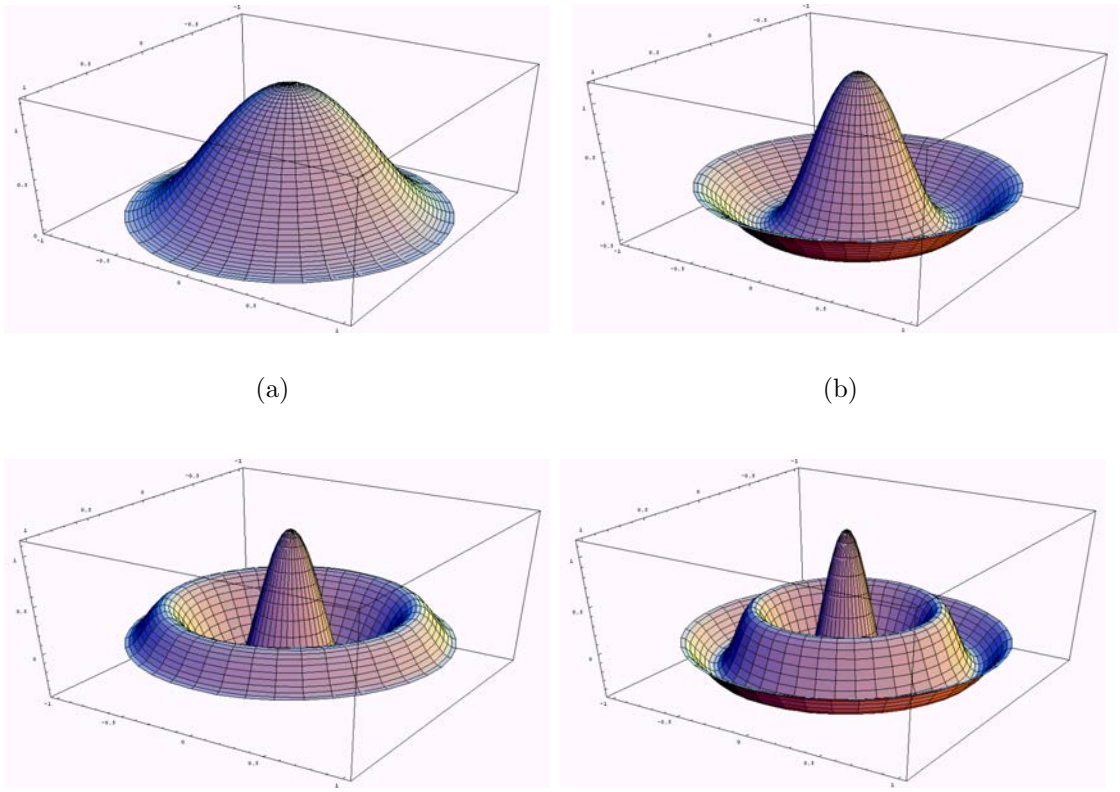

(a) (b)

(c) (d)

Figure A.3. Four lowest symmetric modes of a circular plate: a) 01–mode, b) 02–mode, c) 03–mode, and 04-mode

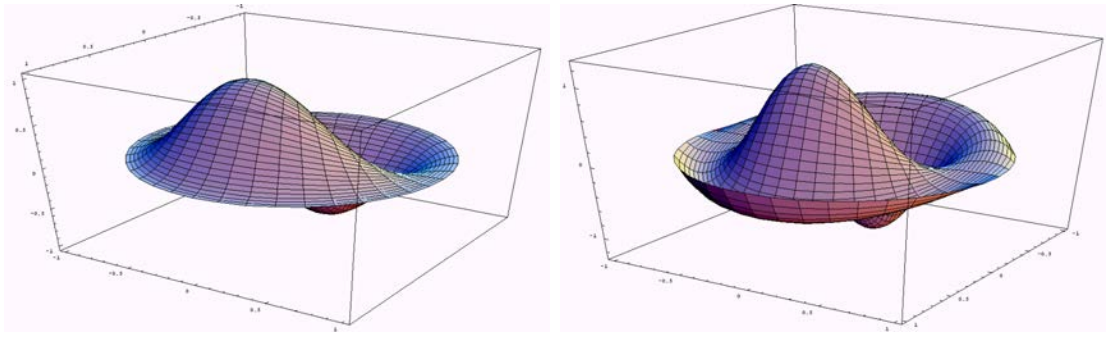

(a) (b)

Figure A.4. Two lowest asymmetric modes of a circular plate: a) 11–mode, and b) 21–mode.

References

[1] L. Meirovitch, *Principles and Techniques of Vibrations*. Prentice Hall, 1997.

Vita

Eunki Hong

Eunki Hong was born in Suwon, South Korea in 1973. He received his BS and MS in Inorganic Materials Science and Engineering from Seoul National University, Seoul, South Korea in 1995 and 1999, respectively. He began his PhD studies at the Pennsylvania State University in the Department of Materials Science and Engineering in Fall 1999. He worked on piezoelectric characterizations of PZT films and studied piezoelectric MEMS devices including micromachined pumps and optical switches.